NANO-SCIENCE CENTER
DEPARTMENT OF CHEMISTRY
FACULTY OF SCIENCE
UNIVERSITY OF COPENHAGEN

PhD thesis

Martin Gudmand, MSc

PHASE BEHAVIOUR AND ENZYME DYNAMICS AT THE LIPID-WATER INTERFACE

- a monolayer, fluorescence microscopy, and spectroscopy study

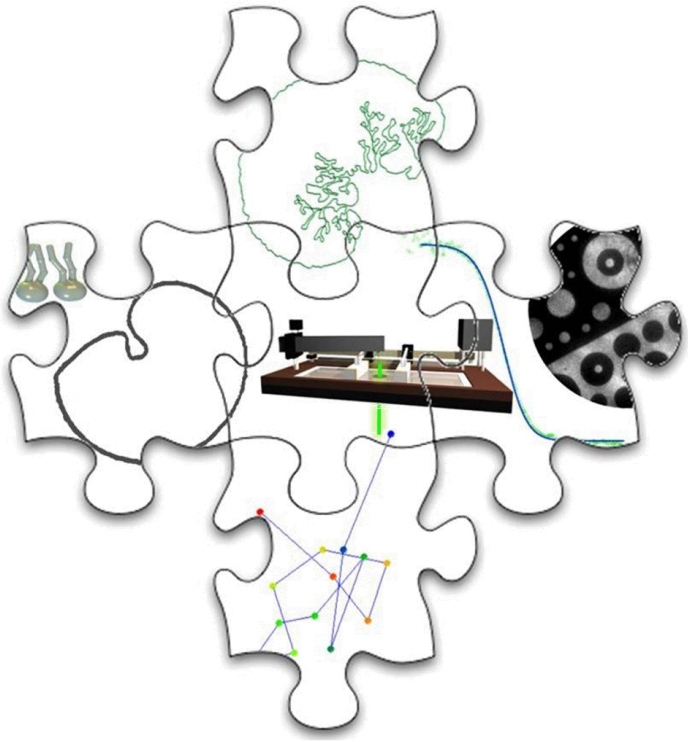

Academic advisors: Prof. Thomas Bjørnholm, PhD
Prof. Thomas Heimburg, PhD

Submitted: May 2008

Acknowledgements

Let me first of all thank everybody who deserves it but did not fit into the tight space below. Let me then go on to mentioning the core of people who have had a direct influence on my work and my life for the past years:

The greatest scientific influence has naturally come from my two supervisors: Prof. Thomas Bjørnholm and Prof. Thomas Heimburg. I am very grateful to Prof. Thomas Bjørnholm for giving me the chance to rejoin the Nano-Science Center and do a PhD. Over the years, it has been an inspiration to witness the enthusiasm for (nano-) science and to participate in vivid discussions. This helped when it was sometimes hard to see the forest for all the trees. The scientific influence of Prof. Thomas Heimburg is apparent in much of the work presented in here, and the word 'thermodynamic' would probably have been used more sparsely if it was not for him. It was reassuring to know that his office door was always open if (or rather when) the experiments became excessively frustrating. I would also like to express my gratitude towards both supervisors for always giving me the freedom to pursue my own ideas, at my own pace. This made the long days in the basement of the Niels Bohr Institute (NBI) seem short.

This project was partially funded by the European Union project "BIOSCOPE" which was a collaboration between several universities and Novozymes A/S (DK). It was very nice to get to know everybody who was part of the project. I always enjoyed the BIOSOCPE meetings, and I am grateful for the rare privilege it has been for a PhD-student to be part of a pan–European project.

The group of "Bioscopists" whom I owe the biggest gratitude is the group of Prof. Johan Hofkens in Belgium (in particular Susana, Hiroshi, and Wendy). Their experience and knowledge with respect to construction of fluorescence microscopes helped me in the beginning. In addition, I benefitted vastly from their help with image post-processing and (in part manually!) tracking of the single molecule experiments presented herein. I am delighted that it was possible to squeeze this analysis into their busy schedule in the very last past of this project.

I would like to thank Prof. Klaus Müllen and his PhD-student Kalina Peneva for providing us with their excellent fluorescent marker (PDI). Nikos Hatzakis, now a member of the Nano-Science Center, is acknowledged for his hard work on labelling and especially purifying the enzyme fluorophore conjugate used for the single molecule tracking experiments. The Novozymes gang; Allan Svendsen, Michael Skjøt, and Thomas H. Callisen steadily delivered knowledge, inspiration, and various purified wild type and mutated enzymes in bulk quantities over the years.

Prof. Benny Lautrup helped with the theory of expanded lipid monolayers. I am thankful for the time, effort, but most of all the enthusiasm that he put into this project.

The people at the NBI workshop have performed an invaluable task in manufacturing the miscellaneous components for the setup. Without the workshop the setup would (still) be held together by cardboard, scotch tape, and instant glue.

I would also like to give my warmest gratitude to those who have been buzzing around the lab the last few years; Heiko (who did a meticulous proof-reading of this manuscript), Andreas, Krissi, Matthias, Kaare, Marie G., Kasia, Marie Jordö, Søren, Inger,.... Thank you for a good time at NBI!

Above all, I thank my family. My daughter for always putting a smile on my face, and my wife for her support and understanding during this project. You still make me want to be a better man.

Abstract & Outline

The present study first describes the construction of a setup that combines a monolayer trough and a fluorescence microscope with a high resolution microscope objective. Next, three different studies are presented which all make use of the setup displaying its strengths which are

- Imaging of monolayer structures at high optical resolution and low fluorophore concentration.
- Single molecule sensitivity which allows imaging of individual fluorophores embedded in a monolayer and single particle tracking experiments.
- Option to perform fluorescence correlation spectroscopy studies of lipid fluorophore diffusion in a monolayer.

This type of setup is ideal for many of the presently exciting single molecule experiments. The monolayer technique provides excellent control over the state of the aggregated lipid structure, and fluorescence microscopy provides excellent optical sensitivity on the single molecule level and high temporal resolution for observing biologically relevant dynamic processes.

The first part of this thesis will set the scene for the different topics by giving an **INTRODUCTION** to the importance of lipid diffusion and enzymatic reactions in the context of biological systems. This part is concluded by the motivation for this work. The second part introduces the basic underlying **THEORY** that is often considered superfluous in papers presented within a narrow field of experts. A main objective of this chapter is to introduce to new people entering this field; the names of a few central authors, their key studies, the terminology, as well as the key concepts. The third part in some ways presents the first result. It describes in detail the **MATERIALS AND METHODS**, especially the novel monolayer trough and fluorescence setup designed and used for many of the experiments herein. The fourth part is divided into three separate chapters, each describing the **RESULTS** from the most important studies performed during this project:

- Direct visualisation and theoretical treatment of the non-equilibrium gas-liquid phase co-existence region in a DPPC monolayer.
- Measurement of the diffusion coefficient of a lipid fluorophore in a DMPC monolayer measured as a function of lateral pressure and mean molecular area.
- Direct visualisation of phospholipase A_2 activity and performing single particle tracking on a DPPC monolayer interface.

In the fifth and final part a summary of all the findings is presented and discussed in the **CONCLUSION**.

List of abbreviations - Chemicals

DiI(C18)	1,1'-dioctadecyl-3,3,3',3'-tetramethylindocarbocyanine perchlorate
Lyso-PC	1-Palmitoyl-2-Hydroxy-sn-Glycero-3-Phosphocholine
DMPC	1,2-dimyristoyl-sn-glycero-3-phosphocholine
DPPC	1,2-dipalmitoyl-sn-glycero-3-phosphocholine
D-DPPC	2,3- dipalmitoyl-sn-glycero-1-phosphocholine
PA	Palmitic acid (product from hydrolysis of DPPC)
PLA_2	Phospholipase A_2
PDI	Derivative of perylene-3,4,9,10-tetracarboxdiimide (Fig. 2.8)
POM	Polyacetal Engineering Polymers, Delrin®
PTFE	Poly(tetrafluoroethene), Teflon®
R6G	Xanthylium, 9-(2-(ethoxycarbonyl)phenyl)-3,6-bis(ethylamino)-2,7-dimethyl, chloride
TRITC-DHPE	n-(6-tetramethylrhodaminethiocarbamoyl)-1,2-dihexadecanoyl-sn-glycero-3-phosphoethanolamine, triethylammonium salt

- Selected terms and experimental techniques

ACF	Auto-correlation function
CM	Confocal microscopy
CLSM	Confocal laser scanning microscopy
FCS	Fluorescence correlation spectroscopy
FRET	Förster resonance energy transfer
FWHM	Full-width at half maximum
MSD	Mean square displacement
NA	Numerical aperture (of a microscope objective)
R	Optical resolution (of a microscope objective)
SMS	Single molecule sensitivity
SMD	Single molecule detection
SM-WFM	Single molecule wide-field fluorescence microscopy
SPT	Single particle tracking
TIRFM	Total internal reflection fluorescence microscopy
WFM	Wide-field microscopy, wide-field fluorescence microscopy
WD	Working distance (of a microscope objective)

Contents

Chapter 1

Introduction

The cell is a fascinating example of nature's complexity, and one of the most basic components of life as we know it. Surrounding every cell is a membrane with a complexity on the same level as the cell itself, and which may vary extensively depending on the function of the cell.

The primary role of the cell membrane (also commonly referred to as the plasma membrane) is compartmentalisation; e.g. protection of the intracellular environment from the harsher conditions of the extracellular surroundings, as well as serving to control local concentrations of biological relevant substances (e.g. ATP). The membrane is composed of three fundamental building blocks; lipids, proteins, and sugars. The relative ratios of these differ between different cell types, and within a single eukaryotic (animal) cell, there exists other membranes which also vary in composition. The membrane proteins have for a long time received the most attention, as many consider these to be responsible for the vital processes relating to the membrane (e.g. transport molecules, and various recognition processes). However, it is now becoming clear that

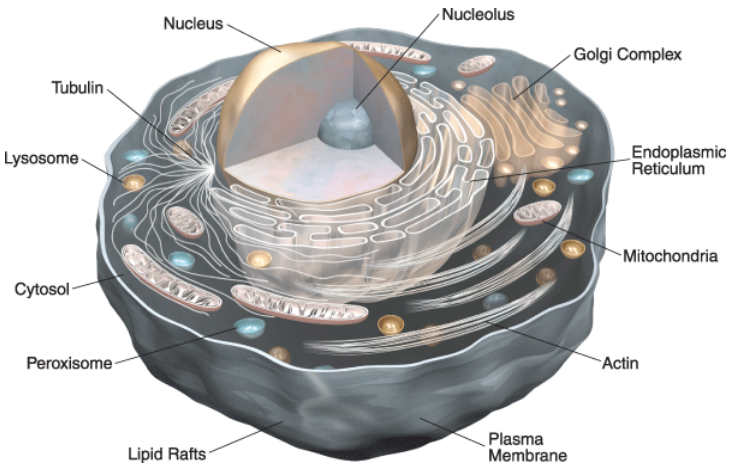

Fig. 1.1 Schematic view of a typical eukaryotic (animal) cell. The cells are large (10-50 μm in diameter) and characterised by having a nucleus (containing DNA) and various organelles; e.g. the mitochondria (ATP generation), the Golgi apparatus (synthesis of proteins and lipids), and the endoplasmic reticulum (protein modification). The primary membrane is the plasma membrane surrounding the entire cell, but the different organelles and compartments also have distinct membranes. Drawing from http://probes.invitrogen.com.

the lipids are more than just a fluid matrix which's only role is as a barrier and/or a solvent for the proteins. This 'lipid renaissance' owes to a large extent to the finding of lipid rafts; special lipid micro-domains which may control various processes; e.g. intracellular trafficking (Edidin 2003).

It is currently not known what exactly determines the lipid composition of biological membranes, and what role it plays, however it is an empirical fact that it is adjusted to neutralise changes in the surrounding media (Macdonald 1988). If for instance, *E. coli* bacteria are grown at different temperatures, than the lipid composition of their membrane will change so that their melting temperature lies just below the growth temperature (Heimburg and Jackson 2005).

This complexity and variation of the lipid composition in cell membranes strongly imply that the lipids play a much larger role in biology than many people currently ascribe to them. Therefore it is important to have a wide range of versatile experimental platforms available for investigating lipid systems. The development and use of such a platform is the main topic of this thesis.

1.1 Membrane models

The documented history of membrane models goes back as far as 1773 (Hewson 1773), with important refinements counting Overton's hypothesis of a 'lipid impregnated boundary layer' (Overton 1899), Gorter and Grendal's finding that the membrane was a bilayer which they concluded by spreading extracted lipids from red blood cells on a Langmuir trough and comparing the areas of the intact cells and the monolayer (Gorter and Grendel 1925). Later, Danielli and Davson added (peripheral) proteins to the model (Danielli and Davson 1935), and finally Singer and Nicholson proposed their renowned "fluid mosaic model", which was inspired by recently available electron microscopy images of cell membranes and x-ray crystallography data of proteins (Singer and Nicolson 1972). The fluid mosaic model was modified by Mouritsen and Bloom in their mattress model which also accounts for lipid reorganisation in the vicinity of integral proteins (Fig. 1.2B); which is referred to as hydrophobic matching (Mouritsen and Bloom 1984).

The fluid mosaic model is still the reference model used throughout the literature, but findings during the last 35 years have led to modifications that are too important to neglect. In the currently accepted membrane models the membrane is much more crowded than in the previous models, different lipid species are inhomogeneously distributed and form domains, some of which are stable over time and some transient. The protein content can also be much higher than indicated in the fluid mosaic model; however the protein content is known to vary a lot. For instance, the myelin membranes surrounding the axons of nerve cells are low in protein content, while photosynthetic membranes are very high in protein content (Engelman 2005). These two examples also show that the function of the membrane correlates to the protein content. The myelin membrane is merely an electrical insulator, while the photosynthetic membranes are highly specialised power plants converting light into energy. The activity of the protein

may in turn be controlled by the lipid environment, and the protein may only function when aggregated as a dimer, or even oligomer. Many of these structure-activity relationships are poorly understood and much work needs to be done on both pure lipid systems and mixed lipid-protein systems to understand the complexity of the cell membrane (Engelman 2005).

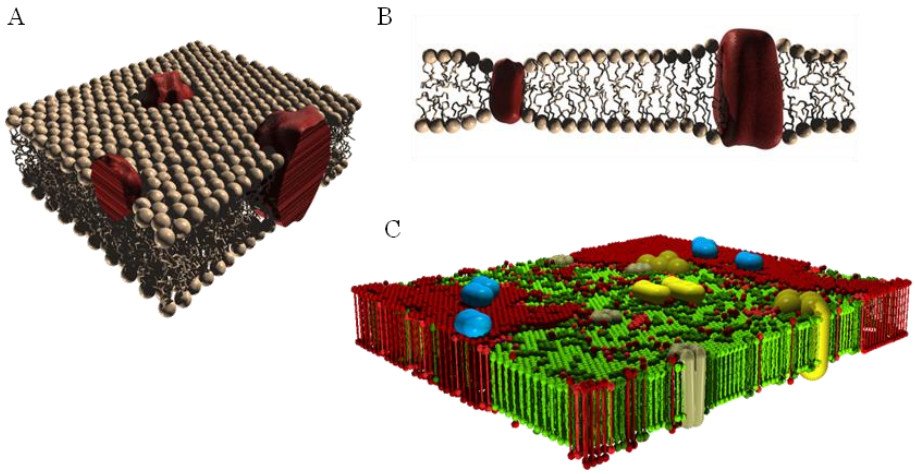

Fig. 1.2 Three simplified representations of the biological membrane model **A:** The membrane according to the fluid mosaic model from 1972 **B:** The mattress model from 1984 which also accounts for hydrophobic matching between the lipid matrix and embedded proteins **C:** The current view emphasising the clustering and inhomogeneous distribution of proteins and lipids. (Images A and B are courtesy of A. Blicher. Image C is courtesy of H. M. Seeger).

1.2 The biological role of PLA_2

The cell membrane is not a fixed entity. Its state can be altered by even small changes in e.g. temperature, pH, ion concentration, or by enzymatic activity changing the composition of the membrane and/or the local pH. Such changes in state can have a dramatic effect on the structure and function of the membrane. For instance, domain formation may be hindered, membrane permeability may increase, or the internal pressure in the membrane may change causing transmembrane proteins to alter structure and activity.

An enzyme that has received vast attention the last 50 years is phospholipase A_2 (PLA_2). The enzyme catalyses the hydrolysis of phospholipids at the sn-2 ester bond to produce 1-acyl-lysophospholipids and free fatty acids (see also Fig. 6.1). Its activity is closely coupled to the biological membrane in that PLA_2 is only active when presented to aggregated lipid structures such as the membrane. In addition, the activity is increased many fold in the presence of domain boundaries between phase separated regions and in systems near the melting transition (sometimes referred to as the main transition). In this region the state of the lipid molecules fluctuate between ordered and disordered

states. As cell membranes are mainly in the fluid state, one might speculate that a biological role of PLA_2 is to act as a scavenger for cells that, due to e.g. decease, show changes in lipid composition and pronounced domain formation. The action of PLA_2 could thus be to either change the composition of the membrane, bringing it back into a fluid state, or to disrupt the cell structure entirely (lysis).

It is known that PLA_2 takes part in a variety of physiological processes ranging from membrane remodelling, cell signalling, digestion, cell lyses (hence the name of the product molecule 'lyso-lipid'), inflammation, and cancer. (Kudo and Murakami 2002; Mouritsen, Andersen et al. 2006; Simonsen 2008).

1.3 Diffusion in the cell membrane

Lipids and proteins in a cell membrane constantly move due to thermal agitation. This movement is referred to as diffusion and is important for cell function and stability. Diffusion of lipids and proteins in the cell membrane is a stochastic process; the movement is random, and given enough time the particles will explore all the accessible areas of the membrane. Throughout this thesis we shall only deal with translational diffusion, i.e. diffusion along the plane of the membrane, and will later illustrate how diffusion can be described mathematically and measured experimentally (Section 2.1).

Diffusion in cell membranes is complex and depends on many different aspects. In general, membranes are in the fluid state which should allow for rapid diffusion. However, it has long been known that measured rates of diffusion (i.e. the diffusion coefficients) of lipids and proteins in biological membranes are 10-100 times slower than in fluid state model membranes; most often pure phospholipid bilayers. The reason for this is that the membrane is inhomogeneous; it is crowded with integral and peripheral proteins, it is segmented as the different lipids tend to phase separate, and the entire domain structure is interconnected by a cytoskeleton network. This places serious restrictions on the lateral diffusion of the lipids and proteins, and a subset of diffusion models are therefore needed to describe the diffusion. The most relevant are hindered diffusion (Fig. 1.3A), confined diffusion (Fig. 1.3B), directed motion (Fig. 1.3C), and free diffusion/Brownian motion (Fig. 1.3D). For the first two cases, hindered and confined diffusion respectively, the effects imposed on the diffusion behaviour are transient. For instance, in the middle section of trajectory A in Fig. 1.3, the particle diffuses freely. This means that the measured diffusion coefficient depends on the time scale on which it is measured. This is very important and we will return to this in Section 2.1.

Many physiological processes are cascade reactions that rely on several molecules being in close proximity. This means that the reaction kinetics can be controlled by the ability of the lipids and proteins to diffuse to a given reaction site on the membrane. Since this ability is governed by the lateral membrane structure, and the membrane structure may be altered as part of the reaction in question, the membrane structure alone could provide an effective feedback control mechanism. For instance, a given

reaction could be stopped when it has altered the membrane structure to a degree where it is no longer favourable for the reactants to be in the vicinity of each other.

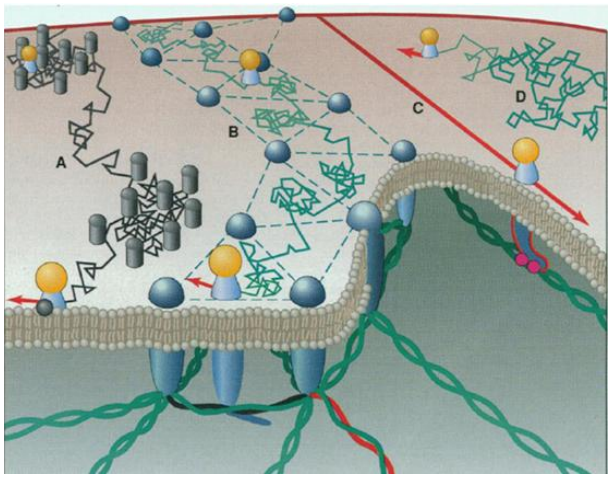

Fig. 1.3 Four different modes of diffusion. **A:** (Transiently) hindered diffusion **B:** confined diffusion **C:** directed motion **D:** free diffusion/Brownian motion. Drawing from (Jacobson, Sheets et al. 1995).

1.4 Monolayers

The phospholipid molecules which to a large extent make up the cell membrane are water-insoluble and belong to a class of molecules called amphiphiles. Amphiphilic molecules are defined as molecules where one part of the molecule is hydrophilic (the head), and the other part is hydrophobic (the tail). When exposed to a water surface, or more strictly an air-water interface, the lipids spontaneously self-organise with the heads immersed in the aqueous phase and tails pointing away into the air region. This process creates a molecular layer that is one molecule thick and which floats on the water surface. Such films are commonly referred to as (insoluble) monolayers or Langmuir films. We will use both terms throughout this thesis.

Monolayers are excellent two-dimensional model system. The water surface is perfectly flat, and several thermodynamic variables are easily controlled (Section 2.2). In a biophysical context, the monolayer is especially interesting in its role as 'half a membrane', because biological membranes can be considered as two opposing (weakly coupled) monolayers. For instance, the lipid composition in cellular membranes generally differs on the inside (*cytoplasmic*) and on the outside (*extracellular*); i.e. the membrane leaflets are asymmetric. Each of these different lipid compositions can easily be mimicked in practice using the monolayer technique. In general, the monolayer technique is highly suited for investigating dynamic lipid-protein interactions (e.g. adsorption). In addition, since it is rather uncomplicated to visualise the microscopic structure of a monolayer by fluorescence wide-field microscopy, one of the strong points

of the monolayer technique is structure-activity studies. As we shall see in Chapter 6, a protein (here phospholipase A_2) injected under a monolayer may cause a significant pressure increase when it penetrates or otherwise perturbs the lipid monolayer. If the monolayer lipid is a substrate for the protein, then a change of state and morphology can also be observed as a result of the protein-lipid interaction.

1.5 Motivation

Despite the many attractive features offered by the monolayer technique, it has so far not been possible to carry out single molecule experiments on this experimental platform. The reason for this has been the need for long working distance microscope objectives with poor quantum collection efficiency. A popular workaround has been to transfer the monolayers to solid supports (most often mica) and then investigate the structure of the sample using atomic force microscopy (AFM) or wide-field fluorescence microscopy (WFM). AFM has unsurpassed structural resolving power, but the temporal resolution (~5 min/image frame) and the lack of capability to locate and track the position of diffusing particles are some of the drawbacks of this method. However, the major drawback of transferring the monolayer is that many of the control handless which are precisely the strongpoint of the monolayer technique are lost when the monolayer is removed from the air-water interface.

This led to one of the primary ambitions formulated at the beginning of this project: To construct a setup where it was possible to perform single molecule studies directly on the water-lipid interface. More specifically, we would like to visualise the behaviour of individual phospholipase A_2 (enzyme) molecules on a monolayer. PLA_2 is especially interesting because, it is a long established fact that it is activated at domain boundaries and packing defects (Op den Kamp, de Gier et al. 1974; Grainger, Reichert et al. 1989; Grandbois, Clausen-Schaumann et al. 1998; Nielsen, Risbo et al. 1999), and that it accumulates at lipid domain boundaries over time (Dahmen-Levison, Brezesinski et al. 1998). However, the dynamics of the individual enzyme molecules has not been studied until now.

As implied above, the main obstruction for doing single molecule fluorescence studies on monolayer structures at the water-lipid interface is the need for microscope objectives with high quantum collection efficiency. Such objectives are primarily characterised by having a high numerical aperture (NA > 1). We will return to the definition of NA in Section 2.3.2, for here it will suffice to state that the higher the NA, the more photons are collected from an emitter (e.g. a fluorescing molecule). These high NA microscope objectives typically have working distances of 200 μm or less. This distance has to accommodate both the glass window in the bottom of monolayer trough as well as the height of the aqueous subphase. This means that the height of the monolayer subphase, when using high NA microscope objectives, is restricted to 50-100 μm. Having a subphase of this height is difficult, but as we shall see not impossible, and the resulting image quality is remarkable.

The implementation of a microscope objective with high NA also makes it possible to do fluorescence correlation spectroscopy (FCS). This is a very powerful experimental technique. It is in some regards complementary to single particle tracking (SPT), since it also determines diffusion coefficients on the single molecule level. However, in FCS one usually determines diffusion coefficient of several thousands of diffusing particles within a small area during a few seconds, and the analysis of these measurements is done at the click of a (mouse-) button. In contrast, the analysis of a similar number of single particles trajectories in a SPT experiment typically require a few days of (manual) labour. However, SPT has the advantage that it, in addition to the diffusion coefficient, also reveals e.g. the partitioning of the lipid fluorophore in different regions of the lipid structure.

The setup which was constructed for this purpose is shown in Fig. 1.4 and described in detail in Chapter 3. The setup was based on an existing fluorescence correlation spectroscopy setup, which was completely rebuilt to allow for the addition of an additional higher power laser line and the integration of the monolayer trough.

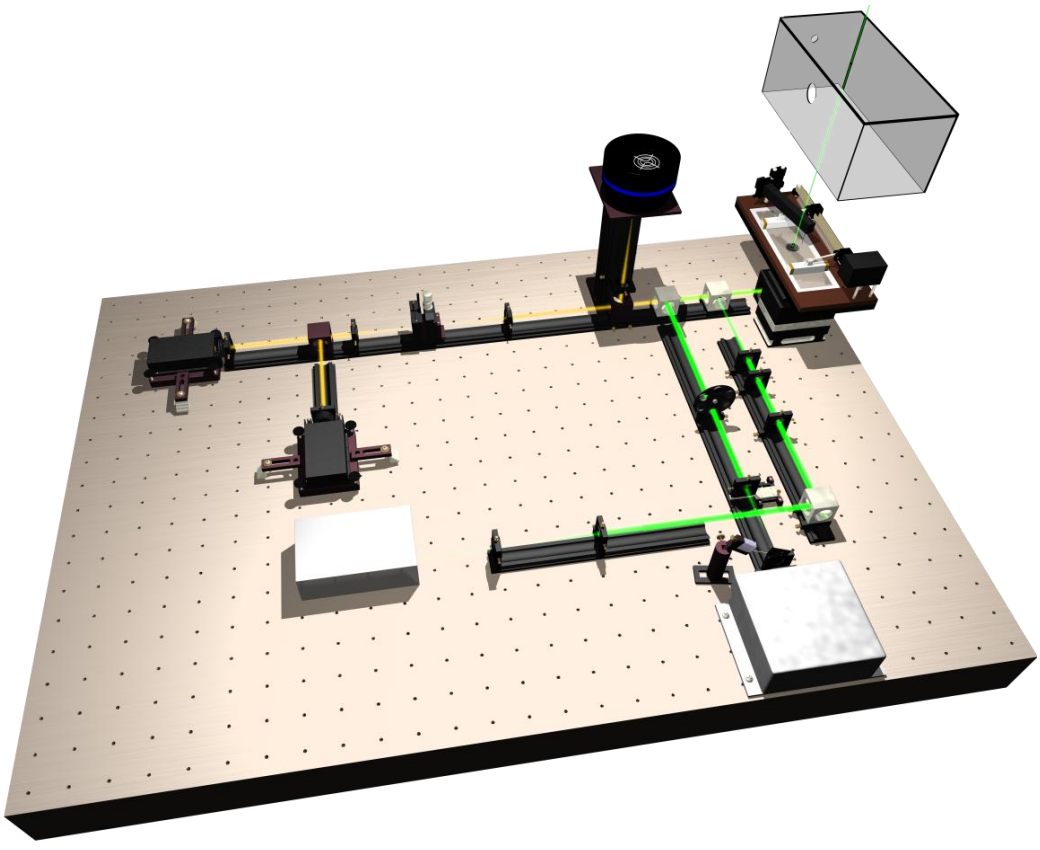

Fig. 1.4 Overview of the combined monolayer, fluorescence microscopy and spectroscopy setup. Drawing is made to scale, and the table dimensions are 1 metre by 1.30 metre. A detailed description is given in Chapter 3.

Chapter 2

Theory

2.1 Diffusion models

In this section the basic mathematical models used to describe translational diffusion in two-dimensional systems will be introduced. Emphasis will be put on the origin and intrinsic assumptions of each model. Later, in Chapter 5, these models will be used to fit the experimental data from lipid diffusion in monolayers at the air-water interface.

Some of the most basic concepts of diffusion properties were formulated by Fick in 1855. Based on simple assumptions he derived two differential equations known as Fick's first and second law (Fick 1855). Fick's first law describes the steady-state flux J_x of particles induced by the local particle concentration gradient $\partial C/\partial x$

$$J_x = -D\frac{\partial C}{\partial x} \tag{2.1}$$

where D is the diffusion coefficient, C is the particle concentration, and x is the one-dimensional space coordinate. Fick's second law states how the particle concentration changes over time

$$\frac{\partial C}{\partial t} = D\frac{\partial^2 C}{\partial x^2} \tag{2.2}$$

In his classic paper from 1905, Einstein re-derived Fick's second law based on a statistical treatment of Brownian diffusion. Further he formulated a numerical solution describing the mean square displacement $\langle x^2 \rangle$ of a particle in one dimension (Einstein 1905)

$$\left\langle x^2 \right\rangle = 2Dt \tag{2.3}$$

This solution is valid when the observation time t is long compared to the time of individual particle movements. In two dimensions where $r^2 = x^2 + y^2$ the mean square displacement (MSD) from the origin to the point $\langle x,y \rangle$ becomes

$$\left\langle r^2 \right\rangle = 4Dt \tag{2.4}$$

In the same paper, Einstein used Fick's first equation, and Stokes' law, to derive the well-known diffusion equation for microscopic spheres in liquid solution

$$D = \frac{k_B T}{f} = \frac{k_B T}{6\pi\eta R_H} \tag{2.5}$$

where k_B is the Boltzmann constant, T is the absolute temperature in Kelvin, f is the friction coefficient, η is the viscosity of the solution, and R_H is the hydrodynamic radius of the particle.

2.1.1 *Diffusion in inhomogeneous media*

Fick's and Einstein's diffusion equations (vide supra) assume a homogenous environment surrounding the diffusing particle. This is not always the case, and rarely the case in real biological systems where diffusion of lipid and protein molecules in the plasma membrane may be hindered by (transient) obstacles and/or confined within (transient) sub-compartments (Jacobson, Sheets et al. 1995; Kusumi, Koyama-Honda et al. 2004). Numerous of the possible inhomogeneities that a particle can experience in two-dimensional systems have been described in detail; see e.g. (Saxton 1987; Saxton 1994; Almeida and Vaz 1995; Hac, Seeger et al. 2005; Saxton 2007). For the present study, it is of special interest that particles experiencing hindered diffusion due to obstacles (e.g. domains) are said to display "anomalous diffusion". In two dimensions this is defined as

$$\left\langle r^2 \right\rangle = 4Dt^{\alpha} \tag{2.6}$$

where $0 < \alpha$ and $\alpha \neq 1$. For $\alpha = 1$ diffusion is normal and Eq. (2.6) reduces to Eq. (2.4). In biology one only encounters $\alpha < 1$ (so-called sub-diffusion), and never $\alpha > 1$ (super-diffusion). If diffusion takes place in a system under directed flow due to e.g. experimental artefacts such surface flow due to convection or biological driven processes such as directed transport, then the diffusion can be described by

$$\left\langle r^2 \right\rangle = 4Dt^{\alpha} + (vt)^2 \tag{2.7}$$

where v is the velocity of the directed flow. This type of diffusion is easily identified in fluorescence correlation spectroscopy (FCS) as the auto-correlation function clearly deviates from that obtained under normal diffusion behaviour (Widengren and Mets 2003; Heimburg 2007). The FCS technique is described in Section 2.3.4.

For anomalous diffusion it turns out that the measured diffusion coefficient depends on the size of the obstacles relative to the size of the observation volume, as well as the observation time (Fig. 2.1). For instance, if the obstacles are smaller than the observation volume, then for short observation times the diffusion generally appears normal as the particles do not interact with the obstacles, at medium observation times the diffusion is anomalous as the particle traces are obstructed by the obstacles. At long times the effect of obstruction is averaged out, and apparent normal diffusion is again observed, but the observed diffusion coefficient is lower than at shorter times (Saxton 2007). It may also be instructive in relation to this discussion to re-examine Fig. 1.3.

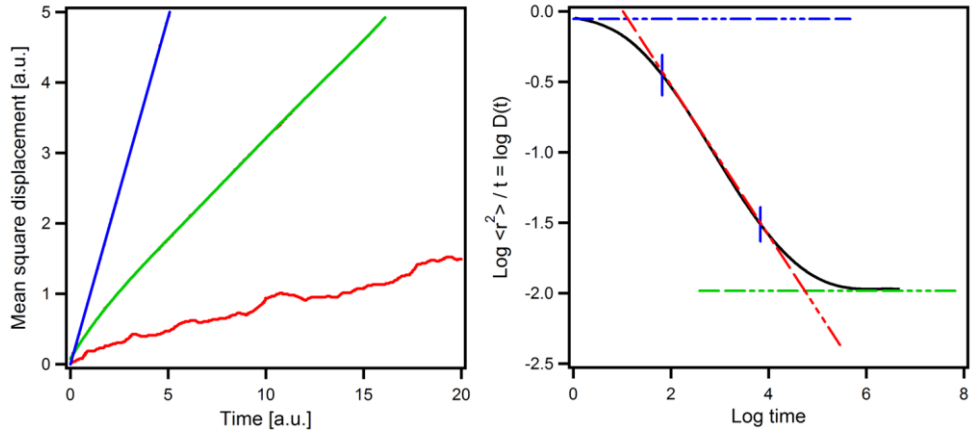

Fig. 2.1 The dependence of the MSD on the observation time **Left**: The blue line shows the linear relationship between MSD and time for normal diffusion. The green curve shows a non-linear relationship at short times and linear at longer times; typical for diffusion in a media where small evenly distributed obstacles are present. Red data shows anomalous diffusion recorded on an intermediate temporal and lateral resolution. **Right**: Anomalous diffusion can be analysed in a log-log plot. The diffusion coefficient D is normalised so it is 1 at short times (blue line), red line yields the anomalous diffusion exponent α, and the green line the apparently normal diffusion constant (where the effect of the obstacles on the diffusion averages out) at long observation time, $D(\infty)$. Both plots adapted from (Saxton 2007).

This general phenomenon has led some authors to distinguish between microscopic and macroscopic diffusion coefficients. The microscopic diffusion coefficient being the diffusion coefficient of free (unhindered) diffusion, and the macroscopic diffusion coefficient being the diffusion coefficient obtained when hindered diffusion is measured on time scales where the MSD appear to be linear with respect to time. In Fig. 2.1, the microscopic diffusion coefficient is given by the top (green) line and the macroscopic diffusion constant the (blue) bottom line.

It will become evident later that this has important consequences when evaluating diffusion coefficients from different types of experiments such as e.g.; NMR, Single Particle Tracking (SPT), Fluorescence Correlation Spectroscopy (FCS), and Fluorescence Recovery After Photo-bleaching (FRAP).

2.1.2 The Saffman-Delbrück model

Unfortunately, there is no simple equivalent of the Stokes-Einstein relation, Eq. (2.5), for two-dimensional lipid systems. This is partly due to the fact that it is not possible to derive an expression for a constant friction coefficient f for an infinite two dimensional fluid (Almeida and Vaz 1995). This is known as Stokes' Paradox. Many attempts have been made to get around this problem; most successfully by Saffman and Delbrück (Saffman and Delbruck 1975). They proposed a model that includes the viscosity of the fluid(s) surrounding the lipid sheet and thereby treats the system as three-dimensional.

Their model assumes that the diffusing particle acts as a hard cylinder positioned perpendicular to the surface of the membrane. This yields an expression for the diffusion coefficient

$$D = \frac{k_B T}{4\pi\eta h}\left[\ln\left(\frac{\eta h}{\eta' R}\right) - \gamma\right] \tag{2.8}$$

where h is the height of the bilayer, η is the viscosity of the lipid layer, η' is the viscosity of the surrounding solution ($\eta << \eta'$), R is the radius of the molecule, and γ is Euler's constant (≈0.5772).

Numerous modifications of the model have been proposed to account for e.g. different viscosities above and below the lipid sheet ($\eta'_1 \neq \eta'_2$) as for instance in monolayer studies (Hughes, Pailthorpe et al. 1981; Hughes, Pailthorpe et al. 1982)

$$D = \frac{k_B T}{4\pi\eta h}\left[\ln\frac{2}{\varepsilon} - \gamma + \frac{4}{\varepsilon} - \frac{\varepsilon^2}{2}\ln\frac{2}{\varepsilon}\right] \tag{2.9}$$

where ε is the dimensionless parameter

$$\varepsilon = \frac{R}{h}\left(\frac{\eta'_1 + \eta'_2}{\eta}\right) \leq 1 \tag{2.10}$$

The Saffman-Delbrück model is a direct extension of the Stokes-Einstein relation, and as such a continuum hydrodynamic model. It is strictly only valid when the diffusing particle is much larger than the solvent molecules. The lower limit for which the model is expected to hold is small proteins (R ~ 1-2 nm) and it can therefore not be used to describe lipid diffusion (Vaz, Clegg et al. 1985; Liu, Paprica et al. 1997; Saxton 1999). The model has some inherent weak points; the calculated diffusion coefficient depends highly on the viscosity of the lipid sheet, but the viscosity of the fluid sheet is not easily determined, and diffusing particles may also sense different viscosities dependant on their shape, height, and tilt relative to the bilayer (Seelig and Seelig 1980; Gambin, Lopez-Esparza et al. 2006).

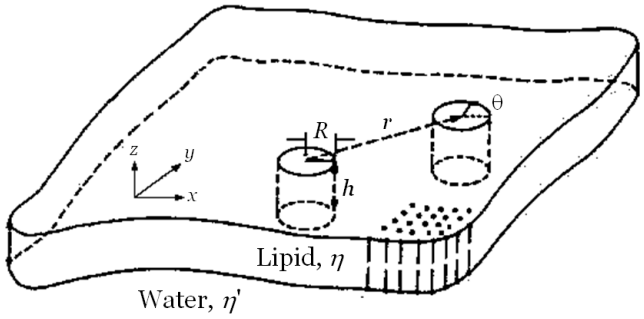

Fig. 2.2 The hydrodynamic model. The particle is modelled as a cylinder with radius R and height h, which is also the height of the membrane. The membrane is surrounded by an aqueous phases on both sides. The particle is only permitted to move laterally in the x-y plane, and to rotate around the z-axis. Figure adapted from (Saffman and Delbruck 1975).

2.1.3 The Free-area model

It has been known for at least 100 years that viscosity only varies a little between different van der Waal liquids, and that it varies little with temperature at constant volume, but that it varies markedly with pressure. This was systematically shown by Batchinsky, who noted that viscosity could be described as a function of "*relative volume of molecules present per unit of free space*" (Batchinski 1913), which Doolittle later successfully formalised (Doolittle 1951). He found that the viscosity of liquids can be satisfactorily described by a simple free-space model as Batchinsky also had predicted. Doolitle proposed an empirical relation between free volume (i.e. the excess volume that arises from thermal expansion of the liquid) and viscosity for pure liquids, far from the phase transition region:

$$\eta = Ae^{B/(v_f/v_0)} \tag{2.11}$$

$$\ln\eta = \ln A + B(v_0/v_f) \tag{2.12}$$

where v_f is the free volume in one gram of solution at a given pressure and temperature, v_0 is the volume of 1 gram of the solution at zero Kelvin (extrapolated without phase change), and A and B are substance specific constants. As an example for the valid range of Eq. (2.11) Doolitle described the correlation between predicted model values and actual measured values for n-heptadecane ($C_{17}H_{36}$) which has a boiling point of 303 °C and freezing point of 22 °C: "*All values measured between 100 °C and 300 °C inclusive lay on a straight line, whereas values below 100 °C gradually deviated (...) reaching a maximum difference of 16.6% at the freezing point*".

Cohen and Turnbull employed this relation to propose a diffusion model for particles with sizes smaller than or equal to the solvent particles (Cohen and Turnbull 1959). By relating the Stokes-Einstein relation and Doolittle's empirical finding, they derived a free-volume model for diffusion in three dimensions in which the diffusion coefficient is proportional to the free volume instead of viscosity. This model is strictly only valid in the regime where the diffusion coefficient is inversely proportional to the viscosity – which is often neglected to mention. This is a consequence of the two relations upon which the model is based: Cohen and Turnbull stress that they assume this when setting up the free-volume model (Cohen and Turnbull 1959), and the fact that the Stokes-Einstein relation directly contains this proportionality.

The free-volume model can be adapted to the two-dimensional case of lipid diffusion in a lipid matrix simply by converting the volume terms to area terms (Galla, Hartmann et al. 1979). The derivation and assumptions of the model follow the lines of Cohen and Turnbull: The lipids are modelled as hard rods confined to a cage made up by their nearest neighbours. When density fluctuations generate an opening (i.e. a free area), and the opening exceeds a critical area a_c, then displacement of the lipid molecule becomes possible. Effective displacement of the lipid then occurs if the void created by the lipid displacement is filled by the movement of other lipid molecules, before the initial lipid molecule moves back to its original position. This is schematised in Fig. 2.3.

In order to express this quantitatively a free area a_f is defined as

$$a_f = a_{av} - a_o \tag{2.13}$$

where a_{av} is the mean area per lipid, and a_o is the van der Waals radius of the (~hard rod) lipid. Under conditions where the lipid molecules experience negligible particle interactions (as in a gas), one can calculate the instantaneous diffusion coefficient using gas kinetic theory

$$D(a_f) = g l_c \mu = g l_c \sqrt{\frac{2k_B T}{m}} \tag{2.14}$$

where g is a geometric factor (≈1/4), l_c is the average length free travel of the particle in the free area, μ is the gas kinetic constant, and m is the mass of the particle. Since the critical area a_c is the minimal possible area for which diffusion is possible, one can state that for a free area smaller than the critical area ($a_f < a_c$) the diffusion coefficient equals zero

$$D(a_f) = 0 \tag{2.15}$$

One may also state that for a free area larger than the critical area ($a_f > a_c$) the instantaneous diffusion coefficient $D(a_f)$ does not vary with the size of the free area and thus

$$D(a_f) = D(a_c) \tag{2.16}$$

Given that the instantaneous diffusion coefficient $D(a_f)$ is constant, the average diffusion coefficient D for a lipid molecule can be expressed as a function of the probability of finding a free area large enough to permit displacement

$$D = \int_{a_c}^{\infty} D(a_c) \cdot p(a_f) \cdot da \tag{2.17}$$

where $p(a_f)$ is the probability of finding a free area a_f. Integration from a_c to ∞ yields the final relation between the average diffusion coefficients of a lipid molecule as a function

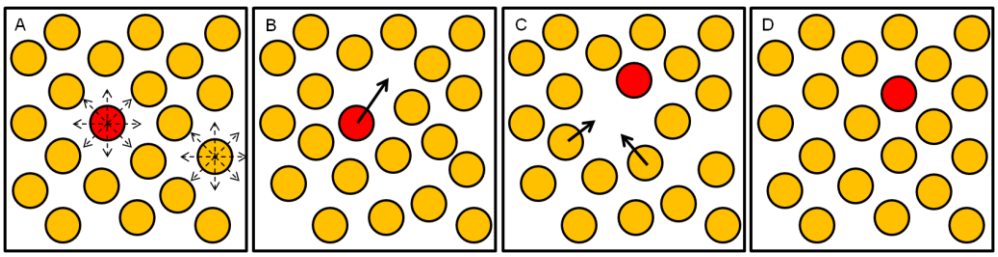

Fig. 2.3 Top view of a lipid matrix during translational diffusion according to the free area model. **A:** The initial situation. The molecules are in constant movement with an instantaneous diffusion coefficient estimated from the gas kinetic velocity (cf Eq. (2.14)). Lipids cannot change position due to the dense packing **B:** Voids in the lipid matrix are created as a result of density fluctuations that arise from thermal agitation. A neighbouring lipid molecule (highlighted in red) may move into the void whenever the void exceeds a critical size a_c **C:** The void created by the displacement of the first molecule is taken up by other molecules **D:** The lipid matrix with the red molecule in a new position and thus effectively displaced.

of the free area

$$D = D(a_c) \cdot e^{(-\gamma a_c / a_f)} \tag{2.18}$$

where γ is a geometric factor correcting for overlap of free areas ($0.5 < \gamma < 1$).

This equation is frequently used when fitting experimental data. It can readily be seen that it only has a weak dependence on temperature ($T^{½}$, cf. Eq. (2.14)) but no activation energy to account for interactions with other particles. A more general equation, the Macedo-Litovitz hybrid, contains this activation energy and has been proposed by multiple authors. It accounts for a possible energy barrier between the two equilibrium situations before and after displacement (Macedo and Litovitz 1965; Chung 1966; Ricci, Ricci et al. 1977; Vaz, Clegg et al. 1985). In two dimensions this equation can be written as

$$D = A_0 D(a_c) e^{-\gamma a_c / a_f - E_a / k_B T} \tag{2.19}$$

where A_o is a constant only dependent on temperature, and E_a is the activation energy per molecule.

The free-area model is theoretically simple and qualitatively intuitive, but quantitatively it is often criticised for the number of fitting parameters, which at present seem to vary with both the method used and system investigated; e.g. (Falck, Patra et al. 2005). Nevertheless the model often correctly predicts the trends within a system quite accurately (Galla, Hartmann et al. 1979; Peters and Beck 1983; Almeida, Vaz et al. 1992; Ke and Naumann 2001). The free-area model will later be used to evaluate the experimental data on lipid diffusion in monolayers.

2.2 Insoluble monolayers

The effects of oil on water have been investigated for millenniums. Pliny the Elder (23 AD - 79 AD), Plutarch (46 AD - 120 AD), and Franklin (1706 - 1790) among many others have reportedly studied the different aspects of the phenomenon (Gaines 1966). Irving Langmuir is considered the creator of the presently used techniques (Langmuir 1917), and monolayers formed at the air-water interface are commonly referred to simply as Langmuir films.

Monolayers constitute a very versatile experimental platform. The Langmuir technique provides control of various intensive thermodynamic variables (lateral pressure, temperature, pH, ionic strength, etc.), and extensive variables (area, amount of particles, etc). Monolayers are often used as membrane models. In this function monolayers are especially suited for investigating the interaction of proteins and lipid interfaces, while they are generally unsuited for investigation of transmembrane processes and transmembrane proteins (e.g. passive or protein mediated transport of ions).

Essentially, an experimental setup consists of a trough filled with water, two movable barriers, and a balance (Fig. 2.4). An amount of particles (hereafter lipid) is deposited

in-between the barriers and the barriers are moved towards each other. The compression leads to a decrease in the mean molecular area (MMA) whereby the surface pressure increases. The result is most often presented in a pressure-area isotherm (Fig. 2.5).

The natural observable in the Langmuir technique is the lateral pressure Π defined as the difference in surface tension of a pure surface γ_0 and a lipid covered surface γ

$$\Pi = \gamma_0 - \gamma \tag{2.20}$$

Surface tension is caused by molecules at the surface having higher energy than molecules in the bulk. Water has an exceptionally high surface tension. Some authors attribute this to an entropy decrease at the surface due to ordering and increased hydrogen bonding; e.g. (Israelachvili 1991), while others suggest that, due to fewer neighbouring water molecules, hydrogen bonds are lost at the interface leading to lower enthalpy; e.g. (Chalikian 2001). In thermodynamic terms surface tension is defined as the energy (e.g. Helmholtz free energy, F) required to create a surface area A;

$$\gamma = \left(\frac{dF}{dA} \right)_{T,V,n} \tag{2.21}$$

where T is the temperature, V is volume, and n the amount of molecules in the monolayer (Gaines 1966). Since γ_0 is constant, the lateral pressure can also be expressed as

$$\left(\frac{dF}{dA} \right)_{T,V,n} = -\Pi \tag{2.22}$$

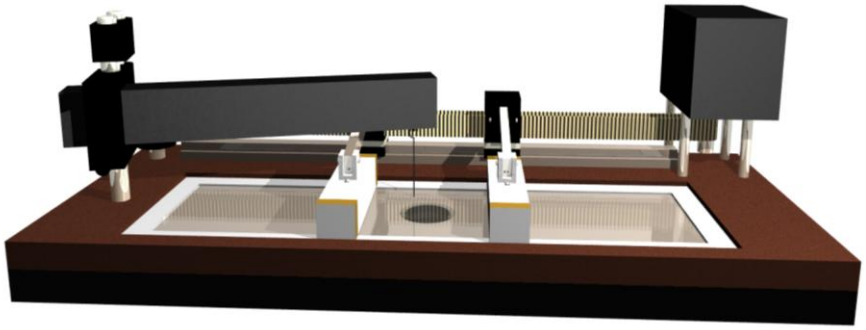

Fig. 2.4 A standard Langmuir setup: Trough, two barriers, and a balance. The setup shown here is the commercial version from Kibron Inc. (www.kibron.com). Most troughs are machined from PTFE (Teflon), but the trough shown here is made of a highly hydrophilic metal alloy which allows for lower subphases than Teflon troughs usually do. The rim of the trough is made from PTFE, and the barriers are from POM (aka Delrin) with PTFE tape on the sides. A metal rod, hanging from a piezo-electric crystal, acts as the balance measuring the surface pressure. Figure made in POV-Ray.

Equation (2.22) presents an, at least, interesting theoretical challenge because it is only valid for a constant amount of particles, *n*. Thus, if there is exchange of lipid or other particles between the surface and the subphase then the monolayer is not a closed thermodynamic system (Möhwald 1995). Therefore, a strict thermodynamic treatment requires that the monolayer is completely insoluble; i.e. no lipid can be dissolved in the aqueous subphase, which is of course an approximation under experimental conditions. In addition caution should be exercised when treating monolayer phases as being stable thermodynamic equilibriums as this is rarely the case. In general, ordered monolayer phases are only meta-stable (Möhwald 1995).

2.2.1 Phospholipid monolayers

The major lipid constituents of biological membranes are double chain phospholipids. A significant part of these are long chain phosphocholines, e.g. DPPC, which are virtually insoluble in water. This makes them excellent model molecules for monolayer studies (cf. Eq (2.22) and related discussion). DPPC in particular has received much interest, most likely due to the convenience of having a system with a phase co-existence region at room temperature, but also because DPPC is the major constituent of lung surfactant, a monolayer that reduces the surface tension in our lungs and keeps them from collapsing when exhaling (Goerke 1998).

Throughout this thesis, we will use the following nomenclature to describe the monolayer phases in the sections beneath (listed in order of increasing lateral pressure): G gas phase, LE liquid-expanded (often referred to as *fluid*), LC liquid-condensed (often referred to as *gel*), and S for the solid phase (often referred to as *crystalline*). The two mixed phases will be referred to as LE-LC phase co-existence region (often referred to as the *main* transition), and G-LE phase co-existence region.

It has been a subject of discussion for a long time whether the LE-to-LC phase transition in phospholipid monolayers is a first order transition or not. At the heart of this discussion is the question of how to define a first order phase transition. In the classical definition by Ehrenfest, a first-order phase-transition has a discontinuous entropy versus temperature curve at the transition temperature. This means that at exactly one well-defined temperature the entropy changes abruptly; e.g. as in the melting of a crystal. From this it follows that the enthalpy of transformation

$$\Delta H_{tr} = T_{tr}\Delta S \tag{2.23}$$

must be non-zero; since $\Delta G(T_{\mathrm{tr}}) = 0$. The transition in a phospholipid monolayer does not fit the classification very well. It is clearly seen that there are no discontinuities in the isotherms or the isobars in Fig. 2.5 (Albrecht, Gruler et al. 1978). For this reason Lee instead proposed to simply define a first order transition as one having an enthalpy of transformation (Lee 1977).

Gibbs phase rule has also been frequently applied in this discussion. The rule applies to an ideal system with macroscopically separated phases (Lee 1977; Heimburg 2007), which exhibit first-order phase transitions. It defines the number of intensive variables

that can be set arbitrarily (i.e. degrees of freedom, F) within a given phase. For an ideal two-dimensional system at fixed temperature Gibbs phase rule states (Petty 1996)

$$F = (C^b + C^s) - (P^b + P^s) + 1 \tag{2.24}$$

where C^b and C^s are the number of component in the bulk and surface, and P^b and P^s is the number of phases in bulk and surface at equilibrium. In a simple experiment where a single lipid component, on a pure water surface, is brought into the phase transition; C^b = 2 (air and water), C^s =1 (the lipid), P^b = 2 (air and water) and P^s =2 (the two different lipid phases), there are no degrees of freedom available (F = 0). Therefore, according to Gibb's phase rule, the lateral pressure is not allowed to change when compressing the monolayer through the phase transition. The pressure-area isotherm should therefore exhibit a completely horizontal plateau in this region (cf. Fig. 2.5 and Fig. 2.6). This feature has never been experimentally realised. However, Gibb's phase rule is not directly applicable to this problem. It is derived from strict thermodynamic considerations, and as such prerequisites infinite purity of chemical species, perfect crystalline packing, and macroscopic phase separation. The purity of the system obviously makes a difference in relation to Eq. (2.24); if e.g. the lipid is contaminated then C^s increases, allowing for more degrees of freedom. Along the same lines, imperfect crystalline packing in an otherwise pure system can be thought of as contamination with air. the significance of macroscopic phase separation is more complicated: First of all, Gibb's phase rule assumes that there are only two lipid species present in the phase transition: Lipids in the ordered state (e.g. gel) and lipids in the disordered (fluid) state each with their distinct chemical potential. However, since there is a phase boundary, at least one more (high energy) lipid species must exist; lipids at the phase boundary. If the system is large (i.e. infinite) and the phases are macroscopically phase separated then the interface may simply be ignored. Consider for instance a monolayer trough with a

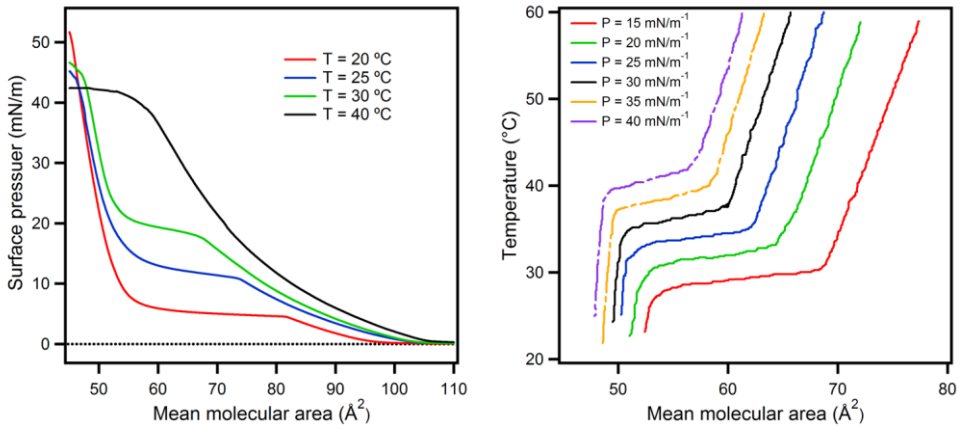

Fig. 2.5 Left: Pressure-area isotherms of DPPC. At T < 40 °C three distinct regions are observed: At high MMA the liquid-expanded phase (LE), at low MMA the liquid condensed phase (LC), and at intermediate MMA the nearly horizontal LE-LC phase. What appear as a horizontal region of the isotherm at 40°C, is due to monolayer collapse near the phase transition at the critical temperature (Own data). **Right:** Isobars for DPPC. Isobar data adapted from (Albrecht, Gruler et al. 1978).

single phase boundary in the centre. On the left there is only lipid in the gel state and on the right only lipid in the fluid state Letting the length of the trough become infinite does not change the absolute size of the phase boundary, but relatively it becomes negligible. This is the case for which Gibb's phase rule applies. In an actual monolayer experiment, macroscopic phase separation does not readily occur. Instead, the gel state lipids form domains embedded in the fluid state lipid matrix, creating one heterogeneous phase (Heimburg 2007). As a result the phase boundary size will scale with system size. A larger trough will simply contain more domains. Therefore the contribution from the lipids at the phase boundary cannot be ignored in monolayers and Gibb's phase rule cannot be applied (Lee 1977; Heimburg 2007).

Albeit the term is at best ambiguous, the consensus within the monolayer-community is to classify the LE-to-LC phase transition as first order, with the non-horizontal slope being primarily explained by the presence of impurities and imperfect crystalline packing (Lee 1977; Albrecht, Gruler et al. 1978; Georgallas and Pink 1982; Lösche and Möhwald 1984; Pallas and Pethica 1985; Möhwald 1995; Nielsen, Bjornholm et al. 2007). This designation is in accord with Lee's classification, since one definitely can state that the monolayer phase transition has an enthalpy of transformation (at $T < T_C$). Whether the transition would be continuous at zero contamination and perfect crystalline packing remains speculative.

A practical consequence of this discussion is that care should be taken when referring to different scenarios such as; macroscopic phase separation, co-existence of e.g. LC-domains in a LE matrix, and domain formation (e.g. lipid rafts) in lipid systems.

A practical consequence of the finite slope and the continuous transition is that it becomes difficult to determine the exact onset and conclusion of the phase transition region (cf. Fig. 2.5: Left panel). It has been proposed to determine the transition points

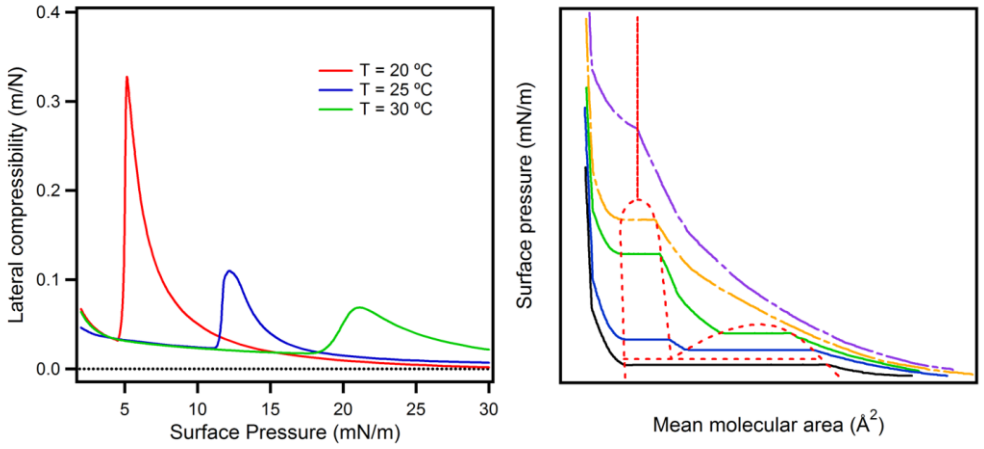

Fig. 2.6 Left: Compressibilities κ_T calculated from isotherms in Fig. 2.5 (Own data). **Right**: Generic pressure-area phase diagram for phospholipid monolayers. The areas within the arcs denote the gas - liquid-expanded phase co-existence region (G-LE region) and the liquid-expanded - liquid-condensed phase co-existence region (LE-LC region). Diagram is modified from (Albrecht, Gruler et al. 1978).

using the lateral compressibility

$$\kappa_T = -\frac{1}{A}\left(\frac{dA}{d\Pi}\right)_T \tag{2.25}$$

Either from a plot of κ_T versus area (Nielsen, Bjornholm et al. 2007) or from the derivatives of κ_T with respect to area (Brockman, Jones et al. 1980). However, most values given in the literature are found from simple visual inspection of the isotherm and therefore vary quite a lot; this is especially true for the pressure (and molecular area) values given for the conclusion of the LE-to-LC phase transition.

It can also be shown that the lateral compressibility is proportional to the area fluctuations in the monolayer at constant pressure (Heimburg 2007)

$$\kappa_T = \frac{\langle A^2 \rangle - \langle A \rangle^2}{\langle A \rangle RT} \tag{2.26}$$

where R is the gas constant. This means that when κ_T is at maximum then the area fluctuations in the monolayer is also at a maximum. We will later see that this plays an important role for the enzyme kinetics of phospholipase A_2 (PLA_2).

2.2.2 Phospholipid monolayer-bilayer relationship

A fundamental question arises whenever phospholipid monolayers are used as models for bilayers or biological membranes: How do phospholipid monolayers and phospholipid bilayers compare?

The obvious difference between monolayers and bilayers is the surface tension of the interface. Whereas the surface tension of the monolayer-water interface is controlled by an applied mechanical force from the barriers, the net surface tension in a bilayer is zero; balanced by the opposing forces from the contracting hydrophobic effect and expanding effect from steric repulsion between the tightly packed lipid molecules (Israelachvili 1991).

Marsh published the perhaps most thorough paper on the subject (Marsh 1996; Marsh 2006) where he compared monolayer and bilayer properties from both theoretical (e.g. free energy considerations, isothermal compressibility, molecular dynamics simulations) and experimental data from mostly DPPC (e.g. phase transitions, enzyme kinetics, partitioning). Marsh reached the conclusion that the monolayer-bilayer equivalence lateral pressure lies between 30-35 mN/m at 20 °C.

A similar value is found when the area change of DPPC lipids at the melting transition is considered. In monolayers, the lipid area change can be seen directly from the isobars in Fig. 2.5 (right). The isobars show that the DPPC melting transition is shifted towards increasing temperatures and has decreasing widths when the surface pressure is increased. At a pressure of 30 mN/m, the melting transition begins at a lipid area of 50.5 Å^2 and ends at 60 Å^2. These areas should be compared with the lipid areas for fluid and gel state lipids in the melting transition of a bilayer. These areas are usually

not reported in the literature. Generally, the lipid areas are given at temperatures relatively far from the melting transition. For instance, the lipid areas for DPPC are given as 48 Å² in the fluid phase (measured at 20 °C) and 64 Å² in the gel phase (measured at 50 °C) (Nagle 1993; Nagle and Tristram-Nagle 2000) for which the main melting transition lies at 41 °C. These values can be corrected for temperature using the relation

$$\frac{dA}{dT} = \alpha_A \cdot A_0 \tag{2.27}$$

where α_A is the thermal expansion coefficient ≈ $4 \cdot 10^{-3}$ k^{-1} (Heimburg 1998). The temperature corrected values DPPC at 41 °C are: a_{gel} = 51 Å² and a_{fluid} = 61 Å². These areas correspond well to the areas found from the isobar at Π =30 mN/m Fig. 2.5 (right).

Other authors suggest that the equivalence pressure is 50 mN/m (Nagle 1976; Gruen and Wolfe 1982; Jahnig 1984; Feng 1999). However this pressure is above the critical point, thereby involving that the monolayer phase transition does not involve area or enthalpy change, which does not appear to be valid (Albrecht, Gruler et al. 1978)

It should be apparent from the discussion above that it is not trivial to directly compare a monolayer to a bilayer. The application of a monolayer as half-a-bilayer should be done in consideration with the system and phenomena under investigation. It should also be kept in mind that the above discussion mainly relates to systems containing only one lipid species. It is obvious that the level of complexity can rapidly increase with the number of components; e.g. for systems with asymmetric bilayers where lipid interdigitation, coupling between domains across bilayer leaflets, etc. can have profound effects.

2.3 Fluorescence, microscopy and spectroscopy

Fluorescence microscopy is an excellent way to investigate monolayer morphology and dynamics. In the following the basic principles of fluorescence which need to be understood to properly set up a fluorescence experiment are described. The emphasis is put on topics that are directly relevant to the experimental work in this thesis.

2.3.1 Fluorescence

Fluorescence can be defined as the emission of light from an electronically excited substance, while a fluorophore is a molecule that can emit light when it is electronically exited[1] (Lakowicz 2004).

[1] Throughout the text only organic molecule fluorophores will be considered. Quantum dots (inorganic nano-crystals) have not been used in this study and will not be considered.

For convenience, the discussion will in general deal with energy instead of wavelength. Energy E and wavelength λ are related by

$$E = \frac{h \cdot c}{\lambda} \tag{2.28}$$

where h is Planck's constant ($6.6 \cdot 10^{-34}$ J·s), and c is the speed of light in vacuum ($3.0 \cdot 10^{8}$ m/s).

The energy levels and transition pathways associated with excitation and relaxation processes are often schematized in a Jablonski diagram (Fig. 2.7): A photon is absorbed; raising the energy level of the molecule from the singlet ground state (S_0) to a singlet excited energy level (S_1, S_2, etc). This happens on a timescale of $\tau \sim 10^{-15}$ s. By internal conversion, the molecule loses energy due to e.g. internal vibrations and relaxes to the lowest vibrational level of S_1 ($\tau \sim 10^{-12}$ s). From this energy level the molecule can return to the ground state via several different pathways; e.g. by emission of a photon ($\tau \sim 10^{-8}$ - 10^{-9} s), or by spin conversion to a triplet state T_1 followed by another spin conversion back to the ground state S_0. Because spin conversion is quantum mechanically forbidden these processes are relatively improbable. However since there is often overlap between a vibrational energy levels of S_1 and T_1 this transition can be quite fast ($\tau \sim 10^{-9}$ s), whereas the T_1 to S_1 is usually very slow (between $\tau \sim 10^{-6}$ s and 1 s).

The Jablonski diagram illustrates the fundamental processes and show why the energy of the emitted photons is generally lower than the energy of the absorbed photons; i.e. most fluorescence occurs at higher wavelength than absorption. The energy difference between the most probable absorption energy and most probable emission

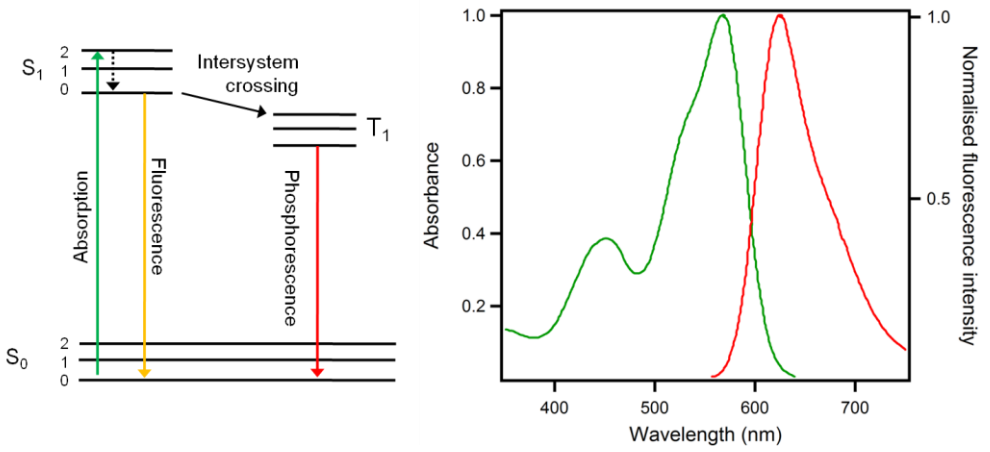

Fig. 2.7 Left: Jablonski diagram representing the transition between different molecular energy levels. S_0 and S_1 denote the singlet ground state and first electronic state energy levels. 0, 1, 2, etc are vibrational energy levels available within each state. Conversion from one state to another can occur via: Absorption/excitation (green arrow), intersystem crossing (black) fluorescence (orange), or phosphorescence (red). Internal conversion is the transition between vibrational energy levels within the same state (dashed). **Right**: Normalised absorption and emission spectra for the PDI fluorophore used later. From (Margineanu, Hofkens et al. 2004).

energy is known as the Stokes' shift, and is found from the peaks in the absorption and emission spectra for a given fluorophore (Fig. 2.7, right panel). There is also a minor part of the emitted photons which have a higher energy than the absorbed photons. This happens when a fluorophore is excited from a higher vibronic state of S_0 to a low vibronic state of S_1. Then the relaxation back to the lowest vibronic state of S_0 will be accompanied by a larger energy difference than the absorption process. This anti-Stokes fluorescence accounts for the observed overlap between absorption and emission spectra.

It is also apparent from the Jablonski diagram that the energy of the emitted light is independent of the excitation energy. This is known as Kasha's rule (Lakowicz 2004). This follows from the fact that the emitted light has the energies associated with transition from the lowest vibronic state of S_1 to different vibronic states of S_0 regardless of the excitation energy.

In addition to the pathways already mentioned, the relaxation from S_1 to S_0 can also be non-radiative through e.g.; dissipation (i.e. loss of energy as heat), energy transfer to another molecule, or catalytic deactivation (quenching). Since both radiative and non-radiative decay pathways are possible, it is useful to define a measure for their ratio. The fluorescence quantum yield Φ_f defines the relative amount of absorbed and emitted photons as the rate constant of fluorescence k_f relative to the sum of rate constants for all decay processes k_{nr};

$$\Phi_f = \frac{k_f}{k_f + \sum k_{nr}} \tag{2.29}$$

This is one of the most important characteristics of a fluorophore. High quantum yields generally signify bright emission and relatively low probability of bleaching (discussed further below); since most bleaching processes occur from the triplet state (Lichtman and Conchello 2005).

Another important characteristic is the probability that the fluorophore will absorb a photon. This is given by the molar extinction coefficient ε measured in $M^{-1}cm^{-1}$ or the absorption cross section measured in cm^2.

Labels for fluorescence microscopy are often synthesised organic molecules with a large degree of π-electron conjugation (e.g. alternating double bonds and aromatic ring structures). Conjugation of π-electrons over a large part of the molecule leads to delocalisation of electrons, and reduces the energy difference between the lowest unoccupied molecular orbitals (LUMO) and the ground state orbitals (HOMO) (Suppan 1994; Lakowicz 2004). This facilitates excitation as the energy required for the $S_1 \rightarrow S_0$ transition becomes similar to the energies of visible light. In general, conjugation also increases the fluorescence quantum yield (Lichtman and Conchello 2005).

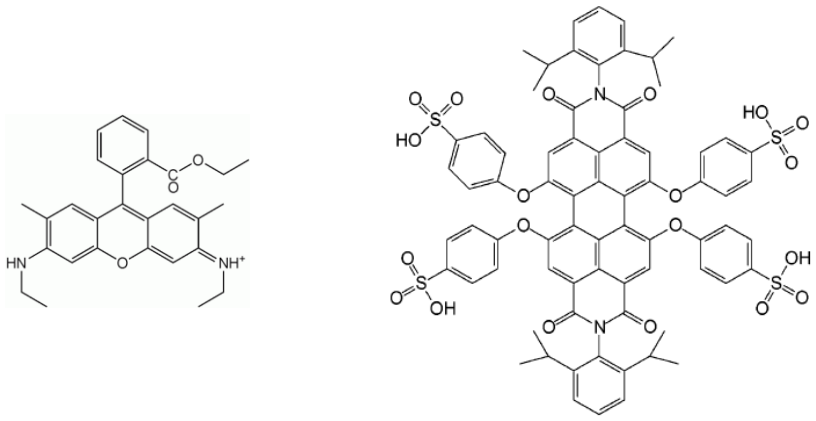

Fig. 2.8 Two of the dyes used in this study. Both labels have a high degree of π-conjugation **Left**: Rhodamine 6G which is often used as a reference in fluorescence studies **Right**: The perylene derivative "PDI" is a recently synthesised fluorophore with excellent photo-physical characteristics: High molar absorption, high quantum yield, long life time, and water solubility (Margineanu, Hofkens et al. 2004)

Returning again to the Jablonski diagram (Fig. 2.7, left), it could appear as if the absorption-fluorescence cycle could run infinitely. This is unfortunately not the case as organic fluorophores tend to bleach under ambient experimental conditions. Bleaching, or photo-induced degradation, is a broad term used for a variety of processes that permanently destroy the fluorophores ability to fluoresce (unlike quenching[2]). Bleaching is a severe limiting factor in single molecule experiments since the experiment basically ends once the molecule under investigation is bleached. Attempts to minimise bleaching are therefore crucial, and much research is currently going into mapping bleaching pathways. Current consensus is that bleaching is closely connected to a chemical reaction between the exited fluorophore's long lived triplet state and ground state triplet oxygen. (Yu, Hu et al. 2000; Christ, Kulzer et al. 2001; Zondervan, Kulzer et al. 2004; Hoogenboom, van Dijk et al. 2005). Oxygen is also known as a quencher of phosphorescence, but via a different mechanism. Presence of paramagnetic oxygen increases the probability of inter system crossing, most pronounced from T_1 to S_1, effectively lowering the triplet population (Widengren, Mets et al. 1995).

It has also been found that the rate of bleaching is strongly dependent on the excitation power, and that one can get orders of magnitude more photons from a given fluorophore before it bleaches by keeping the excitation power low (Deschenes and Bout 2002; Margineanu, Hofkens et al. 2004). The experimentalist can thus obtain a significant increase in fluorophore lifetime by keeping the excitation intensity at a minimum and only illuminating the smallest required area or volume.

[2] Strictly speaking; quenching refers to a photo-physical process; e.g. altering the probabilities of decay pathways, while bleaching is a photo-chemical process altering the molecular structure of the fluorophore (most often oxidation). The concepts are not used consistently in the literature.

In addition to bleaching, there is a more subtle photo-physical phenomenon known as blinking. Blinking, or fluorescence intermittency, is an observable fact where the molecule temporarily loses its ability to fluoresce. Blinking is a reversible process, as opposed to bleaching, and can occur on two timescales: Short-lived blinking ($\tau \approx$ triplet life time) is attributed to the fluorophore being in the triplet state, and is often referred to as triplet blinking (Hoogenboom, van Dijk et al. 2005). Long-lived blinking ($\tau \gg$ triplet life time) has so far only been observed in immobilised fluorophores; e.g. in gels or at glass surfaces (Zondervan, Kulzer et al. 2003; Yeow, Melnikov et al. 2006). It is often attributed to temporary trapping of charges in the immobilisation media (e.g. the gel, crystal, or glass) following photo-induced charge separation and subsequent charge recombination. However the exact mechanism remains unclear and alternative models are still being discussed (Tang and Marcus 2005; Hoogenboom, Hernando et al. 2007). So far, no studies relating to long-lived blinking of freely diffusing organic fluorophores in solution has been published. Probably do to the experimental difficulties this presents. However, most of the existing models require a rigid matrix to stabilise the long lived blinking state (Zondervan, Kulzer et al. 2003). In an experiment where the fluorophores and separated charges are free to diffuse, such charge separation would most likely lead to bleaching via chemical reaction with other molecules in the solution.

2.3.2 Applied fluorescence microscopy

Various fluorescence techniques are currently receiving immense attention in biophysics. This owes partly to the fact that it is a versatile (largely) non-invasive method that can be applied in vitro as well as in vivo, and partly to the fact that one can quite easily detect single molecules at high temporal and spatial resolution.

In fluorescence microscopy, as in conventional light microscopy, the most important component is the objective. It is characterised by a numerical aperture (NA), magnification (M), and working distance (WD). The NA is defined by

$$\mathrm{NA} = n_i \sin\theta_{\max} \tag{2.30}$$

where n_i is the refractive index of the immersion medium (which can be air, water or oil), and $\theta_{\max}$ is the half-angle of the maximum cone of light picked up by the objective (Hecht 2002). For a water immersion objective with NA 1.2 the half-angle is 64°. As Eq. (2.30) shows, an objective with larger NA picks up light from a wider cone. But not only more light is collected from the sample when using high NA objectives, also higher order diffraction patterns are collected resulting in a higher resolution (R); i.e. the smallest distance that two particles can be separated by and still be resolved as two individual particles (Abbe 1873; Rayleigh 1879). This is known as the Rayleigh criterion for resolution. This lead to the following expression for the resolution R

$$\mathrm{R} = \frac{1.22 \cdot \lambda}{2 \cdot \mathrm{NA}} \tag{2.31}$$

where λ is the wavelength of light, and $1.22 \cdot \lambda$ is the approximate diameter of an Airy disc (See Fig. 2.9, right). The resolution is, however, not the precision by which a particle

position can be determined. This can in theory be infinitely precise, as long as the inter-particle distance exceeds the distance defined by the Rayleigh criterion. In fluorescence microscopy a spatial precession of 10-100 nm is frequently obtained by fitting the imaged fluorescence intensity to a two-dimensional Gaussian distribution function; this is sometimes referred to as pixel-fitting (Ghosh and Webb 1994; Schutz, Schindler et al. 1997; Ober, Ram et al. 2004).

The magnification (M) of an objective is defined as the relative enlargement of the image over the object (Piston 1998). In video microscopy, where the image is recorded on a finite size pixel array rather than observed by the naked eye, the magnification should not be chosen arbitrarily. Instead it should be chosen in agreement with the size of the camera's CCD chip and the objective's NA since these two are the factors that limit the resolution. According to the sampling theorem (aka the Nyquist criterion), optimal digital sampling is obtained when collecting two points per resolution size (Spring 1997); i.e. the magnification should be chosen so that the smallest resolvable objects cover two pixels (*px*) on the CCD chip. Magnification below this level is referred to as under-sampling and lead to information loss, while over-sampling "only" lead to practical problems such as; loss of contrast, loss of field of view and excess storage size of image files (Piston 1998).

The last microscope objective characteristic is the working distance (WD); i.e. the distance between the outer lens of the objective and the focus plane. The WD is indirectly related to the NA, and in general a higher NA means a shorter WD. This is most easily realised by looking at the left panel in Fig. 2.9: For a given lens diameter, the

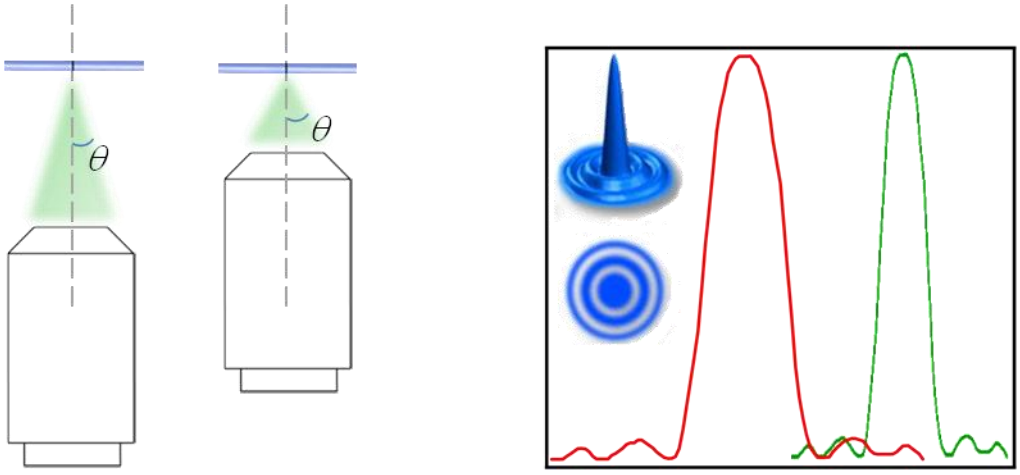

Fig. 2.9 Left: Scematic drawing of two microscope objectives with similar physical dimensions. The one to the left has a longer working distance and therefore also has a smaller half-angle (θ) of the cone of light picked up by the objective. **Right:** full lines illustrate the intensity cross section of the two airy discs created by diffraction form a point source. The airy pattern to the right (green) has a smaller half-width and belongs to the objective with the smaller working distance (higher NA). The relationship between half-angle, numerical aperture, and radius of the airy disc is given by Eq. (2.31). **Inset:** 3D representation of the airy disc. The central maximum (zeroth order maximum) contains ~84% of the intensity. (Inset figure adapted from:

distance between the sample and objective becomes shorter when the angle of collected light becomes larger. A high NA objective typically has a WD on the order of 100-200 μm.

Fluorescence microscopy presents a few additional challenges to ordinary light microscopy due to the photo-physics of organic fluorophores; e.g. saturation, bleaching, triplet formation, and energy transfer. In specialised techniques energy transfer and bleaching can be used advantageous. For instance, in Förster Resonance Energy Transfer (FRET) and Fluorescence Recovery After Photo-bleaching (FRAP) respectively. In most cases however, and especially in single molecule detection (SMD) and single particle tracking (SPT), bleaching effects present a major challenge. Since the probability of bleaching increases with the excitation intensity, it is important to keep the excitation intensity at a minimum, and the fluorescence collection efficiency as high as possible. This can be accomplished using high NA objectives, custom made filter sets with high transmission (>95%), and use the proper digital sampling as described above.

2.3.3 Fluorescence Microscopy Techniques

There are many different ways in which a microscopy sample can be illuminated and excited by a light source. The three most common are; Wide-field, confocal and total internal reflection. Wide-field fluorescence microscopy (WFM) and total internal reflection fluorescence microscopy (TIRFM) have both been used for image formation in this study. The confocal configuration has not been used for image formation (microscopy), but for fluorescence correlation spectroscopy (FCS) described in Section 2.3.4.

WFM set up in so-called Köhler illumination is the simplest way to achieve nearly homogenous illumination: A collimated laser beam is focussed in the centre of the back focal plane on the microscope objective resulting in a collimated, but much narrower, beam perpendicular to the sample surface. In this configuration, not only the focal plane is illuminated, but also a large part of the surroundings, which may cause a significant background signal (i.e. noise). In some applications this is not a problem. For instance when all fluorophores are localised in the focal plane as in single particle tracking studies on membranes (Schmidt, Schutz et al. 1996) or monolayers (Ke and Naumann 2001). However, as soon as fluorescent particles are added to the aqueous phase the S/N ratio can become a serious problem if the ambition is single molecule sensitivity (SMS).

To obtain a better S/N, one can set up the microscope under TIRF conditions. By aligning the laser off-centre to the objective, the laser beam is made to be incident on the sample at an angle (Funatsu, Harada et al. 1995; Dickson, Norris et al. 1996; Moerner and Orrit 1999). The more off-centre the laser is aligned, the larger the angle will be. The largest angle achievable by a given objective is defined by its numerical aperture (NA). When the angle between the incident laser and the sample reaches a critical value, then total internal reflection occurs. This results in the laser being reflected at the interface, which creates an evanescent wave propagating along the interface. The critical angle is given by

$$\theta_{critical} = \sin^{-1}\frac{n_2}{n_1} \tag{2.32}$$

Where $n_1 > n_2$ are the refractive indexes of first (incidence) and second (reflection) media respectively. For a laser beam incidence through water (n_1 = 1.33) at an air-water interface (air: n_2 = 1.0) the critical angle is 48.8°. This means that TIRF is achievable with a water immersion objective with NA=1.2 (since $\theta_{\max}$ ~64°) at an air-water interface when the laser is incident through water. The distance from the interface to where the intensity has decreased by $1/e$ defines the penetration depth d of the evanescent wave. It can be calculated from the relation (Paige, Bjerneld et al. 2001)

$$d = \frac{\lambda}{2\pi\sqrt{n_2^2 \sin^2\theta_i - n_1^2}} \tag{2.33}$$

Typical values (λ = 532 nm, angle of incident light θ_i = 64°) yields $d \approx$ 100 nm.

The last fluorescence microscopy technique available is confocal microscopy, where only a diffraction limited volume is illuminated at any given time. By scanning either the sample over the laser (CM) or the laser over the sample (Confocal Laser Scanning Microscopy: CLSM) an image can be acquired. This technique has not been used for image formation in this study, but is described below in relation to FCS (Section 2.3.4).

In a recent review, the three discussed techniques have been compared with respect to their S/N ratios (Lang, Baier et al. 2006). It is found that the respective S/N ratios are (a.u.): 16, 40, and 70 for WFM, TIRFM, and CLSM. The value for TIRFM is slightly lower than expected. The authors speculate that this is due to micro-scratches on the cover glass and other imperfections in the setup causing stray light.

2.3.4 Fluorescence correlation spectroscopy

Fluorescence correlation spectroscopy (FCS) measures the fluctuating fluorescence intensity in a small continuously illuminated volume over time. FCS as an applied technique was developed more or less simultaneously by two groups; the group of Webb showed it could be used to determine translational diffusion coefficients (Douglas Magde 1974; Elson and Magde 1974), while the group of Rigler measured rotational diffusion of macromolecules (Ehrenberg and Rigler 1974).

The mathematical basis for FCS is the time auto-correlation function $G(t)$, which measures the self-similarity between recorded fluorescence intensities over a time t and after a time lag $t+\tau$. As diffusion is a dynamic process, where fluorophores continuously diffuse in-and-out of the confocal volume, the extent of the auto-correlation function (ACF) is reduced as τ is increased. The ACF thus gives a measure of the time-scale τ on which the system is essentially unchanged. This time τ is in practice defined as the full-width at half maximum (FWHM) of the ACF and defines the characteristic diffusion time (dwell time) of the fluorophore in the focus.

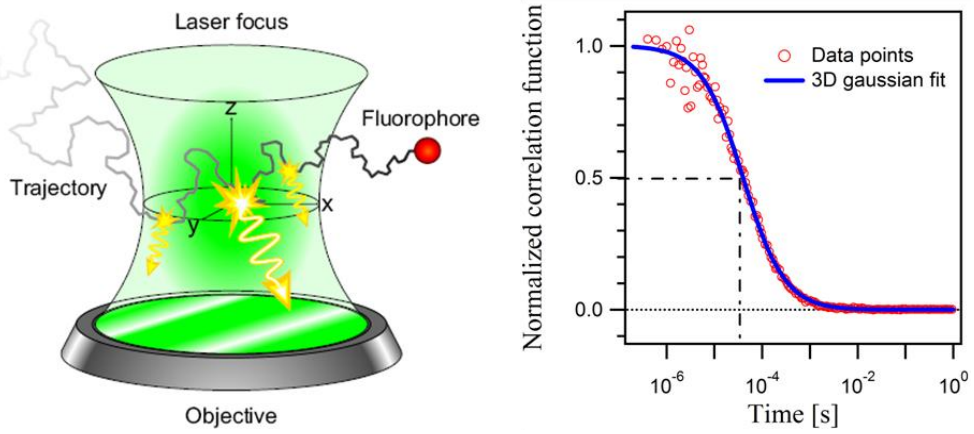

Fig. 2.10 Left: Artist impression of the laser focus. Light green area is the focal volume. Inside this, in dark green, is the observation volume. Fluorophores diffusing through the focal volume are excited with varying intensity (Image courtesy of A. Blicher, NBI) **Right:** The normalised auto-correlation function from diffusion of a small fluorophore (Rhodamine 6G) in water. At short times the correlation is high (no change in intensity), at long times the correlation is lost. The half height (dashed line) is the mean time for which the system (i.e. intensity) is essentially unchanged. (Data recorded in relation to the lipid diffusion experiments in Chapter 5).

In practice, a collimated laser beam is reflected into the objective by a dichroic mirror. Since the incident laser beam is collimated only a diffraction limited spot in the focus plane of the objective is illuminated (i.e. confocal illumination). This is a key feature of FCS as the small observation volume maximises the fluctuations in fluorescence intensity over time. Due to diffraction and the Gaussian intensity of the laser beam, the illuminated spot is a volume with a Gaussian intensity profile in the image plane (x,y -plane), while the intensity profile along the optical (z-axis) is assumed to be Gaussian, though this is still under debate (Rigler, Mets et al. 1993; Hess and Webb 2002; Blom 2003). The Gaussian approximation has been shown to become increasingly valid as the pinhole size and laser intensity is reduced (Hess and Webb 2002; Kastrup, Blom et al. 2005).

The fluorescent light, emitted from particles diffusing through the illumination volume, is focussed onto a pinhole which eliminates the out-of-focus signal and restricts the observation volume. The remaining fluorescence intensity is recorded and the fluctuations correlated according to the auto-correlation function for a three dimensional system, $G^{3D}(\tau)$ (Rigler, Mets et al. 1993)

$$G^{3D}(\tau) = 1 + \frac{1}{\langle N \rangle}\left(1 + \frac{\tau}{\tau_D}\right)^{-1}\left(1 + \frac{r_0^2 \cdot \tau}{z_0^2 \cdot \tau_D}\right)^{-1/2} \tag{2.34}$$

where $\langle N \rangle$ is the mean number of molecules in the focus, τ_D is the diffusion time through the observation volume, and r_0 and z_0 are the dimensions of the x,y-plane and z direction at which the excitation intensity is reduced by a factor of $1/e^2$. Note that the

average concentration $\langle C \rangle$ of fluorophores in the focus can be directly determined from the auto-correlation function if we assume the focal volume V_f to be ellipsoidal

$$V_f = \frac{4}{3}\pi \cdot r_o^2 \cdot z_o \tag{2.35}$$

and the mean concentration in the observation volume is

$$\langle C \rangle = \frac{\langle N \rangle}{V_f} \tag{2.36}$$

For diffusion in a two-dimensional system, e.g. monolayers, membranes, and stacked lipid layers, the contribution from diffusion in the *z*-direction is negligible and the auto-correlation function becomes (Rigler, Mets et al. 1993; Hac, Seeger et al. 2005)

$$G^{2D}(\tau) = 1 + \frac{1}{\langle N \rangle}\left(1 + \frac{\tau}{\tau_D}\right)^{-1} \tag{2.37}$$

This is the form of the ACF we have used for the analysis given in Chapter 5.

2.3.4.1 Multiple beam waist FCS – The FCS diffusion law

Recently it has been shown that it is possible to obtain information regarding the nano-scale organisation of a two-dimensional sample using FCS (Masuda, Ushida et al. 2005; Wawrezinieck, Rigneault et al. 2005; Humpolickova, Gielen et al. 2006). Such information has so far not been available due to the diffraction limited resolution (~0.5 μm) of FCS. This information can be obtained by measuring the characteristic diffusion times τ at different effective radii of focus r_{eff} and thereby at different observation times t_{obs}. This technique is sometimes referred to as Sampling-Volume-Controlled Fluorescence Correlation Spectroscopy (SVC-FCS, (Masuda, Ushida et al. 2005)), or "The FCS diffusion law" (Wawrezinieck, Rigneault et al. 2005).

As described in Section 2.1.1; if diffusion is normal over the entire range of employed observation times of the FCS experiment, then the measured diffusion coefficient D is independent of t_{obs} (and thereby r_{eff}). However, if the diffusion is confined within a domain (aka corralled diffusion) or hindered by a meshwork (e.g. the cytoskeleton) on the time and length scale of the FCS experiment, then the measured diffusion coefficient D_{obs} will be a function of time (Heimburg 2007) and thereby r_{eff}. Hindered diffusion due to hard obstacles with sub-diffraction size is cannot be resolved by this "FCS diffusion law" method, as the effect is averaged out and results in apparently normal diffusion with a macroscopic diffusion coefficient.

In practice different radii can be achieved either by varying the expansion of the collimated laser beam incident on the microscope objective (Masuda, Ushida et al. 2005), by truncating the collimated beam (Wawrezinieck, Rigneault et al. 2005), or by measuring both in- and out-of-focus on two-dimensional samples (Humpolickova,

Gielen et al. 2006). From simulation and experiments it has been shown that the relationship between the diffusion time τ and the effective radius r_{eff} can be expressed as

$$\tau = t_0 + \frac{r_{eff}^2}{4D} \tag{2.38}$$

where D is the microscopic diffusion coefficient, and t_0 is a constant. For normal diffusion or diffusion hindered by hard obstacles $t_0 = 0$. For confined diffusion $t_0 < 0$, and for hindered diffusion $t_0 > 0$ (Wawrezinieck, Rigneault et al. 2005).

For the cases where $t_o \neq 0$, it must be expected that Eq. (2.38) breaks down at relatively short observation times (and low r_{eff}), as the diffusion behaviour is expected to change from anomalous to normal in this region. However, this has not yet been observed due to the (diffraction) limited size of the focus volume.

The FCS diffusion law is not used directly in the present work, but is mentioned due to the promising features it presents. For a full derivation of Eq. (2.38), including experimental work and Monte-Carlo simulations, the reader is referred to (Wawrezinieck, Rigneault et al. 2005).

Chapter 3

Methods and materials

It has been an integral part of this PhD-project to design a monolayer trough for single molecule fluorescence microscopy and spectroscopy studies. This has to a certain extent been an iterative process as experience, requirements, and budget increased over time. In this chapter the rationale behind the design of the trough is first explained. This is followed by a justification behind the choice of microscope objective and camera lenses, as these are critical in video microscopy (Section 2.3.2). Finally, some important specifications of the final setup are given. An overview of the setup is shown at the end of the chapter (Fig. 3.2)

3.1 Monolayer trough for single molecule studies

Fluorescence studies of monolayers date back to 1981 where the first monolayer trough that could be fitted on an epi-fluorescence microscope was constructed (von Tscharner and McConnell 1981). This led to a surge in fluorescence studies on monolayers; initially driven by the discussion on the nature of the liquid-expanded (LE) to liquid-condensed (LC) phase transition as described in Section 2.2.1 (Lösche, Sackmann et al. 1983; Lösche and Mohwald 1984; McConnell, Tamm et al. 1984; Kaganer, Mohwald et al. 1999). Since then a countless number of monolayer trough designs have been published; demonstrating the versatility of the monolayer technique. Until now however no design has incorporated high numerical aperture microscope objectives (NA > 1) as required in practice for single molecule sensitivity.

Designing a trough which can be used in combination with high NA microscope objectives involves the two following main considerations:

First of all, microscope objectives with NA > 1 per definition require immersion media like water or oil in-between the objective and the sample (cf. Eq. (2.30)). Therefore it is not possible to view the monolayer from above, as this will necessarily involve that there is air in-between the monolayer and the microscope objective. Therefore, the first requirement for the trough design was that the microscope had to be an inverted type where the objective is placed below a “window” in the trough and subphase. However, this configuration would anyway have been the preferred, as it has the additional benefit that the monolayer trough can quite easily be covered with a box or similar. This is important in order to allow control of the atmosphere and the

humidity and additionally to minimise airborne contamination (e.g. dust particles) during the experiment.

The second issue is the real challenge. High NA microscope objectives have short working distances; i.e. the distance from the tip of the objective to the focal plane (see Section 2.3.2). The water immersion objective used in this study has a relative long working distance compared to many other high NA objectives, but it is still as short as 220 μm. Approximately half of this distance is typically occupied by the "window" in the bottom of the trough, which typically consists of a coverglass. This leaves only ~100 μm or less for the height of the subphase in-between the coverglass and the monolayer. In practice, a water layer of this height is virtually impossible to work with over the entire trough area. Often, parts of the monolayer trough bottom will dewet and/or the water will form discrete droplets. To avoid this, the trough was designed so that the position of the cover glass was raised 2.5 mm from the trough bottom. This was done by creating a narrow rim around the central hole in the trough (Fig. 3.1). This design allowed the vast part of the subphase to have a height of ~2.6 mm, while only the part of the subphase in-between the coverglass and the monolayer needed to be less 100 μm high.

It is possible to maintain a stable water layer with a height of only 100 μm above the coverglass; however it requires extensive cleaning of the glass surface immediately prior to use. Since the trough itself only needs cleaning with lukewarm ethanol and milli-Q water, then it is apparent that it is not practical to have the coverglass fixed to the trough bottom. It was therefore chosen to design the trough and coverglass as two separate pieces. This was done by making a stainless steel ring which fitted into the central trough hole and onto which the cover glass could be glued (Fig. 3.1). To make sure the ring would fit tightly; the ring diameter was made 5/100 of a millimetre larger than the diameter of the trough hole at room temperature. Heating the trough gently, e.g. under running tap water at ~50 - 60 °C, caused the Teflon trough and hole to expand slightly, allowing easy insertion of the steel ring. Subsequent slow cooling to room temperature, gave a leak proof fit, without any visible signs of distortions or stresses in the Teflon trough.

As briefly mentioned, the cover glasses were glued to the metal ring. For this a UV curing polyacrylate adhesive was used. This is the same type of glue used by the company Kibron (www.kibron.com) which produces commercial monolayer troughs. This glue does not dissolve in aqueous solution, which is an absolute requirement as this could generate a significant monolayer contamination. A detailed procedure for gluing the coverglasses onto the metal ring is given in the Appendix (B.3).

For the final design, it was chosen to make the barriers from a plastic known as Delrin® (POM), which has the advantage over Teflon (PTFE) that it is less hydrophobic (contact angles are ~45° and ~90° respectively). The water therefore tends to wet the POM barriers, rather than being repelled as with Teflon. This minimises the tendency for monolayers to leak under the barriers, which can be a serious problem, especially at the trough edges where the barriers and trough edges make contact. Teflon tape was placed on the barrier edges to keep water and monolayer from creeping onto the part of the POM barriers directly above the trough edges (Fig. 3.1). To further inhibit leakage

beneath the barriers at the trough edges, the barriers were shaped so they were partly submersed in the trough (and subphase). This barrier shape also provided a useful means of steering so that the barriers always moved exactly perpendicular to the trough (Fig. 3.1). Due to the very low friction of Teflon, the barriers were never observed to stick to the trough even though they fit tightly. To reduce surface flow of the monolayer in the observation region, a Teflon ring (ø 15 mm, height 3 mm) with a slit opening (2 mm) facing one of the barriers was placed on the coverglass in the trough during experiments. A second cover glass was placed on top of the ring to reduce air flow. Variations over this strategy has frequently been used for this purpose in the past (Peters and Beck 1983; Grainger, Reichert et al. 1989; Ke and Naumann 2001).

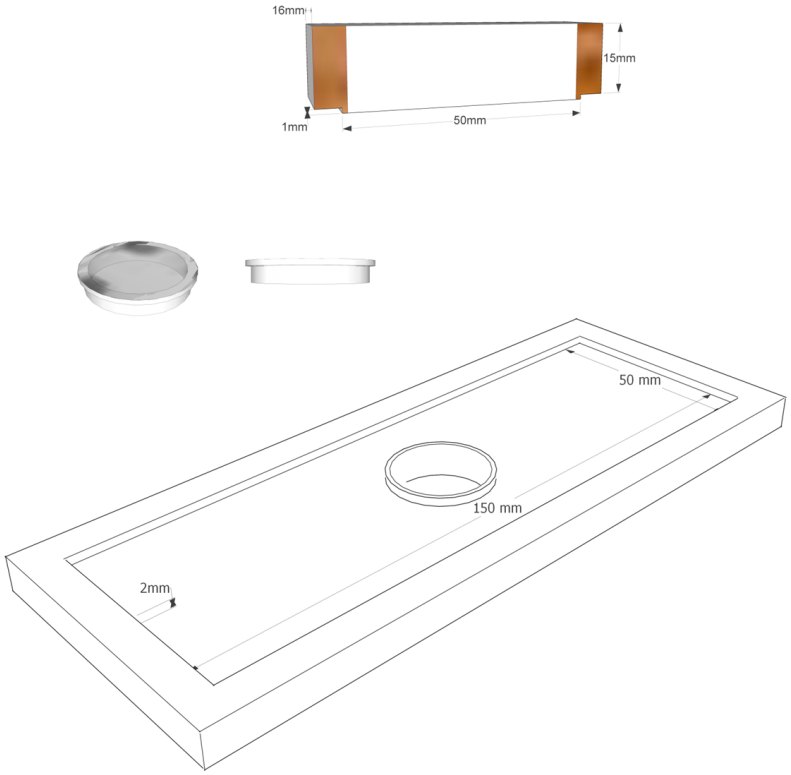

Fig. 3.1A: Barrier made from Delrin® (POM). A step near the edges was made so that the barriers are 1 mm higher in the middle than at the edges and thereby fit perfectly into the trough (below). The brown Teflon tape on the edges was necessary to avoid leakage. **B:** Bird's-eye view and side view of the stainless steel metal ring with a #00 coverglass (thickness 0.1 mm) glued on top. The diameter of the bottom part of the ring is 22.05 mm, slightly larger than the hole in the trough at room temperature. The diameter of the top part is 25 mm, fitting commercially available standard size coverglasses. The height of the top (wide) metal part, which is exposed to the aqueous phase during experiments, is 1 mm (1.1. mm including coverglass). **C:** The Teflon® trough. The diameter of the central hole is 22.0 mm at room temperature. The rectangular trough with a hole in the centre was milled from a single block. Surrounding the central hole is a rim with a height of 1.5 mm and a width of 1.0 mm. The height difference between the trough bottom and trough edges is 2 mm.

3.1.1 Microscope objective and lenses

The key component in any microscope is the objective. Two fundamental types of objectives are available which have the required numerical aperture (NA) > 1: Water immersion objectives (typically NA = 1.2), and oil immersion objectives (NA = 1.3 - 1.4). In general, the higher the NA the higher the resolution and quantum collection efficiency (see Section 2.3.2). However, since the optical observation path crosses the aqueous subphase in the trough it does not make sense to use an oil immersion objective, as the mismatch in refractive index n between the aqueous subphase (n = 1.33) and immersion oil (n=1.515) would introduce optical aberrations. This would cause loss of resolution, loss of contrast, and elongation of the focus in the direction of the optical axis (Egner, Schrader et al. 1998). It was therefore chosen early in the project to keep the 60x water immersion objective installed in the pre-existing fluorescence correlation spectroscopy (FCS) setup (described below).

Since the images are recorded on a camera with a fixed pixel array (often referred to as video microscopy) it is crucial to choose the right combination of lenses. Again, the NA of the microscope objective is the key parameter, as it together with the wavelength l of the excitation light determines the resolution R of the objective (cf. Eq. (2.31))

$$R = \frac{1.22 \cdot 532nm}{2 \cdot 1.2} = 0.27\mu m \tag{3.1}$$

According to the sampling theorem (see Section 2.3.2) the optimal resolution M_{opt} is obtained when resolvable distance spans a little more than two pixels when the signal is projected onto the camera's CCD chip. Since the Andor Ixon EMCCD camera has a pixel array of 512 x 512 pixels and the size of the individual pixels are 16 µm, then the optimal magnification M_{opt} is

$$M_{opt} \approx \frac{2px \cdot 16\mu m/px}{0.27\mu m} \approx 120 \tag{3.2}$$

The available Olympus camera lenses have magnifications of 1x, 2.5x, 3.3x, and 5x. Therefore it was chosen to combine the 60x microscope objective with the 2.5x camera lens. This yields a total magnification of 150; slightly more than the optimal magnification. A magnification of 150x means that the projected size of the sample on each pixel (referred to as "pixel-resolution") is

$$\text{Pixel resolution} = \frac{16\mu\text{m/pixel}}{150} = 107\,\text{nm/pixel} \tag{3.3}$$

From this, we can determine the "field of view" which is typically defined as the diameter of a circle. The diameter of the largest circle that can be fitted on a 512x512 pixel array with 107 nm pixels is

$$\text{Field of view} \approx 512\text{pixels} \cdot 107\,\text{nm/pixel} \approx 55\mu\text{m} \tag{3.4}$$

Two different cameras were used for the images shown in the following chapters. The key numbers for the cameras are shown in Table 1.

Table 1 Key numbers for the two different available cameras. The EMCCD camera from Andor has single photon sensitivity, and high temporal resolution. The CCD camera from Apogee has a larger field of view.

	Pixel array	**Pixel size** (μm)	**$M_{optimal}$** [1)]	**Pixel resolution** (μm)	**Field of view** (μm)
ANDOR Ixon^{EM+}	512 x 512	16	150 [2)]	107	55
APOGEE KX85	1080 x 1300	6.7	60	112	121 [3)]

1) When using a microscope objective with N.A. 1.2 and exciting at l = 532 nm.
2) Optimal magnification according to the sampling theorem is 120x. But no 2x magnifying camera lens was available. Instead, a 2.5x lens was used; yielding a total magnification of 150x
3) Diameter of a circle that fits into the shorter (1080 pixel) axis.

3.2 Laser excitation

Sample excitation was done at 532 nm using a Torus 200 mW laser (CW, TEM_{00}, $\omega \equiv 1/e^2$ = 0.85 mm) from Laser Quantum (GB). To achieve homogenous, rather than Gaussian, illumination of the sample the laser beam was first collimated and expanded. The expansion of the beam is determined by the ratios of the focal lengths of the two lenses composing the beam-expander (sometimes referred to as the telescope). With two lenses having focal lengths of 12.5 mm and 200 mm the telescope gives a 16 times magnification. As the laser emits a beam that is ~0.85 mm wide, the laser beam after expansion $w_{expanded}$ in the telescope becomes

$$\omega_{\exp anded} = \frac{200\,\mathrm{mm}}{12.5\,\mathrm{mm}} \cdot 0.85\,\mathrm{mm} = 14\,\mathrm{mm} \tag{3.5}$$

This beam is much wider than needed for illumination of the sample area under investigation. To minimise sample bleaching outside the area of interest, the beam was heavily truncated by passing it through a circular field aperture. Subsequently it was focussed on the back focal plane of the objective to form a narrow collimated beam incident on the sample. The radius of the field aperture r_{aperture} was chosen so that only a diameter corresponding to the field of view was excited ($r_{field\ of\ view}$ = 55 μm). Given the focal lengths of the focus lens and the objective, 300 mm and 3 mm respectively, the diameter of the aperture opening should be approximately

$$d_{field\,of\,view} = \frac{3\,\mathrm{mm}}{300\,\mathrm{mm}} \cdot d_{aperture} = 55\,\mu\mathrm{m} \Rightarrow r_{aperture} = 5.5\,\mathrm{mm} \tag{3.6}$$

As the field aperture discriminates a significant part of the laser beam, the laser power is decreased. The power P after the field aperture (i.e. truncation) is given by (Yura and Rose 1995)

$$P = P_0 \cdot \left(1 - e^{-d_{aperture}^2 / \omega_{expanded}^2}\right) \tag{3.7}$$

where P_0 is the power of the incident laser. Note that the opening of the field aperture required to truncate the beam outside the field of view is only dependent on the focal length of the focus lens (assuming we do not change the objective). It is independent on the radius of the incident beam; $\omega_{expanded}$. However, the power reduction due to truncation from the field aperture is very dependent on $\omega_{expanded}$.

Inserting d_{aperture} = 6 mm and $\omega_{expanded}$ = 14 mm yields

$$P = 200\,\text{mW} \cdot (0.09) = 18\,\text{mW} \tag{3.8}$$

which results in a final excitation irradiance of

$$\frac{I_0}{2} = \frac{P_0}{\pi \cdot \omega^2} = \frac{18\,\text{mW}}{\pi \cdot (55/2\,\mu m)^2} = 0.8\,\frac{\text{kW}}{\text{cm}^2} \tag{3.9}$$

where ω is the radius of the illuminated area.

This is about the excitation irradiance needed for single molecule detection (See also Appendix C.2). Table 2 shows some typical lens substitutions made for different experimental requirements. As should be apparent from the above, there is a direct trade-off between excitation irradiance and homogenous illumination, and the lowest practically possible excitation irradiance was therefore always chosen for a particular experiment.

Table 2: Field of view (FOV) and excitation irradiance ($I_0/2$) given for 150x magnification. ω_0 is the radius of laser beam at the laser opening. Aperture opening is chosen so irradiation covers an area slightly smaller than the maximum field of view. L1, L2, L3, and O denote the three lenses and the objective respective. The power of the laser line is 200 mW.

ω_0	**Focal length**		$\omega_{expanded}$	**FOV**	**Focal length**		$d_{Aperture}$	P	$I_0/2$
(mm)	(mm)		(mm)	(μm)	(mm)		(mm)	(mW)	(kW/cm²)
	L1	**L2**			**L3**	**O**			
0.85	12.5	200	14	55	300	3	6	18	0.8
0.85	30	200	5.7	55	300	3	6	85	3.6
0.85	12.5	200	14	55	500	3	5	45	1.9
0.85	30	200	5.7	55	500	3	5	157	6.7

3.2.1 Fluorescence correlation spectroscopy setup

The FCS setup was constructed by a former PhD-student, A. Hac, and is thoroughly described in her PhD dissertation and related articles (Bockmann, Hac et al. 2003; Hac 2003; Hac, Seeger et al. 2005).

For the work described herein the setup was used under the following conditions. A 5 mW, 532 nm laser running in TEM_{00} mode was expanded and collimated to 7.2 mm using two lenses with focal lengths of 5 mm and 100 mm (20 times expansion). The expanded laser beam slightly overfilled the 7 mm back aperture of the water immersion objective (Olympus 60×, UPLAPO, working distance 0.25mm, N.A. 1.2). Between beam expander and objective the laser beam was passed through an optical density filter of at least OD 3 (lowering the laser power by a factor 1000), and most often OD 3.6 (factor 4000). This was done to reduce bleaching to a minimum and in order to fulfil the criteria needed for the assumption of a Gaussian excitation intensity distribution (Hess and Webb 2002). Irradiance ($I_0/2$) using OD 3 was 0.2 kW/cm² and 0.06 kW/cm² using OD 3.6.

Fluorescence signal from the diffraction limited focus spot (radius ~300 nm) was filtered first by a dichroic mirror (cut-off 537 nm, AHF, Germany) and then a cleanup filter (Transmission 542-622 nm, OD6 outside this region, AHF, Germany). To discriminate the out-of-focus signal and to restrict the observation volume the fluorescence signal was focussed onto a pinhole of 30 μm, The remaining in-focus signal from the confocal volume was recorded on an avalanche photo diode (APD, Laser Components GMBH, SPCM-AQR-13) and time auto-correlated using a hardware correlator card (Correlator.com, Flex5000, Bridgewater, NY, USA). The use of a single APD was the only major change made to the optical path with respect to the original setup. Originally a polarising beam splitter was used to distribute the signal on two APDs. Removing the beamsplitter and only using one APD effectively doubled the S/N ratio. The payoff was the loss of ability to record in cross-correlation mode which has a slightly better temporal resolution in the nanosecond range. This is far below the needed temporal resolution for lipid lateral diffusion experiments where fluctuations occur on the millisecond timescale.

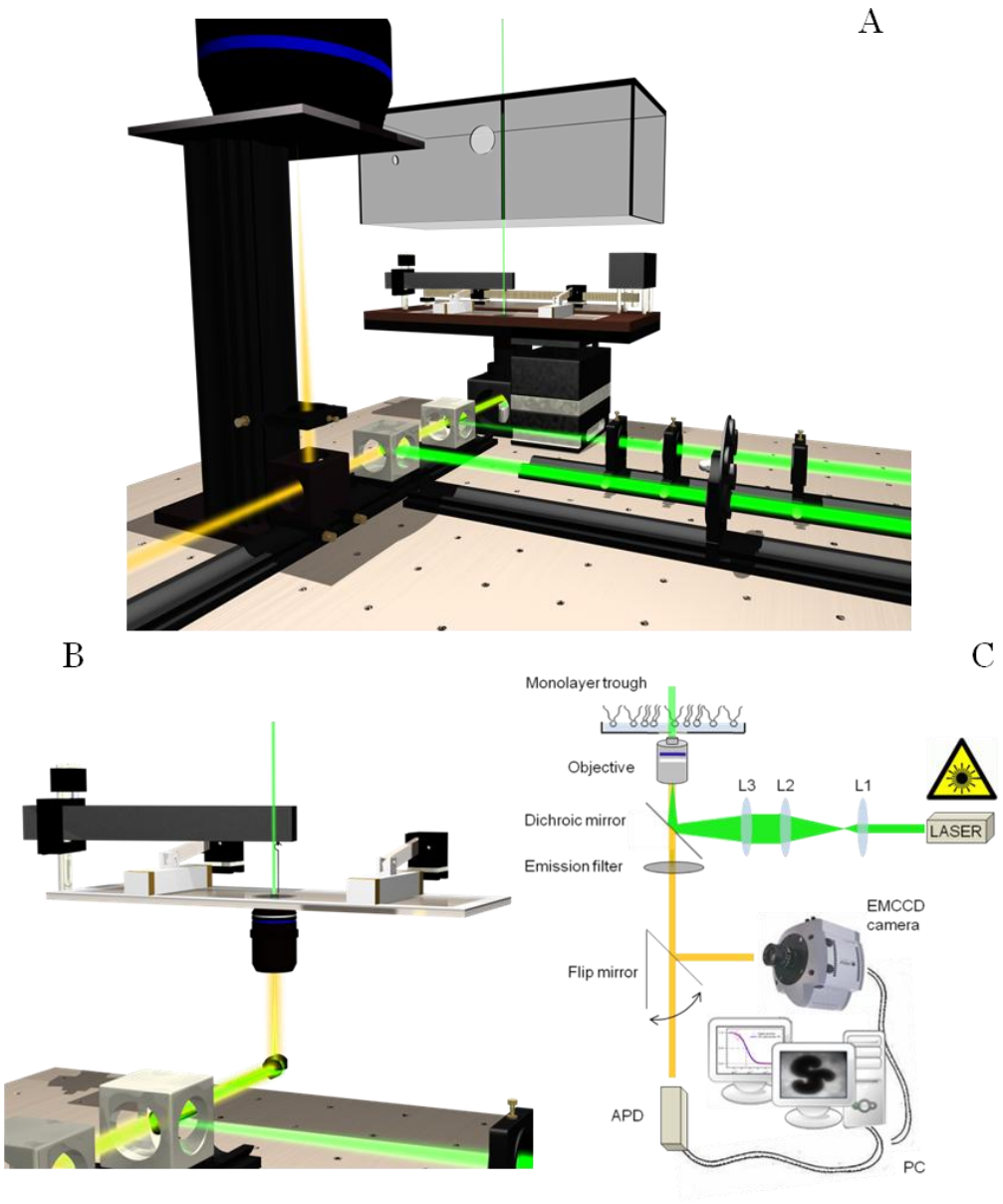

Fig. 3.2 A: Illustration of the central part of the microscope setup, with the two beam paths. One for FCS and one for WFM. **B:** Detailed illustration with the constructional elements removed. The objective is placed just beneath the Langmuir trough. **C:** Schematic of the complete setup with the lenses in WFM mode. Only one laser line is shown for simplicity. Lens 1 (L1) and lens 2 (L2) compose the beam expander. Lens 3 (L3) focuses the laser on the objective (Köhler illumination). For FCS mode Lens 3 is removed and a focussed spot is created ~200 μm above the objective. The signal is directed to either an EMCCD camera (WFM), or an APD (FCS)

Chapter 4

Morphology of DPPC monolayers

In this chapter the morphology of the two different phase co-existence regions in DPPC monolayers are visualised and discussed. Due to the particular design of our wide-field microscopy (WFM) monolayer setup, the presented WFM images were obtained at higher optical resolution than any previously published microscopy images. The first part of the chapter deals with condensed lipid domains (LC-domains) embedded in a matrix of expanded lipid (the LE-region). Then the less well-investigated region, the 'gas' (G) to 'liquid-expanded' (LE) transition region is visualised and discussed. This

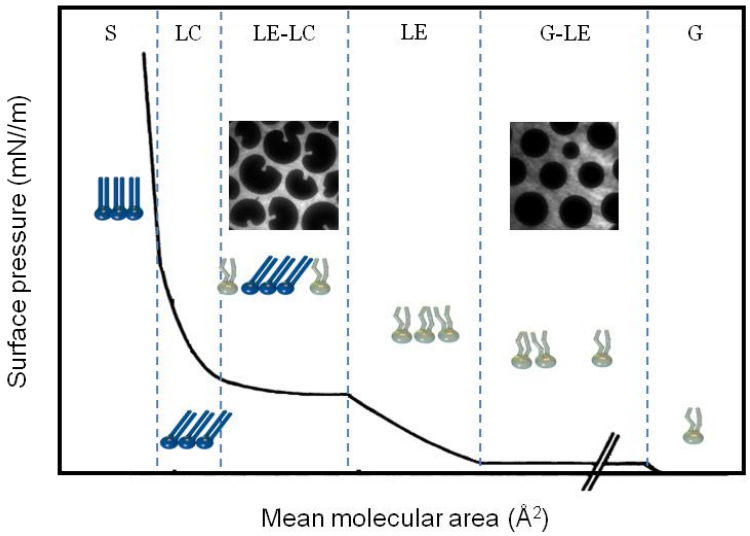

Fig. 4.1 A schematic representation of a DPPC compression isotherm. The cartoon representation of lipid molecules illustrates the lipid organisation during the compression. The monolayer is initially in a gas-phase where the lipids have negligible interaction. After full compression the lipid monolayer is shifted into a solid-phase where both lipid headgroups and aliphatic chains are highly ordered. The transition pressure of the two phase transitions; LC-to-S and 'LE-LC'-to-LC are quite subtle and often hard to determine experimentally. Note also the broken scale on the x-axis. Idealised isotherm shape modified from (Albrecht, Gruler et al. 1978; Möhwald 1995). **Images**: The bright areas are the LE-phase in which the lipid fluorophore is miscible. In the first image (G-LE phase co-existence) the dark regions are gas-bubbles (i.e. exposed air-water interface). In the second image the dark regions are LC-domains (condensed lipid structure) in a LE matrix. Images were recorded on the WFM described Chapter 3.

latter transition is extremely wide and the pure gas phase could not be achieved in our Langmuir trough by relaxation from the liquid phase. Therefore the second part of this chapter contains a theoretical model (a virial expansion) which is used to estimate the width of the G-LE phase co-existence region.

4.1 Introduction

Fluorescence wide-field microscopy (WFM) imaging is an excellent method for illustrating the complex morphology of the phase co-existence regions in DPPC monolayers, and the morphology of DPPC monolayers has been studied intensively using this method for more than 25 years (von Tscharner and McConnell 1981; Lösche, Sackmann et al. 1983; Lösche and Mohwald 1984; Lösche and Mohwald 1984). WFM has played a major role in elucidating the nature of the LE-to-LC phase transition (see also Section 2.2.1). It is now generally accepted that a DPPC monolayer can exist in four different pure phases below the critical temperature (~40 °C). These are; gas (G), liquid expanded LE, liquid condensed LC, and solid S. In addition to these there are two mixed phases; a gas/liquid-expanded phase co-existence (G-LE), and the liquid-expanded/liquid-condensed phase co-existence (LE-LC). These two phase co-existence regions (G-LE and LE-LC) are the most obvious regions to study with fluorescence WFM since most fluorescent probes partition almost exclusively in the LE region and thus give a rise to high contrast in fluorescence images. Fig. 4.1 shows the relative position of these phases in a pressure-area isotherm of DPPC.

4.2 Results and discussion

4.2.1 LE-LC phase co-existence, the shapes of LC-domains

The various shapes and periodic organisation of domains in the LE-LC phase co-existence region have been the subject of numerous studies; e.g. (Klopfer and Vanderlick 1996; McConlogue and Vanderlick 1997; Li, Miller et al. 1998; Kane, Compton et al. 2000; Kruger and Losche 2000). In brief, it has been shown that the domain shape and the periodic structure of the monolayer is the result of competition between molecular chirality, line tension, and electrostatic interactions. It has also been shown that experimental conditions play a large role on the appearance of monolayers. For instance, the concentration of the lipid spreading solution and the compression rate may affect the size of the domains drastically (Li, Miller et al. 1998). Some representative domain shapes are shown in Fig. 4.2: The LE-phase is seen as a homogonous (no contrast) region (Fig. 4.2A). Upon compression into the LE-LC region, domains (dark regions) start forming (Fig. 4.2B) which are arranged on a hexagonal super-lattice in the LE lipid matrix (bright region). Continued compression brings the monolayer into the LC phase, where the domains initially get blurry (Fig. 4.2C) and finally disappear completely. However this latter effect is, as will be discussed in Section Chapter 5, to a certain degree dependent on the relative amount of the lipid fluorophore.

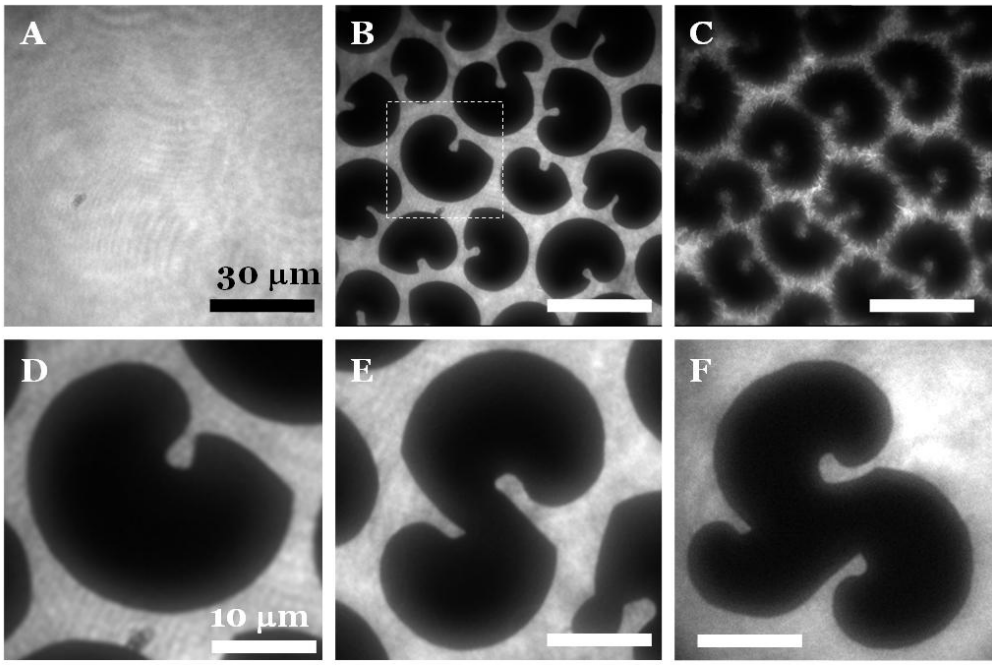

Fig. 4.2 Six representative images showing various phases and domain shapes during the compression of a DPPC monolayer (0.1 mol% TRITC-DHPE). LE-regions are bright and LC-domains are dark. **A:** The homogenous LE-phase **B:** The LE-LC phase co-existence; most of the domains are bean shaped, but three of the domains are beginning to transform into S-shapes. **C:** The beginning of the LC-phase; upon further compression the contrast is lost. **D-E**: The classical domain shapes frequently observed in the LE-LC phase (shown in order of decreasing mean molecular area). Note that one of the lobes of the bean in image D is more flat than the other lobe; an effect caused by packing of the chiral DPPC molecules.

A few of the possible and well-described domain shapes found in the LE-LC region are shown in Fig. 4.2D-F. In the beginning of the LE-LC region, the bean shaped domains constitute the preferred structure. During the transition, an extra lobe forms (always from the more flat lobe) creating S-shaped domains with two round end lobes (Fig. 4.2D, see also Fig. 4.2B). At the end of the region trilobed domains are formed, and again with the new lobe emanating from the flat (now central) part of the domain (Fig. 4.2E). Performing the compression at a higher rate sometimes creates domains with even more lobes. Previous studies have shown that all of these domain shapes gradually relax, and after 10 hours of aging become more or less circular (Klopfer and Vanderlick 1996).

4.2.2 The G-LE phase co-existence region

In spite of the maturity of the monolayer technique, and the countless number of studies on DPPC monolayers, most authors tend to disregard one of the co-existence phases; namely the G-LE region. However, as will be shown in the following, some very interesting and fundamental phenomena occur in this phase.

Ahead of presenting and discussing the results, it should be stressed that the experiments were performed under non-equilibrium conditions as the monolayer relaxation (i.e. the opposite process of compression) was too fast to allow for monolayer equilibration. Attempts were made, but it does not appear to be practically possible to perform the relaxation under equilibrium conditions.

When the area available for a monolayer, which is initially in the LE-phase, is increased at a rate higher than the rate at which the monolayer lipid can redistribute across the lipid-water interface, then 'holes' are created in the lipid monolayer. These 'quasi-two-dimensional areas void of lipid' are hereafter referred to simply as gas-bubbles.

A series of images recorded at increasing MMA is shown in Fig. 4.3. In this experiment, the relaxation was done at the highest possible rate at which the monolayer plane could be kept in the optical focus of the microscope (~5 Å²/lipid/min). As shown, fast relaxation caused quite large gas-bubbles to form at mean molecular areas just a few square-angstroms from the LE-phase. In contrast, when the relaxation was done at 0.5 Å²/lipid/min, then the homogenous appearing phase seen in image Fig. 4.3A could be maintained for much larger molecular areas (at least 150 Å²). A general explanation for this may be that in the G-LE region which is close to the LE-phase, small air bubbles spontaneously form (due to density fluctuations) and collapse (due to line tension) in a

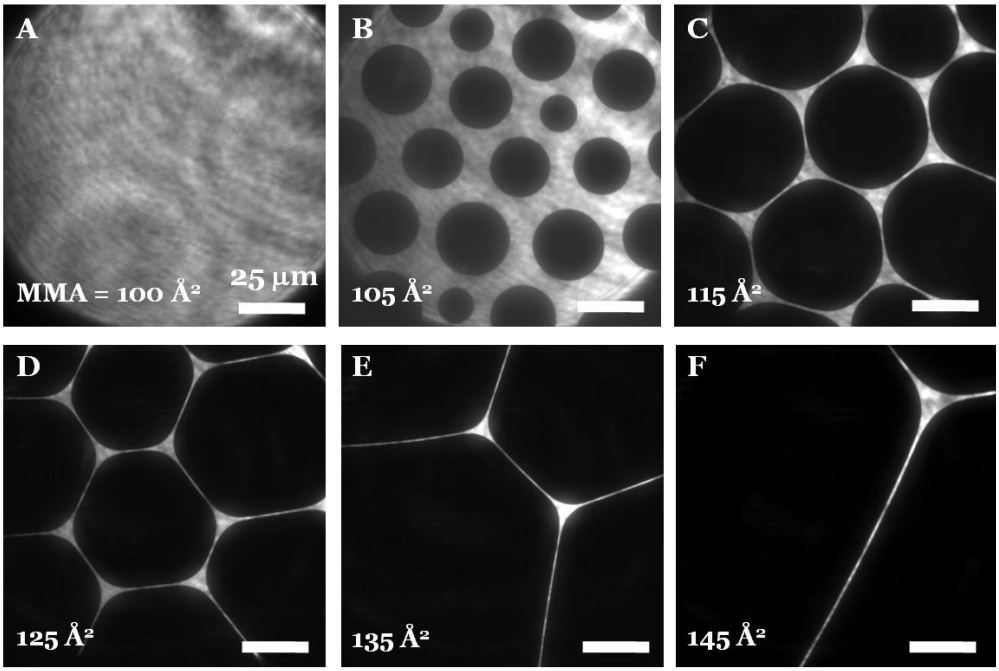

Fig. 4.3 DPPC monolayer (0.1 mol% TRITC-DHPE) during isothermal relaxation. Bright regions are lipid (initially LE phase), and dark areas are (quasi-) two-dimensional gas bubbles (i.e. air-water interface). The gas bubbles are formed as a consequence of fast non-equilibrium relaxation of the DPPC monolayer. In the last image shown (F) the monolayer "string" spans more than 100 μm and the width of the string is near the diffraction limit.

highly dynamic process. These dynamic gas-bubbles were never observed in the microscope images and are therefore expected to be below the optical resolution. However, if the monolayer was relaxed at high rate (>2 Å²/lipid/min), some of these dynamic gas-bubbles were stretched to a size where they became meta-stable. This is comparable to the phenomena of undercooling of (3D-) fluids, where a substance may retain its fluid structure below its freezing temperature if the temperature is shifted too quickly for the molecules to arrange into an ordered (solid) structure. Gas-bubbles with a size on the order of the diffraction limit were observed to be at least meta-stable, so the critical size at which the meta-stable bubbles are reached must be on the order of 0.5 μm.

It is also apparent that the area inside the gas-bubbles increases much faster than one would expect from the relative change in mean molecular area. For instance, when the MMA available for DPPC is increased by 35% from 100 Å² (Fig. 4.3A) to 135 Å² (Fig. 4.3E), then the lipid region covers less than 10% of the water surface. As a consequence of this inconsistency, it would be unlikely if the monolayer structure seen in Fig. 4.3 covered the entire trough area. Indeed, when the monolayer was translated over the microscope objective, a linear phase boundary between two inverted phases was often observed (Fig. 4.3). Two typical types of phase boundary regions are shown in Fig. 4.4. Notice how the phase boundary resembles the cross-section of a liquid at its boiling temperature.

During the experimental series, it was obvious that the homogenous 2D-gas phase predicted in Fig. 4.3 was never reached. In order to get a feeling for the width of the G-LE transition region, and thereby the position of the gas phase in terms of mean molecular area, a virial expansion of a DPPC isotherm was performed and extrapolated into the G-LE region.[3] A virial expansion expresses the pressure in a real gas as an infinite power series depending only on the density of the lipid. In the form relevant for a monolayer, it reads

$$\Pi = \pi_1 \frac{a_o}{a} + \pi_2 \frac{a_o^2}{a^2} + \pi_3 \frac{a_o^3}{a^3} + \pi_4 \frac{a_o^4}{a^4} + ... \qquad (4.1)$$

where the surface pressure Π only depends on the mean molecular area a (at constant temperature), π_n are the virial fit coefficients, and a_o is a chosen fixed length scale ($a_o \equiv$ 100 Å²). The virial (latin for force) coefficients describe the interaction of the particles in the system. Truncating the virial expansion to only one term (π_1) reduces Eq. (4.1) to the ideal gas law, and so this coefficient describes ideal behaviour, whiles the second, third, etc. virial coefficient accounts for the deviation from ideal behaviour.

The pressure changes associated with the expansion and relation in the G-LE region are below the resolution of our Langmuir balance. This means that the virial expansion has to be fitted only to data points in the LE-phase. For the actual fitting procedure, the data set for DPPC at 38.5 °C was chosen as it contains the largest LE region of the isotherm available. The fit is made to the LE-phase data, and then extrapolated into the

[3] Virial expansion was suggested and performed by Prof. Benny Lautrup, NBI, University of Copenhagen.

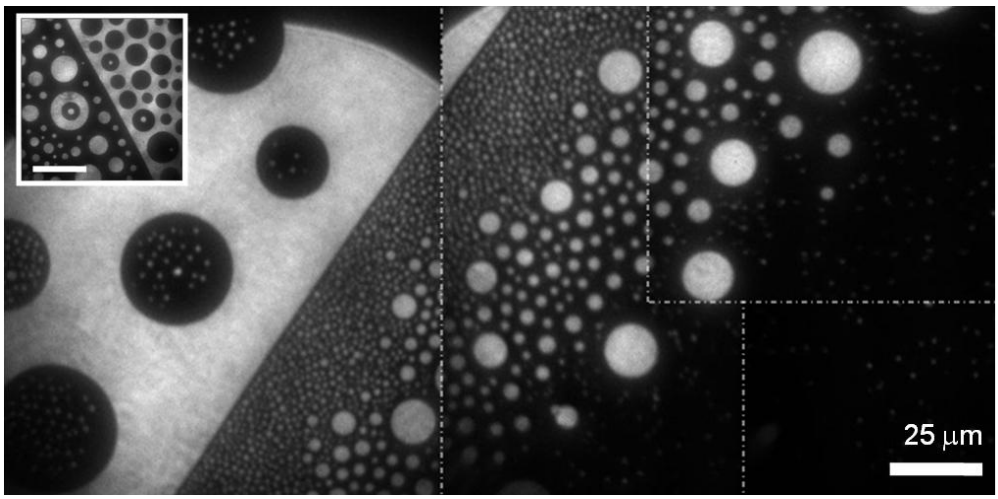

Fig. 4.4 Four separate images combined to create a mosaic showing the monolayer morphology in the area near the phase boundary. In the left side of the mosaic, a linear phase boundary between the two inverted phases is seen. Monolayer was DPPC (0.1 mol% TRITC-DHPE) at MMA ~120 Å² (21-22 °C). The edges of the individual images composing the mosaic are shown as dotted lines. Since the gas bubbles and lipid domains were in constant movement, the features near the edges do not overlap perfectly in the mosaic. **Inset:** Another type of phase separation boundary often observed. The overall features are similar to the larger mosaic, but the size and distribution of the bubbles vary (scale bar is 25 μm).

G-LE region and the gas (G) phase. The precision of the fit would benefit from a data point in the G-LE region. At present this is unfortunately not available.

The first coefficient, the anchor value for a approaching infinity, can be determined prior to fitting from the expression;

$$\pi = \frac{k_B T}{a_0} \tag{4.2}$$

which is basically the 2D-version of the well-known ideal gas law, where the mean molecular area a is given by the number of particles n at a given total area A ($a = n/A$). The ideal gas equation is considered a good approximation for a approaching infinity, as the particles at high a must experience negligible interaction; e.g. attraction and excluded area.

For the chosen length scale a_0 = 100 Å² and the temperature corresponding to the experimentally determined fitting values from the DPPC isotherm; T = 38.5 °C, we get π_1 = 4.3 mN/m. The other coefficients are found by fitting to the experimental data. Within the LE-phase, the fit is nearly perfect with a root-mean-square error $\Delta\Pi$ = 0.1 mN/m, and yields three further coefficients

$$\pi_2 = -33.68\,\text{mN/m}, \qquad \pi_3 = 37.33\,\text{mN/m}, \qquad \pi_4 = 7.95\,\text{mN/m}\,. \tag{4.3}$$

At least four coefficients were necessary to get a good fit. The extrapolated virial fit is shown in Fig. 4.5. The shape of the virial fit has the expected appearance of a Maxwell construction for a first-order gas-to-liquid phase transition.

The following values were found from the fit: The cross-over to negative pressure is located at a mean molecular area of 99.98 Å², the minimum is found at 149 Å² (point A in Fig. 4.5, inset), the cross-over to positive pressure is found at 655 Å², and the maximum at 1381 Å² (point C).

The tie line shown in Fig. 4.5 (right) signifies the equilibrium state for the G-LE phase co-existence. Its value is determined by considering the G-LE phase co-existence equilibrium conditions. As usual we will express the free energy as the Helmholtz free energy F (Section 2.2) and the relevant variables

$$F = F(A,n) \tag{4.4}$$

First, a new extensive variable for the mean molecular area a is created from the two (experimentally controlled) extensive variables; number of particles n and total available area A

$$a = \frac{n}{A} \tag{4.5}$$

The variable a is usually referred to as MMA, but for the present treatment we will keep to the shorter notation a (except for the graphical representations).

Under equilibrium conditions, the two-state (gas and liquid) system is described by

$$F = F_1(A_1,n_1) + F_2(A_2,n_2) \tag{4.6}$$

Since the surface tension and the chemical potential is given by

$$\gamma = \left(\frac{dF}{dA}\right)_n, \qquad \mu = \left(\frac{dF}{dn}\right)_A \tag{4.7}$$

the differential two-state free energy becomes

$$dF = \gamma_1 dA_1 + \mu_1 dn_1 + \gamma_2 dA_2 + \mu_2 dn_2 \tag{4.8}$$

At constant area a and particle number n the minimum in free energy $dF = 0$ is obtained for

$$\gamma_{LE}(a_{LE}) = \gamma_G(a_G) \tag{4.9}$$

$$\mu_{LE}(a_{LE}) = \mu_G(a_G) \tag{4.10}$$

We already know the values for the area determined surface tension $\gamma(a)$ from the virial fit in Eq. (4.1), and the values for $\mu(a)$ can be determined from a virial fit to the chemical potential

$$\mu(a) = \int aq'(a)da = a_0\left(\pi_1 \log\frac{a_0}{a} + 2\pi_2\frac{a_0}{a} + \frac{3}{2}\pi_3\frac{a_0^2}{a^2} + \frac{4}{3}\pi_4\frac{a_0^3}{a^3}\right) \tag{4.11}$$

A solution to the two virial expansions in Eq. (4.1) and Eq. (4.11) which satisfy Eq. (4.9) and Eq. (4.10) yield the following values for the equilibrium areas in the LE and G-phase

$$a_{LE} = a_0 - 0.176 = 99.8\ \text{Å}^2 \tag{4.12}$$

$$a_G = 14048\ \text{Å}^2 \tag{4.13}$$

Thereby the mean molecular area at which a pure gas-phase is reached (a_G) has been determined to the accuracy that our data allows. This theoretical value readily explains why we never observed the pure gas phase: It would require a 140 times expansion of the monolayer from the liquid phase to reach the gas phase ($\sim a_G/a_{LE}$).

Since the tie line in Fig. 4.5 (right) per definition is horizontal then the two equilibrium areas for the LE-phase and G-phase have the same corresponding pressure

$$\Pi_{G-LE} = 0.0276\,\text{mN/m} \tag{4.14}$$

According to Maxwell, the states along the curve between a_{LE} and point A as well as the states along the curve point C and a_G are meta-stable states, the tie-line is the equilibrium state, while the remaining points on the solid curve between a_{LE} and a_G (point A to C) correspond to thermodynamically unstable states; at these points the area should increase when the pressure is increased ($d\Pi/da > 0$). Such states do not exist.

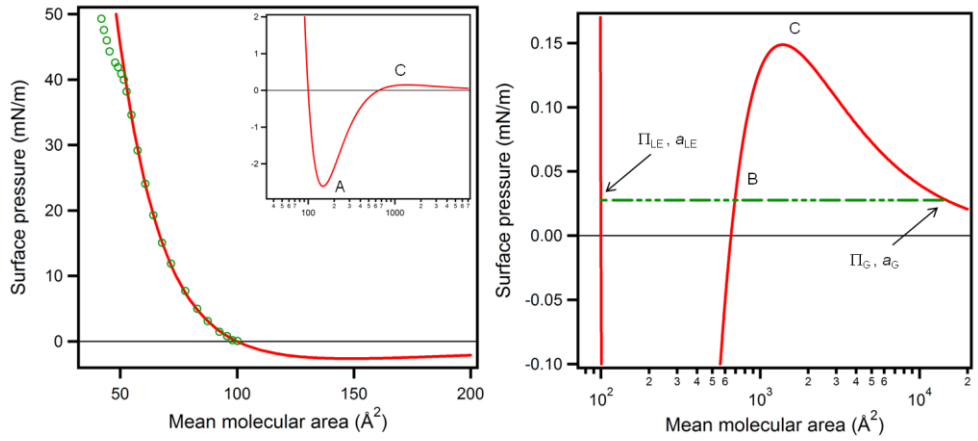

Fig. 4.5 Left: Virial fit (red solid line) to experimental data: DPPC isotherm at 38.5 °C (points, not all data points are shown). **Left inset:** Detailed representation of the fit near zero surface pressure and the onset of the G-LE region. Note the logarithmic abscissa (Axis labels are the same in all graphs). The appearance of the virial fit is similar to a Maxwell construction of the van der Waal's equation for the fluid-to-gas first order transition. **Right:** Detailed representation of the virial fit in the G-LE region. According to Maxwell, the system is in thermodynamic equilibrium at all points along the tie line (green broken line). The zero line is defined as the surface pressure of pure water in the absence of any particles.

4.3 Conclusion

The two different phase co-existence regions of a DPPC monolayer were directly visualised. Using our newly built wide-field microscope and Langmuir trough setup, the intricate shapes of LC-domains in the LE-LC phase co-existence region could be resolved at higher optical resolution than in any previously published studies. These images clearly revealed the asymmetry of the classical (kidney) bean shaped LC-domain structures. As often reported in the literature, upon further compression into the LE-phase and further into the S phase, the image contrast disappeared and the lipid fluorophore appeared uniformly distributed in the monolayer. We shall see later that this is not always the case (Section 5.2.2).

The often neglected G-LE phase co-existence region was also investigated by direct visualisation of the formation of perfectly circular 2D-gas bubbles. This process was found to be highly dependent on the rate of monolayer relaxation (i.e. the speed of the trough barriers). High relaxation rates resulted in formation of large gas-bubbles at mean molecular areas (MMA) just a few square-angstroms from the pure LE-phase. On closer inspection of the morphology of the G-LE region, an inverted phase was also found which in part could account for the stability of the relatively large gas-bubbles.

The width, in terms of MMA, of the G-LE region was determined by fitting experimental data to a virial expansion. The virial fit resulted in a Maxwell construction of a first-order gas-to-liquid phase transition. From virial fits to both surface pressure and chemical potential, an estimate of the equilibrium areas of the LE-phase and G phase was found; a_{LE} = 99.8 Å^2 and a_G = 14048 Å^2. Even though the precision of the fit could be improved with a reliable data point in the G-LE region, the fit strongly implies that lipid monolayers, when spread at the air-water interface, are generally in the G-LE phase co-existence region and not in the G-phase as often implied.

Chapter 5

Lipid diffusion in monolayers

In this chapter, the first of two single molecule studies is presented. In the first part, fluorescence correlation spectroscopy (FCS) has been used to study the diffusion behaviour of a lipid fluorophore in a DMPC monolayer as a function of pressure. It is shown that the obtained data fit the free area model well. It will also be shown that there is a good correlation between the diffusion coefficient and the thermodynamic variable surface pressure Π. In the second part of the chapter, single molecule wide-field fluorescence microscopy (SM-WFM) was used to visualise the distribution of a fluorophore in a DPPC monolayer in the LC and S phase. The fluorophore was contrary to common belief seen to partition selectively near the grain boundaries between the residual LC-domains.

5.1 Introduction

Lipids and their lateral diffusion play an important role in many biological processes, and have as a scientific topic had a renaissance in the past decade, partially motivated by the lipid raft hypothesis (also known as detergent resistant membranes DRMs); see e.g. (Saxton 1999; Edidin 2003).

Lipid diffusion in biological and model membranes has been studied by fluorescence techniques for more than 30 years with pioneering work including; (Devaux and McConnell 1972; Sackmann and Trauble 1972; Galla and Sackmann 1974; Razinaqv, Behr et al. 1974). The different modes of diffusion are now quite well-described and understood; e.g. free diffusion, hindered/obstructed diffusion, and confined diffusion (see Section 2.1). Experimental data for lipid diffusion in a lipid matrix has generally been shown to fit the free-area model proposed by Galla et al. quite well (Galla, Hartmann et al. 1979; Peters and Beck 1983; Almeida, Vaz et al. 1992; Ke and Naumann 2001). However, there is still a need for evaluating different model systems with respect to the free-area model before it becomes actually predictive; for a discussion see e.g. (Xiang 1999; Falck, Patra et al. 2005). To this end a versatile experimental platform is required in which individual parameters can be varied over a broad range (e.g. composition, pH, salt concentration). An experimental technique that satisfies many of these requirements for a model system is the Langmuir technique (Brockman 1999).

A variety of fluorescence techniques have been applied to investigate lipid diffusion on different length and time-scales. fluorescence recovery after photo-bleaching (FRAP)

has since the invention in the mid-seventies (Axelrod, Koppel et al. 1976) been by far the most frequently applied technique; for a recent review see (Sprague and McNally 2005). In FRAP, fluorophores within an area of typically a few micrometres are bleached, and the time until the area has been replenished via diffusion with non-bleached fluorophores is measured. Typical recovery times are on the order of seconds. Another fluorescence technique, which is becoming increasing popular, is single particle tracking (SPT) using wide-field microscopy (WFM). SPT is a powerful technique with the potential to reveal a wealth of information, most noticeably the strong point of SPT is often argued to be the ability to disclose distributions rather than ensemble properties (Schmidt, Schutz et al. 1996; Saxton and Jacobson 1997). The time and length scale of SPT is from tens of nanometres to a hundred micrometres, and timescales ranging from milliseconds to seconds. In practice this range is limited though by bleaching effects when organic fluorophores are used as probes. SPT also often requires image post-processing due to a low S/N ratio, and extensive data analysis of many individual tracks in order to obtain reliable statistics (Qian, Sheetz et al. 1991). Fluorescence Correlation Spectroscopy (FCS) offer a compromise between FRAP and SPT. FCS has single molecule sensitivity, the highest temporal resolution of the three, and readily measures thousands of diffusion events in a matter of seconds giving reliable diffusion coefficients at short acquisition times (Elson and Magde 1974; Webb 1974; Hac, Seeger et al. 2005; Saxton 2005; Schwille and Garcia-Sáez 2007).

The different modes of diffusion were discussed in Section 2.1, with a special emphasis on the effect of the temporal and spatial resolution of the applied technique (e.g. SPT, FCS, or FRAP). For the discussion presented below, it is practical to restate the most relevant diffusion expression

$$\left\langle r^2 \right\rangle = 4Dt^{\alpha} \tag{5.1}$$

where $\alpha = 1$ if the diffusion is normal (free, unhindered), and $0 < \alpha < 1$ if diffusion is anomalous (hindered).

In the current study results from FCS and single molecule sensitive wide-field fluorescence microscopy (SMS-WFM) investigations on two different monolayer systems are presented:

- Diffusion coefficients of the lipid fluorophore TRITC-DHPE in a DMPC monolayer was measured as a function of surface pressure and fitted according to the free-area model and directly to the mean molecular area MMA.
- Images of the distribution of single DiI(C18) lipid fluorophores in a DPPC monolayer at high surface pressure. The images, which show inhomogeneous partitioning of the probes in the lipid matrix, demonstrate a fundamental challenge inherent to many fluorescence experiments. Such images are seemingly absent in the literature.

It is the ambition of this study to show that FCS can be applied to monolayer studies and that FCS performed at multiple effective radii (i.e. varying focus) can be used to increase the accuracy of the measured diffusion coefficients. Parenthetically, it was also

found interesting to measure and compare diffusion coefficients from lipid monolayers with those of solid supported bilayer stacks recorded on the same optical setup by our group previously (Hac 2003; Hac, Seeger et al. 2005). Such studies of complementary systems measured on the same setup are rare, but valuable since they may reveal possible instrumental artefacts. In the following, fluid and gel, will denote lipid bilayer phases. For monolayers the usual nomenclature will be used (LE, LC, and S)

5.1.1 Theory

5.1.1.1 Free-area model

The two-dimensional free-area model (FAM), directly adapted from the three-dimensional free-volume model (Cohen and Turnbull 1959; Macedo and Litovitz 1965; Galla, Hartmann et al. 1979), has become the preferred model for describing the lipid diffusion coefficient D in a lipid matrix. The original FAM expression proposed by Galla et al. is given by

$$\ln D = \ln(g l_c u) \cdot \frac{-\gamma \cdot a_c}{a_f} \tag{5.2}$$

in which g is a geometric factor, l_c the average free length of travel, u the gas kinetic velocity of the diffusing particle, γ is a geometric factor correcting for overlap of free areas ($0.5 < \gamma < 1$), a_c is the critical area above which translational diffusion becomes possible, and a_f is the average free area per lipid molecule in the lipid matrix. These parameters were all described in detail in Section 2.1.3.

A more rigorous free area model has later been proposed by Macedo and Litovitz (Macedo and Litovitz 1965) in which the temperature dependence of D is expected to be more pronounced than in the original expression

$$\ln D = \ln\ A_o D(a_c)\ +\ -E_a/k_B T\ \cdot\ -\gamma \cdot a_c/a_f \tag{5.3}$$

For the analysis presented below both equations (5.2) and (5.3) can be re-written as

$$\ln D = \ln D_{\max} - \frac{\beta}{a_f} \tag{5.4}$$

where β is the product of the correction factor γ and the critical free area a_c, and $D_{\max}$, the diffusion coefficient for $a_f \rightarrow \infty$, is given by either

$$D_{\max} = g l_c u \tag{5.5}$$

or

$$D_{\max} = A_o D(a_c) \cdot (-E_a/k_B T) \tag{5.6}$$

for Eq. (5.2) and Eq. (5.3) respectively.

5.2 Results and discussion

5.2.1 Lateral lipid diffusion in DMPC measured by FCS

The pressure vs. area compression isotherms of DMPC at 20 ± 0.5 °C and 22 ± 0.5 ° are shown in Fig. 5.1 (left). The isotherms have similar traits to those previously reported; e.g. (Albrecht, Gruler et al. 1978; Nielsen, Bjornholm et al. 2007), showing the pressure onset at a mean molecular just below 100 Å² and gradual increase until the onset of a continuous phase transition at a pressure above 40 mN/m. A narrow co-existence region is observed at 20 °C and 22 °C, while no transition is observed at 25 °C (data not shown) demonstrating that the critical temperature T_c for a DMPC monolayer on a pure water surface lies at 23-24 °C. This is slightly higher than the critical temperature T_c ~20 °C reported by (Nielsen, Bjornholm et al. 2007) for a monolayer spread on an aqueous subphase containing sodium chloride, but in the same range as values reported for extruded DMPC vesicles (Ebel, Grabitz et al. 2001). The position of the co-existence

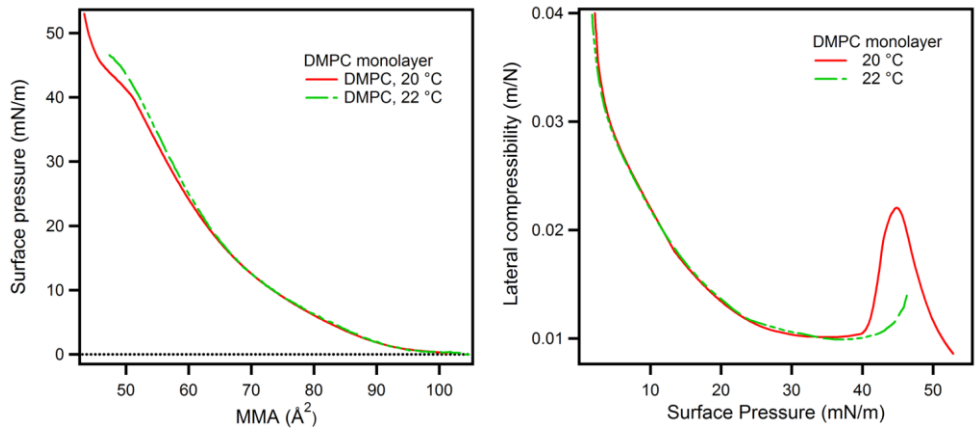

Fig. 5.1 left: Pressure-area isotherms of DMPC at 20 °C and 22 °C (recorded until monolayer collapase). **Right**: Compressibility κ_T vs pressure Π. The curve for data at 20 °C has minima near 34 mN/m (~onset of phase transition) and a local maximum at 45 mN/m. The plot of the data for 22 °C is incomplete due to monolayer instabilities/collapse observed at temperatures close to the critical temperature T_c (see also left panel).

region can be deduced from the plot of compressibility κ_T vs. surface pressure Π in Fig. 5.1 (right), or its derivatives (not shown, see also Section 2.2.1).

Fig. 5.2 (left) shows the result of a typical time-dependent z-scan. The time needed for the monolayer to move through the observation volume was 10 minutes in this case (only the time interval providing traces with adequate S/N ratio for fitting is shown). At the beginning of the scan the monolayer is out-of-focus. This means that the observed

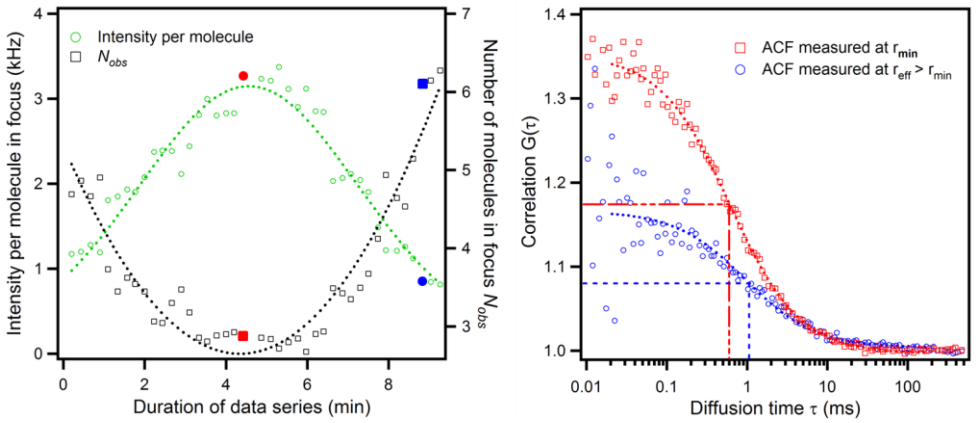

Fig. 5.2 A typical data set from a time-dependent z-scan recorded on a DMPC monolayer at Π = 26 mN/m. Highlighted data points in the left figure correspond to experimental data in the right panel **Left**: The 'intensity per molecule' (◦) increases over time as the air-water interface position first moves towards the optimal focus (0-4 minutes), and then decreases as the monolayer moves past the optimal focus (6-8 min). The number of molecules (N_{obs}, ▫) within the focus acts oppositely, and has minima at the optimal focus (~4-6 min). The fit to the intensity per molecule is Gaussian, and the fit to the number of molecules in the focus is parabolic; cf. Eq. (5.9). The fits were not used analytically and only serve as a guide for the eye. **Right**: Two measured time-ACF curves including fits: One recorded near the optical focus r_{min} and therefore measures fluorescence fluctuations from the smallest possible area, with the fewest possible number of fluorophores in the focus giving the highest possible amplitude, and the shortest possible diffusion time. The other FCS trace was recorded "out-of-focus" which results in the opposite characteristics. Note the semi-logarithmic axes.

area is large which results in relatively many lipid fluorophores N residing in the observation area. It also results in the typical diffusion time τ for a lipid fluorophore being relatively long. At intermediate times, the monolayer is near the optical focus plane; the observation area is the smallest possible (radius = r_{min}) and the diffusion time is also at a minimum. At the end of the scan the monolayer has again moved out-of-focus. Under ideal conditions, e.g. the monolayer moving through the focus at constant speed, the profile of the intensity per molecule vs. time should have a Gaussian profile according to the Gaussian approximation of the FCS beam profile. In addition, the number of molecules in focus vs. time profile should be parabolic. However, the air-water interface did not move at constant speed in all the measurement. Therefore, the fits shown in Fig. 5.2 (left) were not used analytically. Note also that the parabolic fit minima and the Gaussian fit maxima do not correspond to the same measurement. This phenomena was always observed, and has previously been observed (Benda, Benes et al. 2003). For the experimentalist working on two-dimensional (flat) samples, it is important to note that apparently one does not obtain the highest intensity per molecule at beam-waist minimum due to scattering effects (Benda, Benes et al. 2003).

In Fig. 5.2 (right) two auto correlation functions are shown: One corresponding to an in-focus measurement (red curve), and one to an out-of-focus measurement (blue curve). From the fits to the time-ACF's the average diffusion time τ through the FCS focus volume can be determined as the full width at half maximum (FWHM), and the

average number of molecules N in the focus can be found from the reciprocal value of the amplitude of $G(\tau) - 1$ (cf. Eq. (2.34)). All the time-ACF's presented herein could be fitted satisfactorily using Eq. (5.1) with an α-value of 1. This indicates that diffusion was normal on the length and time-scale of the experimental conditions, and that there was no significant surface flow present during the measurements.

The diffusion coefficients were determined from approximately 60 measured pairs of values for the diffusion time τ and the observed number of fluorophores N_{obs} in the focus. This approach makes use of measurements made both in-focus and out-of-focus, which is possible when we know (i) the number of TRITC-DHPE molecules N_{min} at the optimal focus and (ii) the radius of the optimal focus r_{min}. The lowest values of N_{obs}, found near the minima of the parabola in Fig. 5.2 (left), defines N_{min}, while r_{min} is found from external calibration. With this pair of values (r_{min}; N_{min}) at hand, the surface density of fluorophores Γ in the monolayer can be expressed as

$$\Gamma = \frac{N}{Area} = \frac{N_{\min}}{\pi \cdot r_{\min}^{\ 2}} \tag{5.7}$$

Assuming that the density of fluorophores Γ does not depend on the size of the observed area A_{obs}, which is fair for a homogenous system, we can now determine the area of any out-focus-measurement from the number of molecules N_{obs} in the area obtained from the time-ACF fit

$$A_{obs} = \frac{N_{obs}}{\Gamma} \tag{5.8}$$

From this we can find the effective radius of focus r_{eff} as a function of N_{obs}.

$$r_{eff} = \sqrt{\frac{N_{obs}}{\Gamma \cdot \pi}} \tag{5.9}$$

By combination of equations (5.1), (5.7) and (5.9) we get

$$D = \frac{r_{eff}^2}{4 \cdot \tau} = \frac{r_{\min}^{\ 2}}{4 \cdot \tau} \cdot \frac{N_{obs}}{N_{\min}} \tag{5.10}$$

In equation Eq. (5.10) the ratio N_{obs}/N_{min} is used to correct for out-focus measurements. The correction could also be done if the surface density was known exactly; e.g. from the lipid solution from which the monolayer is spread. However, the surface density of fluorophores Γ is subject to larger uncertainty than the ratio N_{obs} / N_{min}. This is due to simple weighing errors when making the stock solutions, bleaching, etc. Therefore the analysis in the following makes use of the N_{obs}/N_{min} ratio.

The most straightforward method to determine the corrected diffusion coefficient D is to plot the diffusion time τ as function of the ratio N_{obs}/N_{min} (Fig. 5.3) where the slope is given by; slope = r_{min}^2 / $4D$ cf. Eq. (5.10). Experimental data obtained at different pressures are shown in Fig. 5.3 (left). All lines passed through the point (τ; N_{obs}/N_{min})(0;0±0.1) indicating that diffusion was normal over the entire range of measured values according to the FCS diffusion law (Section 2.3.4.1). In principle this

plot also contain information on the size of the FCS focus radius r_{min}, which makes the external calibration by measuring the diffusion of R6G with known D_{R6G} unnecessary (Benda, Benes et al. 2003). It was therefore attempted to fit the data to equation with both r_{min} and D as free parameters, but the scatter in our data was too large to do this consistently. Nevertheless, the average value obtained by this approach was within error similar to the one obtained by external with R6G (241±81 nm and 225±10 nm respectively).

The experimentally determined diffusion coefficients D are plotted versus surface pressure in Fig. 5.3 (right). Error bars represent one standard deviation determined from on average 60 measurements at each surface pressure. The systematic uncertainty originating from the determination of the radius of the observation area at the beam waist r_{min} is not included in the error bars (r_{min} = 225 ± 10 nm). Evidently, D decreases monotonically with increasing surface pressure from 120 ± 16 μm²/s at Π = 1 to 6.5 ± 0.8 μm²/s at Π = 40 (20 °C). The plots of Π vs. D and Π vs. MMA are almost exactly superimposable; Fig. 5.3 (right and inset). With respect to temperature, no significant difference in D is observed for measurements performed at either 20 °C or 22 °C below surface pressures of 35 mN/m. At pressures above 35 mN/m D deviates significantly; D being smaller at 20 °C than at 22°C. In this region the isotherms and especially the compressibilities of the DMPC monolayers at the two different temperatures also show distinct differences: At 20 °C the compressibility is at a minimum at 35 mN/m, and at

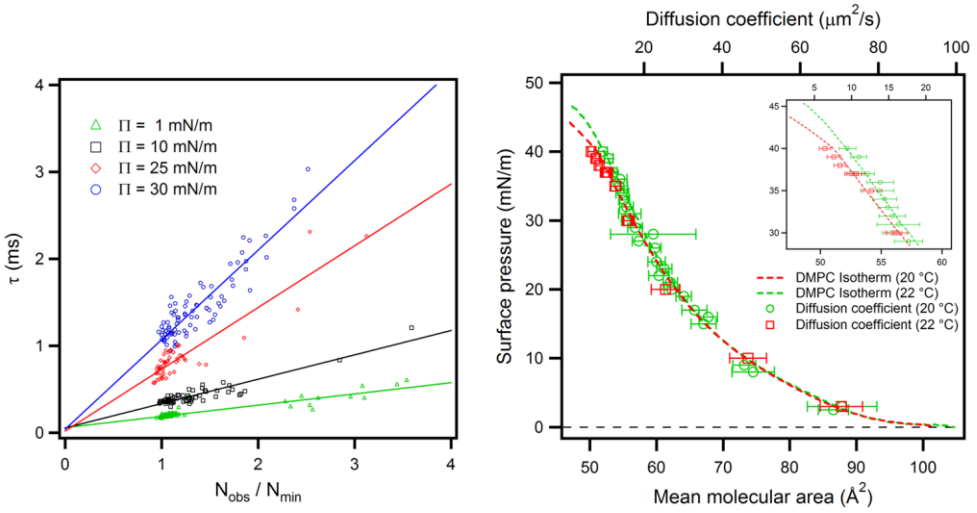

Fig. 5.3 left: Measured diffusion time τ vs N_{obs} / N_{min} for a data set recorded at 22 °C. The slope is given by r_{min}^2 / 4D. All lines pass through the point (0;0±0.1) as predicted by equation. **Right**: Pressure Π vs. diffusion coefficient D (squares) and pressure Π vs. mean molecular area MMA (broken lines) for data sets recorded at 20 °C or 22 °C red and green respectively). The plots of Π vs. MMA and Π vs. D follow the exact same trend. It is noteworthy that the slight temperature induced offset of the Π-A-isotherm is also clearly seen to affect the measured diffusion coefficients. **Right (inset)**: Magnification of range; Π = 28 – 45 mN/m.

22 °C the compressibility is at a minimum at 38 mN/m. These compressibility minima

correspond very well to the pressures at which the kinks in the pressure vs. diffusion coefficient curves are observed.

A plot of D vs. MMA is shown in Fig. 5.4. It shows that D and MMA are linearly dependent in the region between 50 Å² - 90 Å²; with slopes of the least square linear fits being $1.67 \cdot 10^8 \pm 3 \cdot 10^{10}$ s⁻¹ and $1.78 \cdot 10^8 \pm 3 \cdot 10^{10}$ s⁻¹ for 20 °C and 22 °C respectively. These values are similar to reported "jump frequencies" υ_j for lipid molecules in DMPC bilayers at 40 °C; $\upsilon_j = 1.7 \cdot 10^8$ s⁻¹ (Galla, Hartmann et al. 1979). Extrapolation of the straight lines to $D = 0$ yields a value of 47 Å² at both temperatures. In the nomenclature of the free-area model (see below) this corresponds to the critical area a_c; above which lipid translational diffusion becomes possible. A diffusion coefficient corresponding to that of a fluid DMPC bilayer at 25 °C ($4 \cdot 10^{-8}$ cm²/s) would be obtained at 48 Å² according to the extrapolated straight lines.

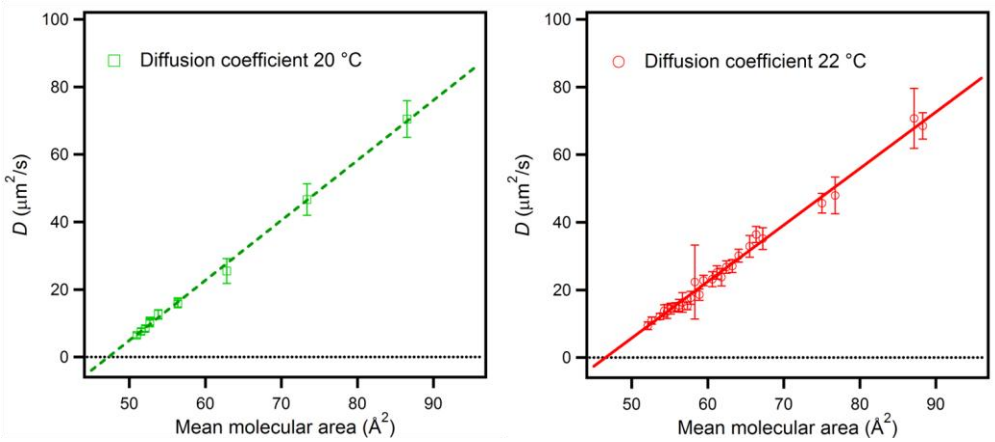

Fig. 5.4 left and right: Plot of the measured diffusion coefficient D vs. the mean molecular area MMA. Both data sets can be fitted perfectly by a straight line (except for one data point at (MMA,D)(95 Å², 120 μm²/s) which is excluded from the plot and fit.

According to the free-area model, a plot of ln D vs. $1/a_f$ is expected to yield a straight line. This is shown in Fig. 5.5 where the data points have been plotted and fit to Eq. (5.4). A key fitting parameter in this fit is the free area, which in the monolayer technique is readily found from the difference between the mean molecular area MMA and the hard core (or van der Waal's) area a_o of the lipid

$$a_f = MMA - a_o \tag{5.11}$$

where the magnitude of a_o for phosphocholines is usually assumed to be ~42-43 Å² (Peters and Beck 1983; Kim and Yu 1992; Marsh 1996; Tanaka, Manning et al. 1999; Ke and Naumann 2001). This value for the hard core area seems reasonable as it is slightly below the average lipid area in a gel phase bilayer (Section 2.2.2) in which translational diffusion is still possible. Hence this average gel lipid area of 48 Å² must include both free area as well as the hard core lipid area. The value $a_o \approx$ 42-43 Å² also fits the minimum value for the mean molecular area MMA where continuously compressed

monolayers are always seen to collapse; for instance the DMPC isotherm at 20 °C shown in Fig. 5.1 (left) could be compressed to a MMA of 44 Å² before monolayer collapse. In the present analysis a_o was set to 42 Å², which provided a quality-of-the-fit value (Pearson's R) of 0.99.

As discussed previously, the free-area model is only expected to be valid in regions "far from" phase transition (Doolittle 1952). DMPC exhibits pronounced pressure induced phase transitions at both low (~0 mN/m) and high pressures (>35mN/m). Thus only the intermediate pressures are expected to fit the model. It is apparent that the experimental data points for Π < 3 mN/m (MMA > 87 Å²) do not fall on a straight line made up of the remaining data points. This suggests that this is the lower limit for the free-area model with respect to a DMPC monolayer. This limit corresponds to an average area per lipid close to two times the hard core area a_o of DMPC (a_o = 42 Å²). Data points below Π = 5 mN/m were therefore omitted from the linear least square fits and analysis below. The data points in the opposite end of the fluid phase appear to lie on the straight line, which is slightly surprising as the free-area model is strictly not valid in this region close to the phase transition. The linear fits were performed with data points weighed according to their standard deviation (error bars in Fig. 5.5) and coefficients from the linear fits are given in Table 3. It is normally assumed that γ, the factor correcting for overlap of free area, is between 0.5 and 1, resulting in a critical area a_c between 24 Å² and 48 Å² at both temperatures. For γ = 0.5 this corresponds well to the value determined by plotting D directly vs. MMA (a_c ~47 Å²). The fit coefficients from the free-area model fits from this and previously published studies are given in Table 3. Also given are single data points for the measured diffusion coefficients at 30 nM/n in the different experiments. Values measured in this study are similar to those reported from FRAP measurement, but one order of magnitude larger than values found by SPT. The origin of the discrepancy between FCS/FRAP and SPT cannot be resolved with the available data.

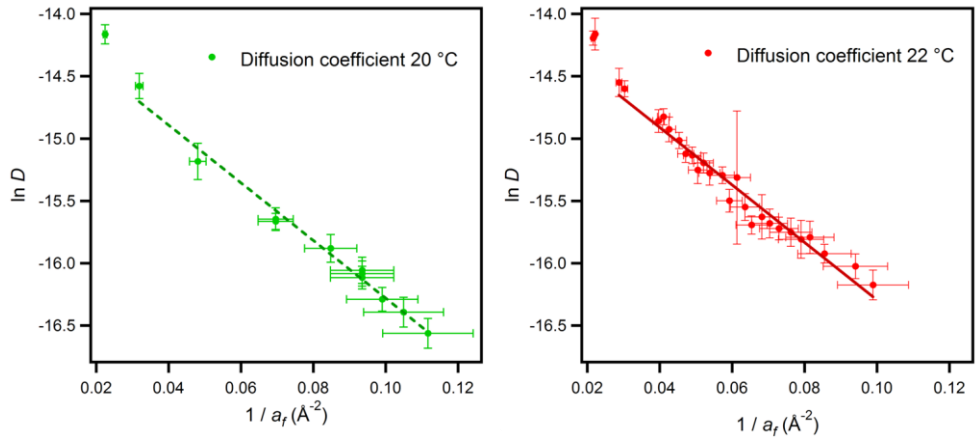

Fig. 5.5 Plots according to the free-area model; Ln D vs the reciprocal of the free area; 1 / a_f (see text). Error bars on the ordinate axis originates from the standard deviation of MMA; which was ~0.5 Å².

Table 3: Values from linear fits of ln D vs $1/a_f$ plots (cf. Eq (5.4): β (= γa_c) and D_{max} (cf. Eq. (5.5) and (5.6)) estimated by extrapolation to $a_f \rightarrow \infty$. D_{max} is the theoretical maximal diffusion coefficient at infinite dilution without phase change. Values from earlier studies on lipid diffusion in monolayers as function of Π and/or MMA are given for comparison. These values were found by re-analysing the original data and in some cases deviate by up to five percent from the original values. The diffusion constants at the approximate monolayer-bilayer equivalent pressure (~30mN/m) are approximately a factor 5 larger than reported diffusion coefficients for fluid bilayers (see text).

Method	**Lipid**	**Temp.** (° C)	β (Å²)	D_{max} (μm²/s)	D**(30 mN/m)** (μm²/s)	**Reference**
FCS	DMPC	20	-23 ± 1.0	86 ± 7	16	-
		22	-23 ± 0.9	88 ± 5	16	
FRAP	DLPC	21 - 22	-25	120	26	(Peters and Beck 1983)
FRAP	DLPC	22 - 23	-31	180	28	(Kim and Yu 1992)
FRAP	DLPC	22 - 24	-23	120	35	(Tanaka, Manning et al. 1999)
SPT	DMPC	24	-8	5	1.5	(Ke and Naumann 2001)

The so-called monolayer-bilayer equivalent pressure is commonly assumed to be in the range 30-35 mN/m (Marsh 1996; Marsh 2006). At this surface pressure diffusion coefficients measured by FRAP and FCS in monolayers are a factor of two lower than diffusion coefficients measured in bilayer systems, which are in the range 3-5 μm²/s irrespective of the method used; FRAP (Wu, Jacobson et al. 1977), FCS (Korlach, Schwille et al. 1999; Hac 2003) or SPT (Schutz, Schindler et al. 1997). That diffusion in monolayers is faster than in bilayers at equivalent lateral pressures seem quite reasonable. For instance, effects such as van der Waal's coupling between the acyl chains of the opposing monolayers and interdigitation (sometimes called dynamic inter-penetration) are absent in monolayers, and this should intuitively result in a more free diffusion in monolayers compared to bilayers. Along these lines one may speculate that the reported SPT values for TRITC-DHPE in DMPC monolayers may have been systematically underestimated as they are lower than diffusion coefficients measured for TRITC-DHPE in POPC bilayers; $D \approx 4.4$ μm²/s (Schutz, Schindler et al. 1997) and DiI(C18) in POPC multilayers; $D \approx 4.9$ μm²/s (Rocha, Hutchison et al. 2008).

The measurements presented herein were all performed at pressures below the phase co-existence region of DMPC. The phase co-existence region is a potentially interesting region in that the compressibility and thus the fluctuations is at a maximum in this region (Heimburg 2007). These fluctuations near the critical temperature ($T_c \approx$ 23-24 °C) are expected to result in highly dynamic behaviour on all length scales from molecules to the entire system (Nielsen, Bjornholm et al. 2000; Nielsen, Bjornholm et al. 2007). At present, it was however not possible to perform FCS measurements in the co-existence region of the DMPC monolayers at neither 20 °C nor 22 °C. The primary reason was that stable pressures could not be maintained for the period of time required to perform a time-dependent z-scan.

5.2.2 Fluorophore partitioning in DPPC at high surface pressures

As described above, the very narrow co-existence region of DMPC near the critical point caused practical problems. Therefore, measurements on DPPC monolayers were initiated to investigate diffusion in the phase co-existence region.

DPPC monolayers exhibit a broad phase co-existence region at room temperature (Isotherms are shown in Section 2.2.1:Fig. 2.5 left) which results in formation of large domains that can be over a 100 times larger than the FCS focus (Fig. 5.6 left). Such domains are readily imaged by wide-field fluorescence microscopy since fluorophores are generally excluded from the crystalline-like structure which makes them appear dark in fluorescence microscopy images.

In order to perform FCS measurements on diffusion inside the domains, different lipid fluorophores were tested (see materials and methods). However, none of the tested lipid fluorophores partitioned in the domains under what is considered to be normal monolayer study conditions (e.g. compression rates ≤ 1 Å^2/lipid/min). Therefore FCS measurements on DPPC were postponed for a future study devoted to this specific "partitioning problem". Instead, single molecule sensitive wide-field microscopy (SMS-WFM) images providing insight into the challenges of fluorescence studies on lipid systems in the LC and S phase are presented in the following.

Fig. 5.6 (left) shows a LC-domain (dark region) in a LE lipid matrix (bright region) formed by slow compression of a DPPC monolayer containing DiI(C18) into the phase co-existence region. The lipid fluorophore concentration was ~10^{-4} mol%. Under these conditions the lipid fluorophore neither partitioned in the LC-domain during domain formation, nor did it penetrate the gel domain after formation. This strongly implies that LC-domains in a fluid lipid matrix should be considered as impermeable ("hard") obstacles for lipid fluorophores in relation to diffusion studies on inhomogeneous systems exhibiting stable LC or gel domains.

Upon further slow compression into the S region (Π > 30 mN/m), at least two populations of lipid fluorophores were seen (Fig. 5.6 right); lipid fluorophores trapped inside the gel domains (arrows in Fig. 5.6 right), and lipid fluorophores accumulated along the reminiscent domain boundaries (grain boundaries). The trapped lipid

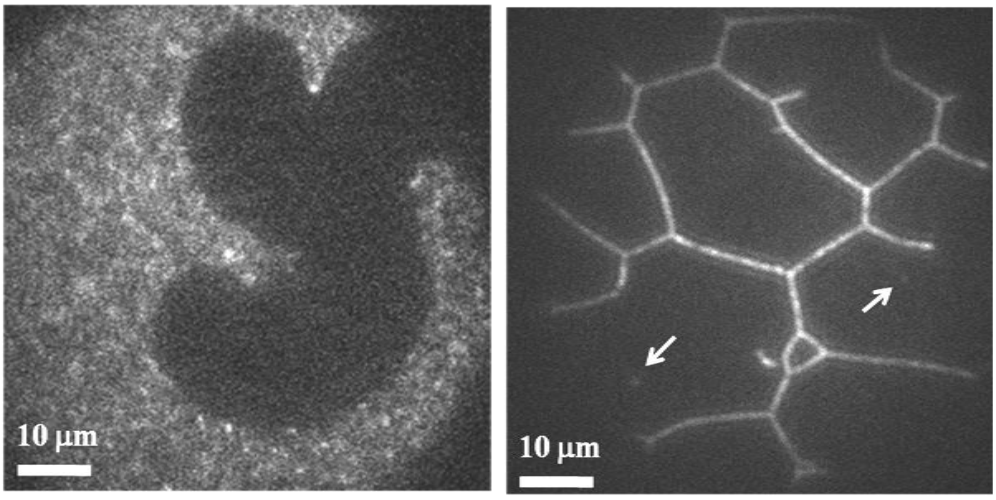

Fig. 5.6 SMS-WFM image of a typical tri-lobed gel lipid domain in the fluid lipid matrix. Lipid fluorophore is DiI(C18). The ratio of DPPC:fluorophore is 1:150,000 (~$7 \cdot 10^{-4}$ mol%) resulting in a few fluorophores per image pixel (px). The domain was formed by slow compression (~1 Å^2/lipid/min). Under these conditions the fluorophores partition exclusively in the fluid regions of the monolayer. Image width and height is 68 μm (256x256 pixels, resolution is 267 nm/px, exposure time 40 ms, irradiance 1 kW/cm^2).

fluorophores remained immobile until they bleached in a single step indicating that they were single fluorophores. As bleaching of the lipid fluorophores along the grain boundaries progressed, single lipid fluorophores in this region became identifiable, showing that the longest surviving lipid fluorophores diffused along the boundaries in a one-dimensional fashion (The term one-dimensional is used loosely in this context, as it strictly implies that the grain boundaries have a width of a single molecule, which is not likely to be the case).

Interestingly, these two populations were not detectable when lipid fluorophore concentrations of 0.1 mol% were used, which is a normal concentration for FRAP studies. Under these conditions a homogenously illuminated monolayer was observed at high surface pressures. Although the grain boundaries are not detectable at this fluorophore concentration, it must be assumed that at least a part of the effect seen at low lipid fluorophore concentrations remain. It is therefore very likely that this effect plays a role in the large range of diffusion coefficient reported in the literature for lipid diffusion in the LC, S or gel phase; 10^{-12} - 10^{-16} cm^2/s (Saxton 1999; Hac, Seeger et al. 2005).

Only when performing very fast monolayer compression and/or relaxation with compression rates > 10 Å^2/lipid/min the lipid fluorophore DiI(C18) was seen to partially penetrate the domains (Fig. 5.7). The resulting domain shapes were highly distorted compared to the domain shapes observed following slow compression (e.g. Fig. 5.7 left). However, even under these conditions DiI(C18) was still only able to penetrate certain areas in the domains. In these areas, only a slight decrease in the absolute amount of fluorophores was observed over time, which indicates that the areas containing fluorophore was in some way connected to the LE phase. A distorted domain is shown in

Fig. 5.7 (left). The area marked by the red square is magnified in Fig. 5.7 (middle and right) where 450 consecutive images are overlaid. Each yellow dot indicates that a fluorophore was observed in at least one of the 450 frames. It is evident that the lipid fluorophores favour specific areas within the domain. This is also clear from Fig. 5.7 (right) where a colour coded histogram image has been constructed. The image construction shows "hot-spots" in dark red; i.e. sites where the lipid fluorophore was seen in more than ten of the 450 images, and areas where no lipid fluorophores where seen during the ~90 second image sequence in dark blue. The image constructions in Fig. 5.7 (middle) and Fig. 5.7 (right) are known as Point Accumulation for Imaging in Nano-scale Topography; PAINT (Sharonov and Hochstrasser 2006), and Histogram-PAINT; H-PAINT (Rocha, Hutchison et al. 2008) respectively.[4] It is evident from the H-PAINT image in Fig. 5.7 (right) that the fluorophores are overrepresented in specific parts of the domain, and along with the domain formation procedure one must contribute the regional miscibility of the lipid fluorophore to extensive defects in the domain structure.

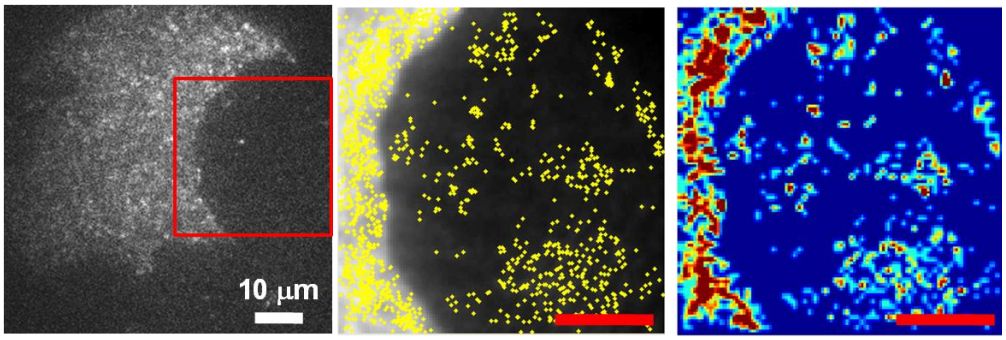

Fig. 5.7 DPPC monolayer containing DiI(C18). Scale bar is 10 μm in all three images. **Left:** Snapshot of a markedly distorted gel DPPC domain formed by fast compression and relaxation. Under these conditions the lipid fluorophores (bright spots) are able to penetrate parts of the domain structure. Total image width and height is 68 μm (256 px) **Middle:** PAINT image of the section marked by a square in left image. Yellow dots denote where a lipid fluorophore was localised during 450 consecutive image frames (~90 seconds). It is clear that the fluorophore is not evenly distributed within the domain. Image width and height is 33 μm (125 px). **Right:** H-PAINT image of the same section as middle image. The H-PAINT image is formed by stacking 450 consecutive image frames. The colour scale refers to the number of times a lipid fluorophores was observed at that specific position in the image; from dark blue corresponding to zero to dark red which is more > 10.

[4] The software used to produce the PAINT and H-PAINT images were developed and kindly supplied by the group of Johan Hofkens in Leuven, Belgium.

5.3 Conclusion

Time-dependent z-scan FCS measurements have been used to measure diffusion coefficients of TRITC-DHPE in a DMPC monolayer at different surface pressures. This method greatly improved the accuracy in determining diffusion coefficients on two-dimensional samples where it can be difficult to define the exact location of the beam waist position relative to the sample.

The measured diffusion coefficients were found to follow the trend of the direct observable surface pressure Π closely (Fig. 5.3, right). The measured diffusion coefficients also fit the free-area model well, and extrapolation of the model fits yielded realistic values of the critical area a_c = 24 - 48 Å^2 and the maximal diffusion coefficient $D \approx 85$ μm^2/s in the fluid phase of a DMPC monolayer. The diffusion coefficient D was also found to be proportional to the mean molecular area MMA (Fig. 5.4) in the LE region. Extrapolation of the fit to experimental data yielded a critical area (the MMA at which D=0) a_c = 47 Å^2 for both investigated temperatures.

The measured diffusion coefficients are slightly below those found by FRAP measurements on DLPC monolayers, and an order of magnitude higher than diffusion coefficients measured in different phospholipid bilayers systems (supported bilayers, stacked bilayers, and GUVs). The difference in diffusion coefficients in relation to lipid bilayers is attributed to a more free diffusion in monolayers. In bilayers, the lipid fluorophore will hindered by van der Waal coupling to an opposing monolayer, as well as subject to interdigitation.

SMS-WFM images of DPPC monolayers containing very low concentrations of lipid fluorophores show that domains in the co-existence region are impermeable to a range of investigated lipid fluorophores, and should be considered as “hard” obstacles in heterogeneous diffusion studies on this and similar systems. At high pressures, where the monolayer is often assumed to be in an all LE or S phase, the fluorophores form at least two distinct populations. One population is made up from immobilised fluorophores in gel regions. Another population consists of fluorophores that form a separate fluid phase along the grain boundaries or defects in the predominantly gel phase monolayer. These phenomena are believed to explain the large spread in reported diffusion coefficients in the literature.

Chapter 6

Activity and diffusion behaviour of PLA_2

In the following section the activity and diffusion behaviour of PLA_2 on a DPPC monolayer is described. The chapter is divided into two major sections. In the first part, results on a system where the monolayer contained a lipid fluorophore are shown. These experiments show the effect that PLA_2 has on the structure (morphology) of a monolayer in the main phase transition region (LE-LC phase co-existence region). In the second part of the chapter, results are reported from experiments where the enzyme was labelled with a fluorophore. This made it possible to directly visualise the diffusion behaviour of single enzymes near the water-monolayer interface. The diffusion coefficient of PLA_2 is determined on a substrate monolayer (DPPC) as well as on a non-substrate monolayer (D-DPPC), showing how on-going hydrolysis affects the diffusion behaviour. Our unique setup also made it possible to change the surface pressure during the single particle studies, and thereby show the difference in adsorption behaviour of PLA_2 to the monolayer as a function of pressure.

6.1 Introduction

Phospholipase A_2 (PLA_2) is a small water-soluble enzyme which catalyses the hydrolysis at the *sn*-2 ester bond of glycerophospholipids to produce a lysophosholipid and a fatty acid (Scheme 1). When the reaction takes place at alkaline pH, the fatty acid immediately dissociates into the corresponding (negatively charged) base and a proton.

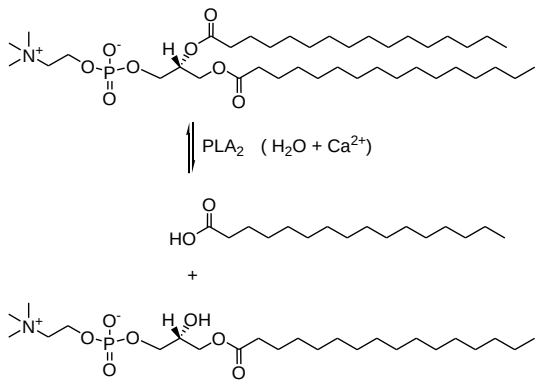

Fig. 6.1 Left: The reaction scheme for PLA_2 catalysed hydrolysis of DPPC. DPPC is cleaved into two smaller fragments; PA (palmitic acid) and lyso-PC (lyso-phoshocholine). The pK_a of PA is ~5, and PA therefore dissociates to anionic palmitate (n-hexadecanoate) and a proton immediately after hydrolysis at the experimental pH value of 8.9.

The enzymatic activity of PLA_2 is stereo-selective and only the (L-) enantiomer is a substrate, whereas the (D-) enantiomer acts as a competitive inhibitor of the enzyme. The activity of PLA_2 is regio-selective in that the catalytic turnover is increased many fold at interfaces between an aqueous medium and an aggregated lipid structure (known as interfacial activation). This activity increase is especially pronounced in the region where two lipid phases co-exist; e.g. near the melting temperature of phospholipid vesicles, or in the LE-LC co-existence region of phospholipid monolayers. In such systems the degree of lipid state fluctuations is also at a maximum (Op den Kamp, de Gier et al. 1974; Romero, Thompson et al. 1987; Mouritsen, Andersen et al. 2006). This dependence on the state of the substrate is sometimes referred to as quality-of-the-interface effects (Verger and De Haas 1976).

A large diversity of phospholipase A_2 sub-types are known to exist. These are all divided into different sub-families depending on their structure and requirement for calcium ions as a co-factor (Six and Dennis 2000). For the last 30 years, the biochemical and biophysical community has primarily investigated two different types of secreted PLA_2: pancreatic PLA_2 (Type IB) and synovial PLA_2 (Type IIA). Both of these can be found in blood stream, and both play important roles in a variety of processes such as; lipid metabolism, apoptosis (cell death), and different cancers (Cupillard, Mulherkar et al. 1999; Mouritsen, Andersen et al. 2006).

Both type IB and type IIA PLA_2 have a molecular weight of 14,000 g/mol, and consist of 126 amino acids and contain 7 disulfilde bridges. Their geometrical shape is similar to a kidney (bean), and the dimensions are ~22 Å x 30 Å x 42 Å (Berg, Gelb et al. 2001). Molecular Dynamics simulations have shown that there is a distance of approximately 1.5 nm from the surface of the membrane plane to the active site of the enzyme, which is

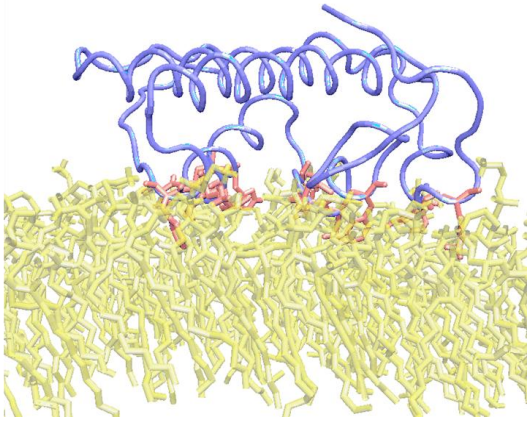

Fig. 6.2 Molecular Dynamics (MD) simulation of pancreatic PLA_2 adsorbed to a lipid interface. The applied model assumes that the enzyme partially penetrates the lipid structure (so-called 'tight binding'). The active site is located in the centre of the enzyme, and the *i-face* (the region in direct contact with the lipid structure) is highlighted in red. From the simulation, it can be estimated that a lipid molecule has to be protruded ~1.5 nm (corresponding to half the length of an extended DPPC molecule) from the plane of the membrane surface to reach the optimal position in the active site. Adapted from (Zhou and Schulten 1996).

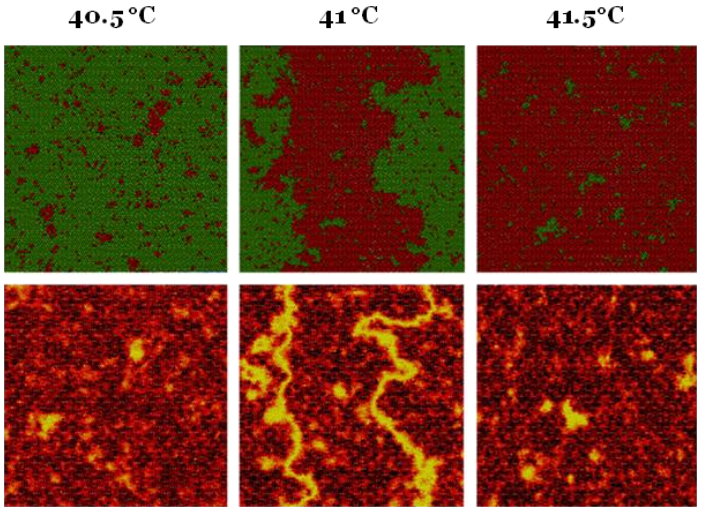

Fig. 6.3 Snapshots from a Monte Carlo simulation of a DPPC matrix at three different temperatures near the melting temperature. **Top**: Lipid distribution (red = solid/LC state, green = fluid/LE state). **Bottom**: The degree of lipid state fluctuations is the highest (coloured in yellow) near the domain boundaries in the main melting transition region (41 °C). In areas consisting mainly of lipids in the same state, there are a minimum of fluctuation (coloured in black). The lipid fluctuations are local fluctuations arising from changes in the ordering of the acyl chains. The activity of PLA_2 is also at a maximum at the main melting temperature of the lipid structure. Simulation courtesy of H. M. Seeger: Based on Differential Scanning Calorimetry (DSC) data on large unilamellar vesicles (LUVs).

located at the top of a cavity in the centre of the molecule (Fig. 6.2). This implies that a lipid molecule has to be protruded significantly from the lipid structure in order to fit into the active site. This protruded lipid configuration is stabilised by hydrophobic amino acid residues exposed along the sides of the active site cavity.

The first direct visualisation of the action of PLA_2 was performed about 20 years ago using wide-field microscopy (WFM) on a lipid monolayer (Grainger, Reichert et al. 1989). Since then, direct visualisation has been performed extensively using e.g. brewster angle microscopy BAM (Li, Chen et al. 2000), atomic force microscopy AFM (Grandbois, Clausen-Schaumann et al. 1998; Nielsen, Risbo et al. 1999), as well as WFM (Jensen and Simonsen 2005; Simonsen, Jensen et al. 2006; Simonsen 2008). Throughout these studies it has been a common observation that the morphologic changes during hydrolysis primarily take place at phase boundaries or at sites of structural defects. It is also common in most of these studies to assume that the change in area of the lipid structure is associated primarily to hydrolytic action. We have also adopted this assumption in this study. The validity of the assumption is corroborated by the fact that the two-dimensional channel-like structures seen in Fig. 6.4 and later in Fig. 6.5, which are formed during hydrolysis, are never seen in the absence of enzyme, and no spontaneous reorganisation of the channels is seen as long as the majority of the initial structure is intact. This indicates that interfering side-effects; such as spontaneous reorganisation due to e.g. line tension and fluidity are negligible in relation to the enzyme induced morphological changes in the lipid structure.

One of the most intriguing and well-studied aspects of PLA_2 is the phenomenon referred to as lag-burst kinetics. This is often observed as a period of apparent low hydrolytic activity (the lag phase) followed by an auto-catalytic burst. Typically, the lag phase (usually defined as the time between enzyme addition and the activity burst) is on the order of 10-30 minutes, but varies depending on a variety of parameters. The lag phase is at a minimum:

- When the experiment is performed in the main transition region of the lipid substrate. In this region the compressibility, the lipid state fluctuations, and the interfacial area are all at their maxima; see also Fig. 6.3 (Honger, Jorgensen et al. 1996; Hoyrup, Callisen et al. 2004).
- When anionic lipids are present at a mole fraction where the substrate and products phase separate. For the DPPC system the amount of free fatty acid and lyso-PC needed to complete annihilate the lag phase is 8%, which is also the ratio at which phase separation occurs (Burack and Biltonen 1994).
- when structural defects (i.e. holes) are present prior to enzyme addition; Since monolayers and vesicles do not exhibit holes that are mechanically stable, this is mainly relevant for immobilised lipid structures on solid supports such as e.g. bilayers on mica (Grandbois, Clausen-Schaumann et al. 1998; Nielsen, Risbo et al. 1999; Jensen and Simonsen 2005)

These experiments strongly suggest the lipid protrusion; i.e. the ease of which lipids can be extracted from the lipid structure, is the most critical factor for enzyme activation (Mouritsen, Andersen et al. 2006). It is also clear that the lipid protrusion must be strongly coupled to the thermodynamic state of the lipid structure.

So far, all published Wide-Field Microscopy (WFM) studies visualising the action of PLA_2 have been ensemble measurements, using enzyme concentrations in the high nano-molar or even micro-molar range. The only studies reporting the behaviour of a single enzyme molecule have been from Atomic Force Microscopy (AFM) measurements. But while AFM is a very powerful technique for resolving structural features down to the angstrom length scale it is limited by its temporal resolution, and also cannot directly reveal the position of the enzyme. Conversely, WFM as used in this study has a suitable temporal resolution and the ability to track single enzyme molecules during lateral diffusion on a lipid structure.

The chapter is divided into two parts. The first part describes experiments where the monolayer was labelled with a lipid fluorophore, while the enzyme was not labelled. These experiments were done at a 5 nM enzyme concentration where enzyme activity could be observed as a change in monolayer morphology. In this part the activity of PLA_2 is visualised and quantified. The second part of the chapter describes experiments where only the enzyme was labelled with an organic fluorophore. In these experiments, the enzyme concentration was below the level where drastic changes in monolayer morphology could be observed. However, the adsorption and diffusion behaviour of single PLA_2 molecules at the water-monolayer interface is described, and the diffusion coefficient of PLA_2 is determined under different conditions.

Unless otherwise specifically stated, these abbreviations are used in the following sections: 'PLA2' will refer to porcine pancreas PLA_2, 'DPPC' will refer to the enzyme substrate (1,2-dipalmitoyl-sn-glycero-3-phosphocholine), and D-DPPC to its enantiomer (2,3- dipalmitoyl-sn-glycero-1-phosphocholine) which is not susceptible to hydrolysis (Van Deenen and De Haas 1963).

6.2 Results & discussion

6.2.1 PLA_2 induced LC-domain degradation

Previous studies which have visualised the action of PLA_2 by BAM, WFM, or AFM have all used Type IIA PLA_2 from different snake or bee venoms (Grainger, Reichert et al. 1989; Dahmen-Levison, Brezesinski et al. 1998; Grandbois, Clausen-Schaumann et al. 1998; Nielsen, Risbo et al. 1999; Jensen and Simonsen 2005; Simonsen, Jensen et al. 2006). In this study, a type IB PLA_2 was used. The choice of porcine pancreas PLA_2 was motivated by the lack of (direct visualisation) studies on the action of this enzyme in the literature, and by the very limited activity of this enzyme outside the phase transition region (Op den Kamp, de Gier et al. 1974) which is ideal for monolayer studies where the enzyme is frequently added prior to monolayer compression.

Since the PLA_2 in this experimental series is different from previous studies, we first performed experiments similar to those of the work by Grainger *et al.* (Grainger, Reichert et al. 1989; Grainger, Reichert et al. 1990) to assess to what extent the action of these two enzymes is comparable. This involved compressing a monolayer of DPPC (with 0.1 mol% lipid fluorophore embedded) into the phase co-existence region on a subphase consisting of Tris buffer (10 mM, pH 8.9, 150 mM NaCl, 5 mM $CaCl_2$) and enzyme. Except for the type of enzyme used, the only other difference is that we used ~30 times lower nominal concentration of enzyme than in the experiments of Grainger *et al.*; 5 nM vs. 130 nM respectively. A complete experimental protocol is given in the Appendix (A.5).

The PLA_2 induced degradation of LC-domains is shown in Fig. 6.4. The bright regions in the image series indicate the LE phase enriched in the lipid fluorophore (TRITC-DHPE). The dark regions indicate the LC-domains (referred to as 'domains' in the following) from which the lipid fluorophore is excluded. The enzyme was not marked with a fluorophore in this experiment. Fig. 6.4A shows the appearance of the LC-domains immediately after the compression of the monolayer was stopped and the lipid monolayer was brought into the phase transition region. This point in time is defined as time zero ($t \equiv 0$). The domain shapes at $t = 0$ and the partial isotherm (not shown) were similar to those seen in Chapter 4 and those reported in the literature (Maloney and Grainger 1993; Klopfer and Vanderlick 1996; McConlogue and Vanderlick 1997).

The first visible effect of PLA_2 adsorption and/or hydrolytic action is the relaxing of the bean shaped domains into circular round shapes (Fig. 6.4B). This re-arrangement

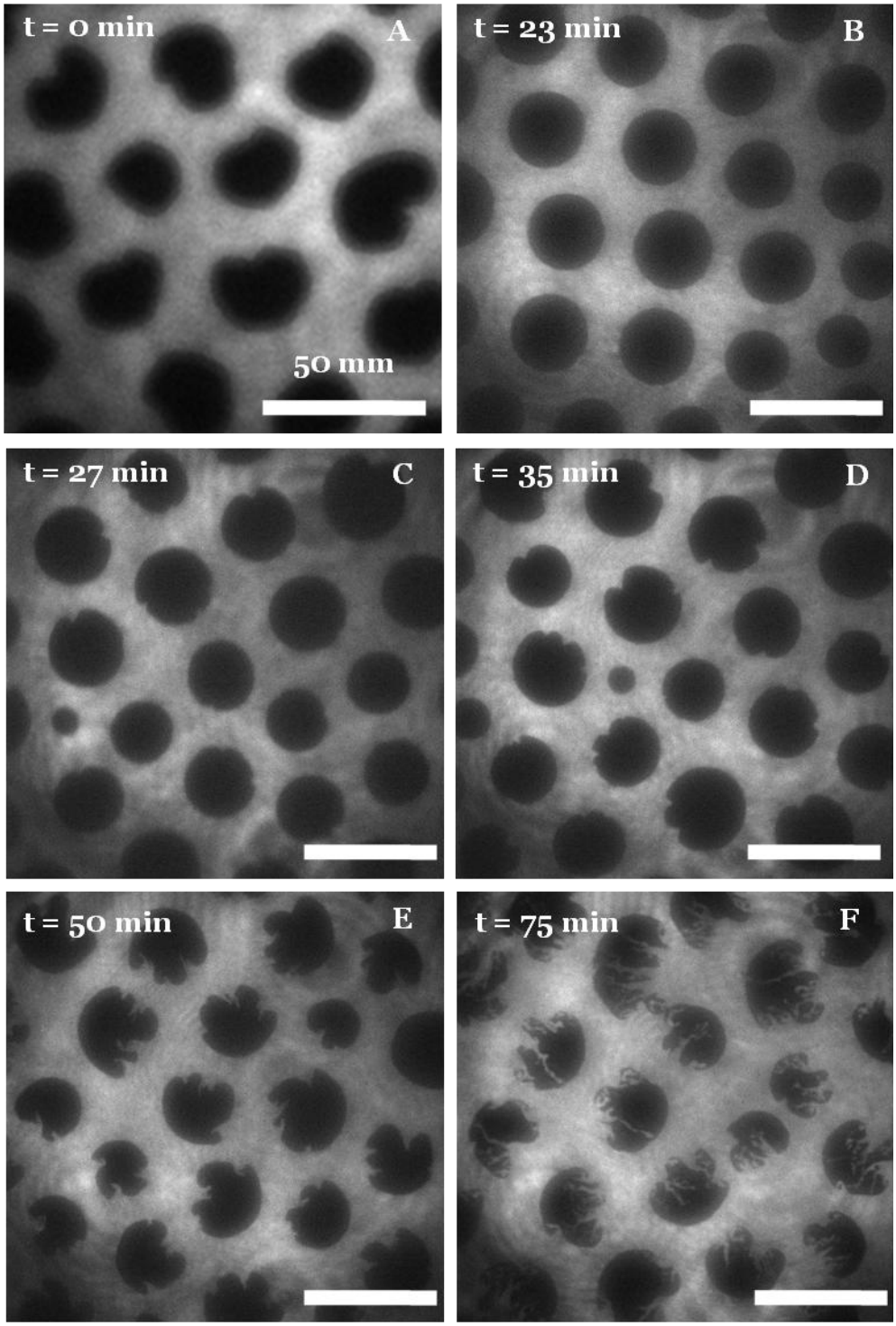

Fig. 6.4 Selection of images at different time points during the PLA_2 induced degradation of LC-domains in a DPPC monolayer with 0.1 mol% lipid fluorophore embedded. The bright regions are the LE region, and dark regions the LC-domains. The degradation is caused by (non-fluorophore marked) PLA_2 present in the subphase at a bulk concentration of 5 nM. (**A**) Typical domain shape at MMA 65 $Å^2$ immediately after compression stop. (**B**) 34 minutes after compression stop one can see the first few indentations in the LC-domains. (**C-H**) The domains are degraded via narrow channels which penetrate the domain in a linear (directed) fashion. Subphase: Tris, pH 8.9, 150 mM NaCl, 5 mM $CaCl_2$. All scale bars are 50 μm. The domains are not exactly the same from frame to frame due to surface flow (drift) of the monolayer. Images were taken with a 40x magnification (NA 0.6) microscope objective.

occurs much faster for monolayers with enzyme in the subphase than for those without. In our experiments, with 5 nM PLA_2 in the subphase, it typically took less than half an hour for the domains to relax, whereas it has been reported to take 12 hours in the absence of enzyme (Klopfer and Vanderlick 1996). This phenomenon can be explained by the fact that PLA_2 adsorption disrupts the lipid packing in the domains: It has previously been shown by X-ray diffraction studies that the D-DPPC molecules in tightly packed monolayers are tilted 30° relative to the lateral axis (Brezesinski, Dietrich et al. 1995), and that this angle changes to 8° when enzyme is injected under the monolayer. This corroborates well with a model where the enzyme preferentially adsorbs to the domain boundaries (Dahmen-Levison, Brezesinski et al. 1998) and thereby disorders the molecular structure of LC-domains near the boundary by changing the tilt angle. The enzyme probably also screens the electrostatic forces from the lipid head groups. This causes line tension to become the dominant force and drives the domains to develop into the observed circular shapes.

The first visible effect of PLA_2 adsorption and/or hydrolytic action is the relaxing of the bean shaped domains into circular round shapes (Fig. 6.4B). This re-arrangement occurs much faster for monolayers with enzyme in the subphase than for those without. In our experiments, with 5 nM PLA_2 in the subphase, it typically took less than half an hour for the domains to relax, whereas it has been reported to take 12 hours in the absence of enzyme (Klopfer and Vanderlick 1996). This phenomenon can be explained by the fact that PLA_2 adsorption disrupts the lipid packing in the domains: It has previously been shown by X-ray diffraction studies that the D-DPPC molecules in tightly packed monolayers are tilted 30° relative to the lateral axis (Brezesinski, Dietrich et al. 1995), and that this angle changes to 8° when enzyme is injected under the monolayer. This corroborates well with a model where the enzyme preferentially adsorbs to the domain boundaries (Dahmen-Levison, Brezesinski et al. 1998) and thereby disorders the molecular structure of LC-domains near the boundary by changing the tilt angle. The enzyme probably also screens the electrostatic forces from the lipid head groups. This causes line tension to become the dominant force and drives the domains to develop into the observed circular shapes.

During the same time period, corresponding to the period between images in Fig. 6.4A and B, the surface pressure increased monotonically at constant area due to a combination of enzyme adsorption and penetration into the monolayer as well as initial hydrolysis (isotherm for similar experiment shown in Fig. 6.6).

The subsequent images (Fig. 6.4C-F) show the hydrolysis induced LC-domain degradation progress. At first, small indentations are seen on the LC-domains (Fig. 6.4C-D) after a lag time of 27 minutes. Then, in Fig. 6.4E-F, the indentations develop into two-dimensional structures which are often referred to as channels (Grainger, Reichert et al. 1989; Grandbois, Clausen-Schaumann et al. 1998; Nielsen, Risbo et al. 1999). Two characteristic features are especially noteworthy. (1) The domains are only degraded from one of the two halves of the circular domains, leaving the opposing half remarkably inert to hydrolysis. (2) The indentations which evolve into channels seem to be directed, and in many cases follow a straight line over large distances on the molecular level. This indicates that the physical organisation of the lipid molecules in

the domain is important for hydrolytic action. One may speculate that this is due to the lipids only being accessible to the enzyme from one side due to the tilted lipid organisation described above.

The reaction typically proceeded for one hour until the majority of the domains had been degraded (Fig. 6.4F). After this the monolayer morphology did not change. It is interesting to observe how two of the partially hydrolysed domains are attracted to each other in the final image (Fig. 6.4F). This is in strong contrast to the behaviour of the initial behaviour of the domains where they were arranged on a hexagonal super-lattice to maximise the inter-domain distance. This joining of LC-domains was always seen at the end of the hydrolysis process, and always in the configuration seen in Fig. 6.4F; where the hydrolysed regions of the LC-domains joined together. It varied between experiments how many of the hydrolysed LC-domains that joined.

The backsides of the domains were never seen to join. Notice also how most of the domains are arranged with the hydrolysed side facing the back side of another domain; a feature that can only be explained by electrostatic effects. It is also noteworthy that the time point of the initial attack (Fig. 6.4C) and subsequent domain degradation appear to be a highly concerted action; i.e. the time at which degradation begins, evolves, and ends is virtually the same for all domains in the field of view. This clearly favours the view that enzyme activation is closely related to the macroscopic (thermodynamic) state of the lipid interface.

Based on these observations we chose to perform a new series of experiments where only a single domain was observed. For these experiments a custom-made monolayer trough was constructed (Section 3.1). This trough made it possible to work with very low monolayer subphases (~100 μm) and thereby to employ high numerical aperture (NA) microscope objectives which have working distances on this order of length scale. High NA objectives provide far better quantum collection efficiency and optical resolution (Section 2.3), which makes it possible to relatively accurate outline and measure the area of the domains and the length of the domain boundary (the length of the boundary is referred to as 'perimeter' in the following). It is important that the domains structures are optically well-resolved when measuring the perimeter as this is known to be dependent on the optical resolution (Mandelbrot 1967). As the optical resolution does not allow for perfect resolution, we will inadvertently get a lower estimate for the perimeter in the following measurements.

The protocol was similar to the one in the previous experiments; the enzyme was added in a nominal concentration of 5 nM to the buffered subphase before the lipid was spread on the aqueous surface. Monolayer compression was initiated immediately at a compression rate of 5 Å^2/lipid/min. Compression was done from a mean molecular area MMA of 110 Å2 and until the Liquid-Expanded - Liquid-Condensed (LE-LC) phase co-existence region was reached (Π = 8 mN/m, MMA = 65 Å^2). A detailed experimental protocol is included in the Appendix (A.5).

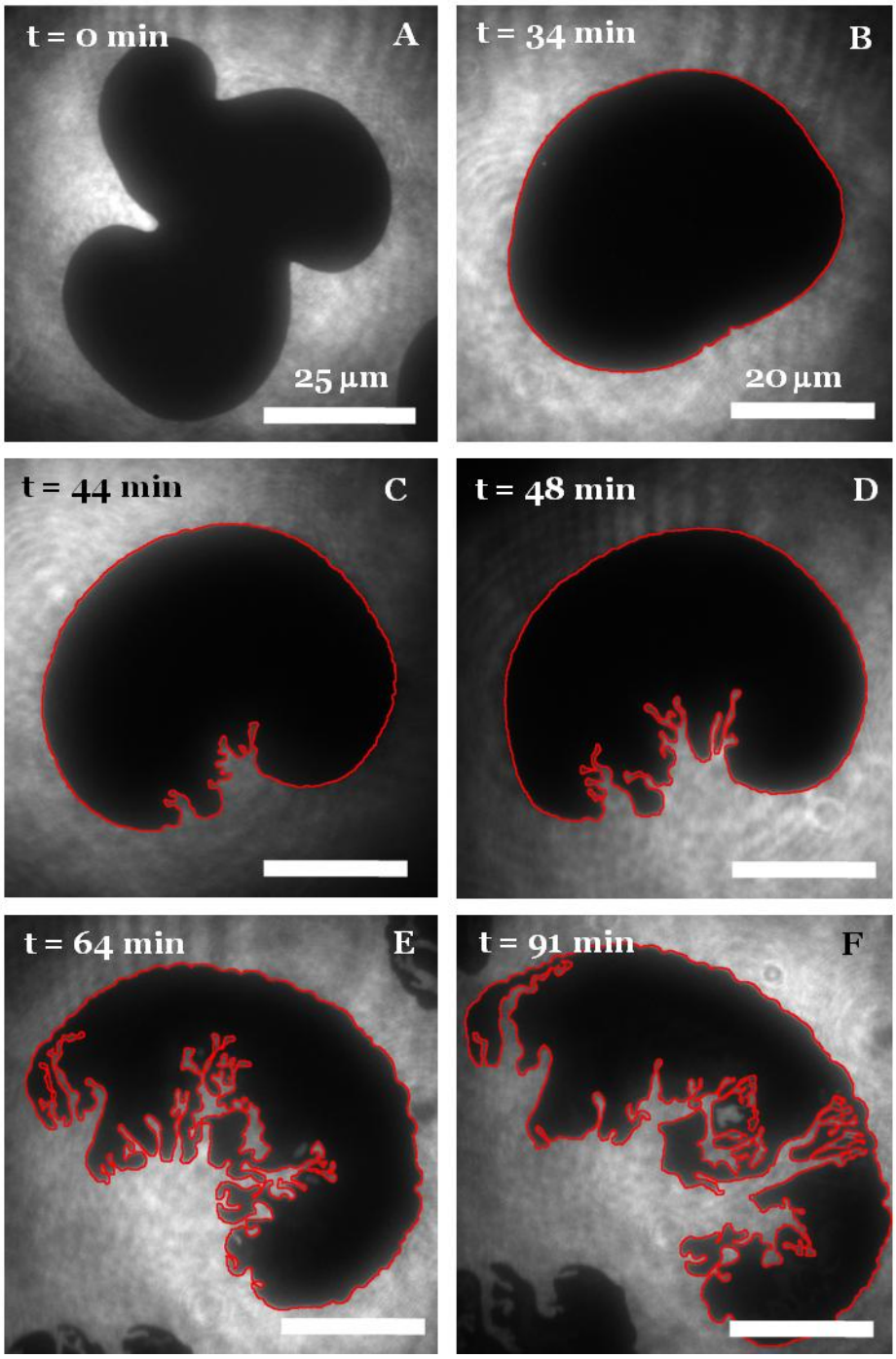

Fig. 6.5 Time evolution of a LC-domain during PLA_2 catalysed hydrolysis. The domain shapes are outlined in red (image post-processing). The images in between image B (t = 34 min) and image E (t = 64 min) were analysed with respect to quantifying the change in area and the change in perimeter versus time. Note that the domain in image A is not the exact same as the domain followed in image B-F, as a slight drift in the monolayer did not make it possible to keep the same domain in focus during the entire time sequence of images. All scale bars in images B-F are 20 μm^2. The DPPC monolayer contained a fluorescent lipid analog (TRITC-DHPE). The enzyme was not marked with a fluorophore.

Fig. 6.5 shows the time-evolution of a LC-domain (dark region) surrounded by LE phase (bright region) during hydrolysis catalysed by PLA_2. The degradation pattern closely resembles the one seen in the previous experiments with multiple domains in the field of view as well the pattern seen in solid supported lipid structures during the hydrolytic action of PLA_2 (Grandbois, Clausen-Schaumann et al. 1998; Nielsen, Risbo et al. 1999). In addition, the lag times are similar in the two experiments; ~27 and ~34 minutes for the experiment visualising multiple domains and the experiment visualising a single domain respectively. This is slightly longer than the lag times for apparently defect free solid supported bilayers (Nielsen, Risbo et al. 1999; Jensen and Simonsen 2005).

The dynamics of such a system can be quantified by different approaches. It is not practical to evaluate the kinetics based on the pressure vs. time (Π-*t*) curve (shown in Fig. 6.6) since the surface pressure depends on multiple interrelated processes; e.g. adsorption and accumulation of enzyme at the water-lipid interface, and formation of reaction products which may partially dissolve in the subphase (Ivanova, Ivanova et al. 1996).

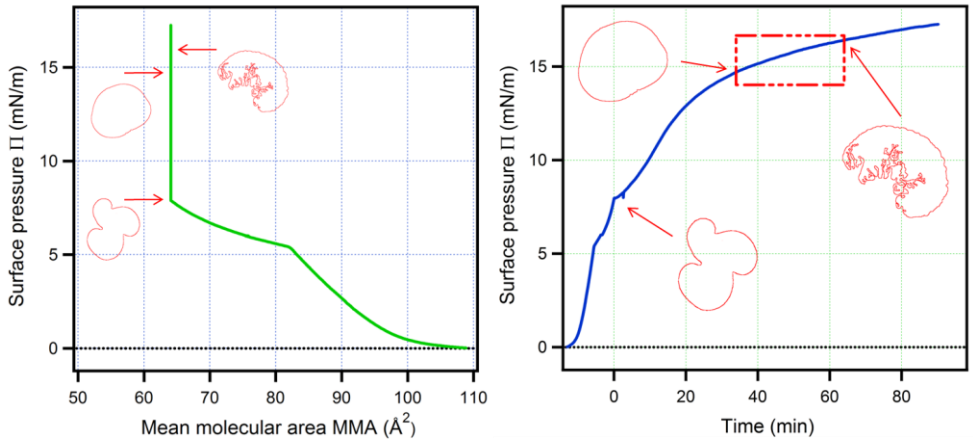

Fig. 6.6 left: Pressure-area isotherm from the experiment shown in Fig. 6.5. Compression was started at a MMA 110 Å², and the onset of the LE-to-LC phase transition region is seen at MMA 82-83 Å². Compression was stopped at a target MMA of 65 Å² corresponding to a surface pressure of 8 mN/m. The monolayer was kept a constant area during the enzyme adsorption and hydrolysis process. The domain shapes at corresponding pressures during the hydrolysis process are shown for reference. **Right**: Pressure-time plot: Compression was started at t= -13 min, the phase co-existence region was reached after 7 minutes (t = -6 min), and compression was stopped after 13 minutes when larger tri-lobed domains had been created (t ≡ 0). The part of the isotherm bounded by the red box corresponds to time period in which images were analysed; at t = 34 minutes the first indentation was seen. After t = 64 minutes the domain had been extensively degraded. Domain outlines correspond to Fig. 6.5A, B, and E.

It is also not straight-forward to evaluate the change in total domain area with respect to time, as this also appears to depend on the surface pressure which increases during the hydrolysis process. This is shown in Fig. 6.6, where it can be seen that the total area of the domains increased from 1470 μm², when the first domain indentation

was observed, to 1510 μm² approximately 10 minutes later (t = 44 min). After this time point, the degradation becomes more rapid and a decrease in the total area is seen. The highest rate of change in domain area with respect to time (dA/dt) is found at 52 minutes and is -5 μm²/min. Assuming that the average lipid area is 50 Å² results in a maximum turnover rate of $1 \cdot 10^7$ lipids/min at a nominal PLA_2 concentration of 5 nM. However, such a number holds little information, as it does not contain any information on the concentration of enzyme at the surface or the "concentration" of substrate which plays an important role in interfacial enzyme kinetics; see e.g. (Honger, Jorgensen et al. 1996; Nielsen, Risbo et al. 1999; Jensen and Simonsen 2005).

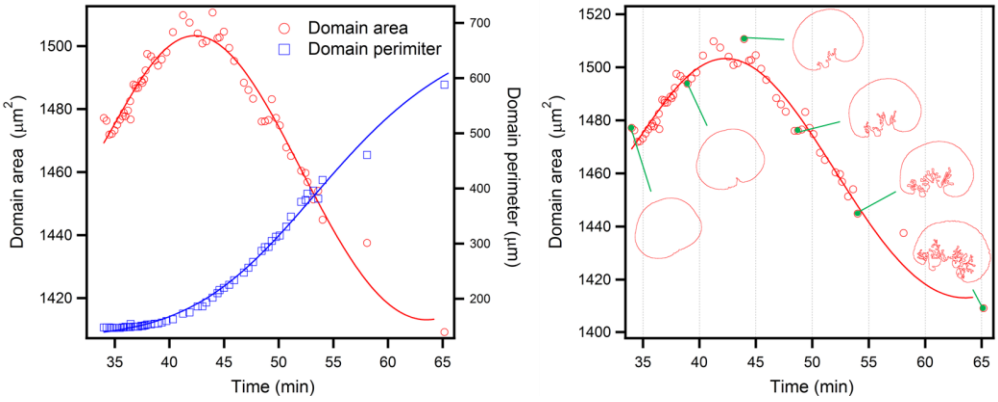

Fig. 6.7 Left: Time evolution of the LC-domain area A and perimeter P. Data points are given as red circles ◦ and blue squares ▫ and the smoothed full lines serve only as a guide for the eye. Both curves have the highest numerical value for the derivative at t = 52 min (not shown). **Right:** Same curve as in the left panel (A vs t). Outline of domain shapes are given for six random images of the in total 60 analysed images in the time interval 34 – 64 minutes. Counter-intuitively the area of the domain increases when the initial degradation becomes visible in the shape of indentations and channels.

The most appropriate method of analysis is to quantify the change in domain area of a specific region and relate it to the perimeter within the same region. In this method of analysis it is presumed that the domain boundary within the region of interest is available for enzyme action, and thus represents the substrate concentration. This method of analysis has become the standard method for quantifying enzyme activity from image analysis (Nielsen, Risbo et al. 1999; Balashev, Gudmand et al. 2003; Jensen and Simonsen 2005). These analyses frequently show that the rate of degradation of the lipid structure increases when the perimeter increases. This is also valid for the domain in Fig. 6.5. The area A and perimeter P versus time t is shown in Fig. 6.8(left) which illustrate the classical lag-burst activity: Initially the lag-phase show very limited activity (channel growth), but as the indentation into the domain structure grows, the activity increases in the burst phase. Due to product inhibition and possible lack of suitable substrate the activity decreases again toward the end of the degradation process.

The model which attributes activity to the available substrate implies a relation of the type

$$\frac{dA}{dt} \propto \alpha \cdot P \tag{6.1}$$

where α is the slope of the lines in Fig. 6.8 (right), and P is the perimeter of the LC-domain. This relation is also found to hold for the current analysis. However, it is only valid for the initial phase where the perimeter within the channel is short Fig. 6.8 (right). It is not surprising that Eq. (6.1) only holds for low values of P, since the formation of channel structures demonstrates that part of the domain boundary inside the channel is not available for enzyme attack.

The average α-values for the lines are 0.4 μm/min. From this number, a lower estimate for the enzyme activity can be made by assuming that the enzyme molecules are constantly active and sit closely packed all along the domain boundary. If the distance between the enzymes is on average 5 nm, then there are ~200 PLA_2 molecules per μm of domain boundary. We also need to estimate the number of lipid molecules per μm^2, which is $2 \cdot 10^6$ if the mean molecular area is 50 $Å^2$. Using these numbers, the rate of hydrolysis per enzyme can be estimated to ~70 lipid molecules/enzyme/second (the numbers used for this estimate is given in Apeendix C.1). The same calculation, but for the highest observed rate at t = 52 min (dA/dt = 0.5 μm^2/s, P = 350 μm) yields ~3

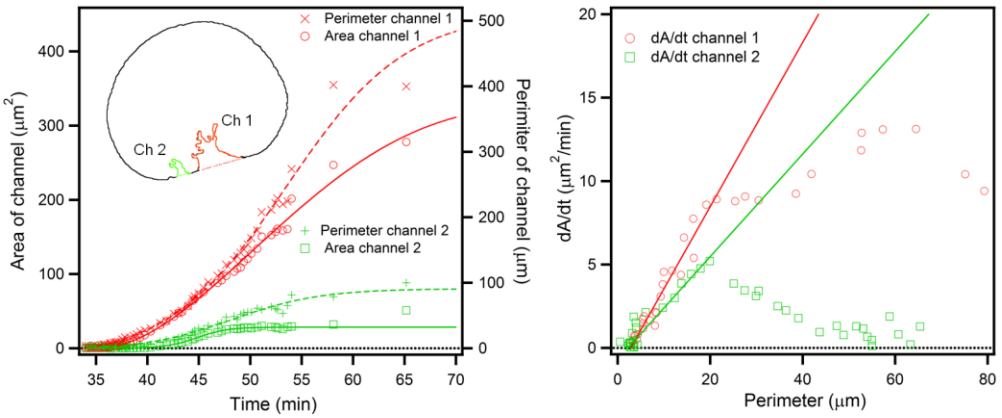

Fig. 6.8 left: Time evolution of the area and perimeter within the two main channels penetrating the domain in Fig. 6.5**. Inset:** The domain outline from Fig. 6.5C illustrating the location of the two channels penetrating the domain structure. **Right:** The rate of area increase dA/dt for the two channels (local domain degradation) versus perimeter (~ available substrate). Initially, there is a linear relation indicating that the entire perimeter is available for enzyme attack. As the perimeter grows the relation is lost. This indicates that not all the perimeter is available for enzyme attack.

lipid molecules/enzyme/second. This number is significantly lower than the number calculated from the initial rate, because a significant fraction of the perimeter after 52 minutes clearly did not act as a site for degradation.

Although a comparison between different systems and different methods of analysis is complicated, the different studies in general arrive at comparable numbers:

- The lowest value for single enzyme turnovers (~4 s^{-1}) was found in a previously published AFM study on an initially all gel state DPPC membrane without structural defects degraded by snake venom PLA_2 (Nielsen, Risbo et al. 1999).
- In the present study an almost 20 times larger value was found (~70 s^{-1}). This value is for a monolayer system in the LE-LC phase co-existence region.
- A slightly higher value has been found in AFM studies on bee venom PLA_2 on gel state DPPC bilayers; 88 s^{-1}. In this study the turnover was estimated from the assumption that the individual channels were created by a single enzyme (Grandbois, Clausen-Schaumann et al. 1998).
- A recent AFM study on fluid state POPC multilayers estimate a turnover of 200 - 250 s^{-1} (Simonsen, Jensen et al. 2006).
- The highest reported turnover (~500 s^{-1}) is related to the turnover of lipids in lipid vesicles in solution at the phase transition temperature (Jain and Berg 1989; Berg, Rogers et al. 1997).

With these numbers in mind we will leave this type of experiments where the lipid was labelled and enzymatic activity was quantified. Instead, we will focus on the single molecule experiments where the enzyme was labelled and the diffusion behaviour of the enzyme was investigated.

6.2.2 *Single PLA_2 molecules at the lipid monolayer*

It is a fundamental challenge in biophysics to describe the diffusion behaviour of enzymes at water-lipid interfaces; e.g. cell membranes. This is especially true in the case where the catalytic activity is enhanced at the interface, as it is the case for many lipases. For enzymes which are 'interfacially activated' the diffusion behaviour of the enzyme at the monolayer is likely to be heterogeneous, and to depend on the state and lateral organisation of the monolayer. Such heterogeneous diffusion behaviour is difficult, if at all practically possible, to quantify using ensemble fluorescence techniques such FRAP or FCS. However, single particle tracking, using wide-field fluorescence microscopy has the ability to visualise and track thousands of individual particle trajectories from a single experiment and thereby resolve the expected multiple diffusion coefficients of the enzyme with a reasonable statistical certainty.

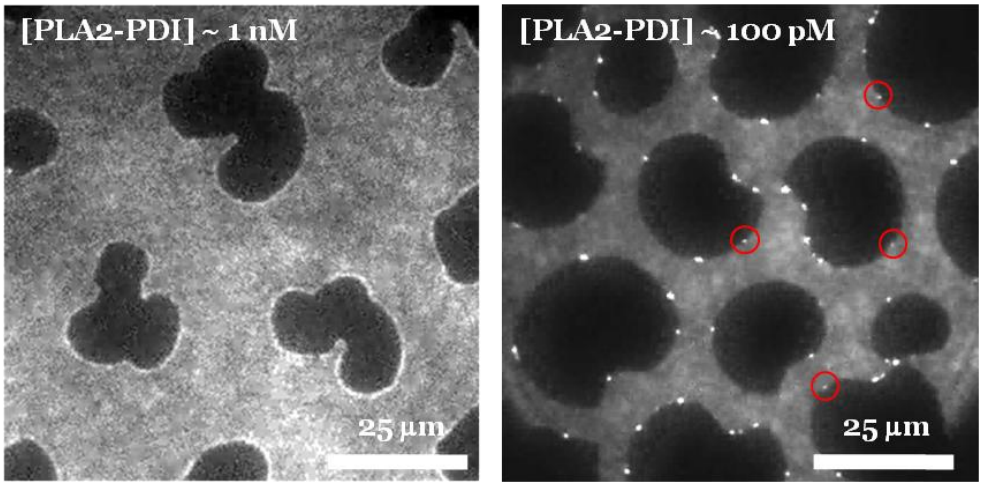

Fig 6.9 Wide-field fluorescence microscopy images of two different DPPC monolayers in the LE-LC phase co-existence region (MMA ~ 65 Å²). The observed fluorescence signal is solely from the enzyme; PLA_2 labelled with the fluorophore PDI (PLA_2-PDI). The enzyme was injected under the monolayer after domain formation. **Left**: 10-15 minutes after addition of PLA_2-PDI to the subphase, the fluorescence signal from the enzyme completely cover the LE phase, while virtually no enzyme can be observed within the LC-domains. After an additional 5-10 minutes the enzyme begins to observably accumulate at the LC-domain boundary giving rise to high signal intensity in this region. **Right**: In a similar experiment, at slightly lower surface concentration of PLA_2-PDI, the enzyme is seen to accumulate in small clusters along the LC-domain boundaries. Judged from the intensity and bleaching behaviour, some of the small spots (four random ones have been highlighted) may well be single enzymes, but this is not conclusive since there are too many enzymes on the monolayer to identify individual molecules.

One of the frequently discussed mechanistic traits of lateral enzyme diffusion and activation is whether the enzyme works in a 'hopping mode' or a 'scooting mode' (Jain and Berg 1989). But also other traits such as the tendency for the enzyme to accumulate at domain boundaries within the interface have been investigated and discussed (Dahmen-Levison, Brezesinski et al. 1998). The accumulation phenomenon is visualised in Fig 6.9 at two different enzyme concentrations; 1 nM and 100 pM. In both images the

fluorescence signal comes exclusively from the labelled enzyme. At the highest enzyme concentration a nearly uniform accumulation of enzyme surrounding the LC-domain is seen. At a concentration of enzyme ~10 times lower, the enzymes are distributed in clusters along the LC-domain boundary. Some of the spots closely resemble the intensity signal from single enzymes (see below), but the optical resolution does not allow for this to be stated conclusively.

In order to be able to identify and track the movement of individual enzyme molecules, it is necessary that the enzymes are well separated laterally on the monolayer. In practice it is not easy to determine the optimal nominal concentration of enzyme that allows this and since enzyme tends to accumulate at the interface this concentration will also vary in time. Therefore a different approach was used when adding enzyme to the subphase in the following experiments relative to the experiments described in the preceding section where domain degradation was visualised.

In these SPT experiments, the DPPC monolayer (with no lipid fluorophore embedded) was compressed to a pre-set target pressure. Then the fluorescently labelled enzyme was carefully injected into the subphase approximately two centimetres away from the optical axis (i.e. the area directly above the microscope objective). This created an enzyme concentration gradient which allowed a range of surface concentrations of enzyme to be investigated and visualised within a single experiment by focussing the microscope on different areas of the monolayer. This method made it possible, within the same monolayer, to visualise regions of very high enzyme concentrations where the LC-domains were clearly degraded, regions of intermediate enzyme concentration (e.g. Fig. 6.10), and regions of low enzyme concentration where the individual enzyme molecules could be distinguished from each other. Due to this enzyme concentration gradient the nominal (bulk) concentration of enzyme in a particular region of the monolayer was not known exactly. The enzyme concentrations given in the text below were therefore estimated by determining the surface concentration at the region of interest and then assuming that 1% of the enzyme was located at the surface at any given time. A complete protocol is given in the Appendix.

6.2.3 PLA_2 at a DPPC product-domain

Hydrolysis of DPPC at the sn-2 ester bond creates PA (palmitic acid) and lyso-PC (1-Palmitoyl-2-Hydroxy-sn-Glycero-3-Phosphocholine, Fig. 6.1). At alkaline pH, PA readily deprotonates and produces the negatively charged base palmitate (for simplicity also abbreviated PA) and a proton. PA is known to phase separate and form so-called product domains during hydrolysis of DPPC. This is seen both in monolayers (Maloney and Grainger 1993) and in lipid vesicles (Burack and Biltonen 1994). These anionic lipid domains are considered to be important for the activity of PLA_2. The product domains are primarily believed to act as an enzyme recruitment factor in that they attract and bind the net positively charged enzyme.

Fig. 6.10(left) shows the appearance of a DPPC monolayer compressed into the LE-LC phase co-existence region prior to enzyme injection. Only the enzyme is labelled, and it is apparent that it is heterogeneously distributed across the monolayer.

The image reveals three distinct regions. The first type of regions is the dark regions outlined in red. Based on their shape and size, these dark regions can be identified as LC-domains. The fact that these regions appear almost completely dark indicates that the enzyme does not adsorb to this region. This is in agreement with the assumption that the enzyme has to partially penetrate the lipid structure to bind to the monolayer (cf. the tight binding mechanism in Fig. 6.2). This is not possible in the closely packed LC-domain regions. The second region is the LE region in which a weak but homogenous signal is seen. The enzymes in this region are seen to move rapidly. However, the enzyme molecules are spaced too closely to resolve the individual trajectories and thereby to determine the diffusion coefficient by SPT. The third region is believed to be a product domain which neighbours upon the LC-domain. The fluorescence signal from the enzyme molecules in this region is much more localised than the enzyme signal in the LE-phase. This indicates that the enzyme diffuses slower at the product domain than at the LE region of monolayer, which is not surprising as the *i-face* of PLA_2 is positively charged, and the product domain negatively charged.

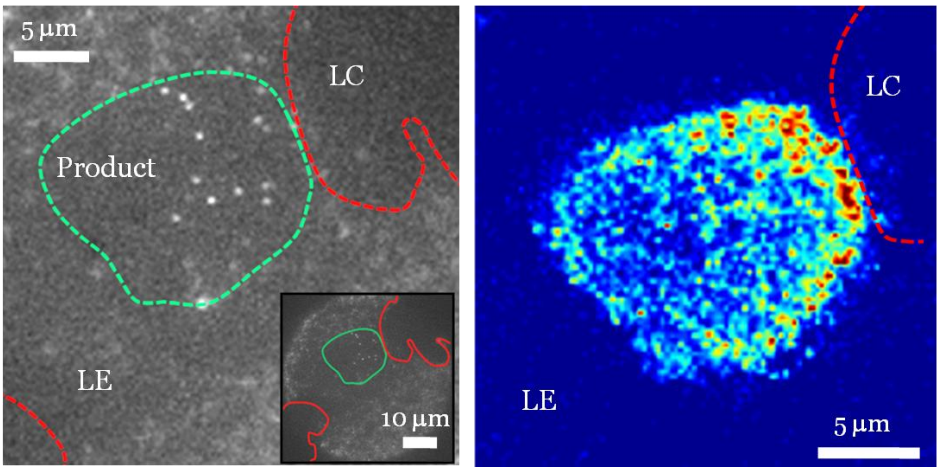

Fig. 6.10 Unprocessed wide-field fluorescence microscopy images of a DPPC monolayer with labelled PLA_2 actively hydrolysing the monolayer lipid from the LC-domain boundary. The observed fluorescence signal is solely from the labelled enzyme; PLA_2 labelled with the fluorophore PDI (PLA_2-PDI). The enzyme was injected under the monolayer after domain formation at Π=12 mN/m and MMA ~60 Å^2. Estimated enzyme concentration is 50 pM. **Left:** Typical image from the image series consisting of 1500 images in total. Three different regions are observed. The first is the completely dark regions (outlined in red) which are LC-domains under which the enzyme practically does not adsorb. The second region is the bright region (not outlined) which indicate the LE-phase. Under this phase the enzyme adsorbs and performs lateral diffusion giving rise to the homogenous appearance. The last region (outlined in green) is a region where the enzyme is observed to diffuse slower, and thus the signal is more localised. This region is a so-called product domain consisting mainly of deprotonised palmitic acid (PA). The negative charges of the hydrolysis products PA cause the enzyme to diffuse slowly relative to diffusion under the LE-phase. The shape of this product domain was determined from the image construct in the right panel of this figure. **Inset:** The entire field of view showing two LC-domains, the product domain, and the LE region.**Right:** H-PAINT image construct using 1000 consecutive images (see text). The mage construct show hot-spots near the product-domain - LC-domain interface. In general, it appears that the enzyme is more frequently located near the edges of the product-domain. The colour scale goes from: Dark red ~ 20 frames contain an enzyme at this position. Dark blue is zero.

The observation that the product domain is formed prior to the characteristic LC-domain indentations and channels agrees well with a simple model: Initial hydrolysis takes place at the domain boundary. At a given mole fraction, the product phase separates into a negatively charged product domain. This domain is attracted to the LC-domain which has a macroscopic electric dipole moment. The product domain acts as a platform for recruitment of enzyme, and also constitutes an increased amount of phase boundary from which the lipid is easily protruded and hydrolysed (See also Fig. 6.14).

This model is supported by the image construct in Fig. 6.10 (right). This is a so-called H-PAINT image (Rocha, Hutchison et al. 2008). It is constructed from an image series of 1000 images, where every enzyme in all images has been localised by fitting to a 2D-Gaussian distribution (positional accuracy < 200 nm). The final image is constructed by accumulating all the determined enzyme positions into a single image; called a H-PAINT image. The colour scale in the H-PAINT image goes from red (referred to as a hotspot) representing that 20 of the image frames contained an enzyme at this position, and to dark blue which represents few or zero enzyme occurrences in that position during the complete image series. The H-PAINT image construct reveals that the enzyme has a preference for the domain boundary between the LC-domain and product domain. In general, the so-called hot-spots (frequently occupied localisations) appear near the edges of the product domain, and are very pronounced at the boundary between the domain and the product domain. These findings are in good agreement with the model of PLA_2 activation at interfaces and domain boundaries hypothesised above.

6.2.4 Single molecule diffusion on DPPC versus D-DPPC

In the following section the diffusion behaviour of PLA_2 on a DPPC monolayer and on a D-DPPC monolayer is compared. Unlike DPPC, D-DPPC is not a substrate for PLA_2, and these two systems therefore make it possible to compare how ongoing hydrolysis influences the diffusion behaviour of PLA_2. H-PAINT images of the two systems are shown in Fig. 6.11. The only fluorescence signal comes from the labelled PLA_2 bound to the monolayer.

These experiments were done at low enzyme concentration (~1 picomolar) as it is necessary for the particles to be well separated in order to perform SPT studies. At this 'single enzyme' concentration it is not expected to observe large morphological changes. A quick back-of-the-envelope calculation shows that a single fully active enzyme would require at least 30 min to degrade the lipid molecules corresponding to the area of a single image pixel.

The image constructs in Fig. 6.11 show a fundamental difference between enzyme distribution at a DPPC monolayer and a D-DPPC monolayer. For a D-DPPC monolayer only a single hot-spot is observed (which is regarded as an artefact; see image legend), while for a DPPC monolayer several hot-spots are seen as a result of hydrolytic action and consequently presence of anionic PA. Previous studies have shown that PLA_2 at high nominal concentration accumulates at both DPPC and D-DPPC boundaries

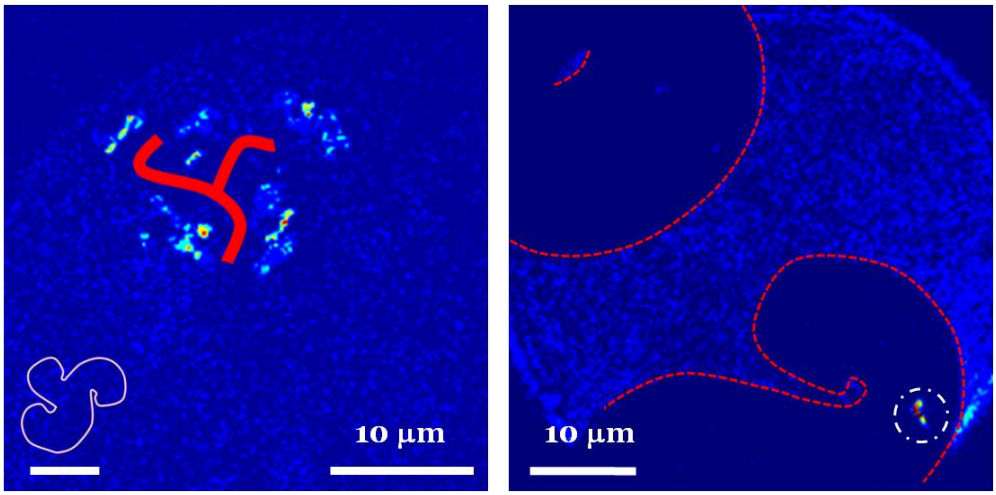

Fig. 6.11 H-PAINT images of a DPPC (left) and a D-DPPC (right) monolayer. Only the enzyme injected into the subphase after LC-domain formation was labelled with a fluorophore. Notice that the handedness of the D-DPPC LC-domain shape is opposite to the previously shown DPPC LC-domains (the LC-domain lobes turn in the counter-clockwise direction). Estimated PLA_2-PDI concentration was ~1 pM. **Left:** H-PAINT image constructed from 250 consecutive images. The multiple hot-spots (sites frequently occupied by the enzyme) indicate regions in which the enzyme is overrepresented. These regions most likely contain hydrolysis products. Due to the low number of fluorophores present on the monolayer, the outline of the LC-domain cannot be conclusively determined. However, based on the location of the hotspots, and assuming a typical LC-domain structure, a potential framework is proposed and shown in bold red. **Left inset:** Template structure for the framework. Inset adapted from (McConlogue and Vanderlick 1997). Scale bars are both 10 µm. **Right:** H-PAINT image from 1000 consecutive images. In contrast to the left image of DPPC, no hot-spots are seen on the edges of the D-DPPC LC-domains or in the LE region. The hot-spot seen inside the LC-domain (highlighted white circle) is considered an artefact of enzymes getting trapped inside a structural defect within the LC-domain.

(Dahmen-Levison, Brezesinski et al. 1998). In the present study it was found that this effect was concentration dependent for D-DPPC, but not for DPPC. DPPC always showed hot-spots at various positions along the domain boundary, whereas for D-DPPC hot-spots and accumulation of enzyme at the LC-domain boundary was only seen at enzyme concentrations above the nanomolar range.

The image constructs also show a fundamental similarity. The enzyme was seen to adsorb equally well to DPPC and D-DPPC monolayers. This indicates that the affinity for PLA_2 towards the two monolayers types is the same. This is in agreement with previous findings from experiments on lipid vesicles (Bonsen, Vandeene.Ll et al. 1972). It also shows that hydrolytic action is not a prerequisite for enzyme adsorption.

6.2.5 SPT – Determination of diffusion coefficients

To determine the effects of hydrolytic action on the diffusion coefficient of PLA_2 at the lipid interface, a SPT analysis was performed on image sequences of up to 1500 images. Typically 500-1000 individual particle trajectories were included in each data

set. The analysis shows that there is a significant difference in the rate of the translational diffusion coefficient D on the two different monolayer systems. Typical particle trajectories obtained from SPT are shown in Fig. 6.12. Due to the excellent photo-stability of the PDI fluorophore; > 5 seconds in an aqueous environment (Margineanu, Hofkens et al. 2004), the PLA_2-PDI conjugate could be tracked for relatively long times compared to typical SPT experiments using organic fluorophores. In general, the survival time of the fluorophore by far exceeded the residence time of the enzymes at the surface making bleaching effects negligible. Only fluorophores which were sometimes found completely immobilised at the domain boundaries were subject to bleaching.

For PLA_2 diffusion on the large product domain shown in Fig. 6.10 the SPT analysis yielded two characteristic diffusion coefficients; D = 0.16 $\mu m^2/s$ and 0.03 $\mu m^2/s$. Of all the 900 analysed trajectories, 87% of them contained only steps with the fast diffusion coefficient, while 13% contained both fast and slow diffusion steps. No trajectories were found to be exclusively slow. These trajectory heterogeneities show that most of the enzymes diffuse fast during their entire residence time on the monolayer, and only a small percentage is transiently slowed down. This type of information is the strong point of SPT and the cumulative distribution function analysis (Schutz, Schindler et al. 1997). However, at present it remains speculative to attribute e.g. enzyme activity/in-activity to the two different diffusion coefficients.

For diffusion on the DPPC monolayer shown in Fig. 6.11 (left), three characteristic diffusion coefficients were determined. A fast diffusing component (D = 2.7 $\mu m^2/s$) and two slow components; one of them from virtually immobilised particles (D = 0.03 $\mu m^2/s$), and another for confined (anomalous) diffusion (0.3 μm^2; α = 0.2). These different diffusion coefficients are considered to be related to the increased lateral heterogeneity in the monolayer created during hydrolytic action.

Interestingly, for the D-DPPC monolayer only a fast component (D = 4.6 $\mu m^2/s$) was found for the particles in the LE-region (The particles confined inside the structural defect were immobile; D = 0). The diffusion coefficient for free diffusion is a factor of 2 larger than the diffusion coefficient found for PLA_2 on the DPPC monolayer. This may be interpreted as a result of the PLA_2 binding mechanism being similar for the two monolayers, but that diffusion is slightly hindered by the presence of opposite charges at the DPPC monolayer from the hydrolysis products.

The measured diffusion coefficients are not expected to be directly related to the catalytic turnover of lipid molecules (i.e. diffusion limited catalytic activity) as a diffusion coefficient of 0.01 $\mu m^2/s$ would yield turnover rates of several thousand lipids per second (up to 10^5 s^{-1}). This is considerably higher than any measured turnover rate in the literature (Berg 1985; Jain and Berg 1989; Berg, Gelb et al. 2001).

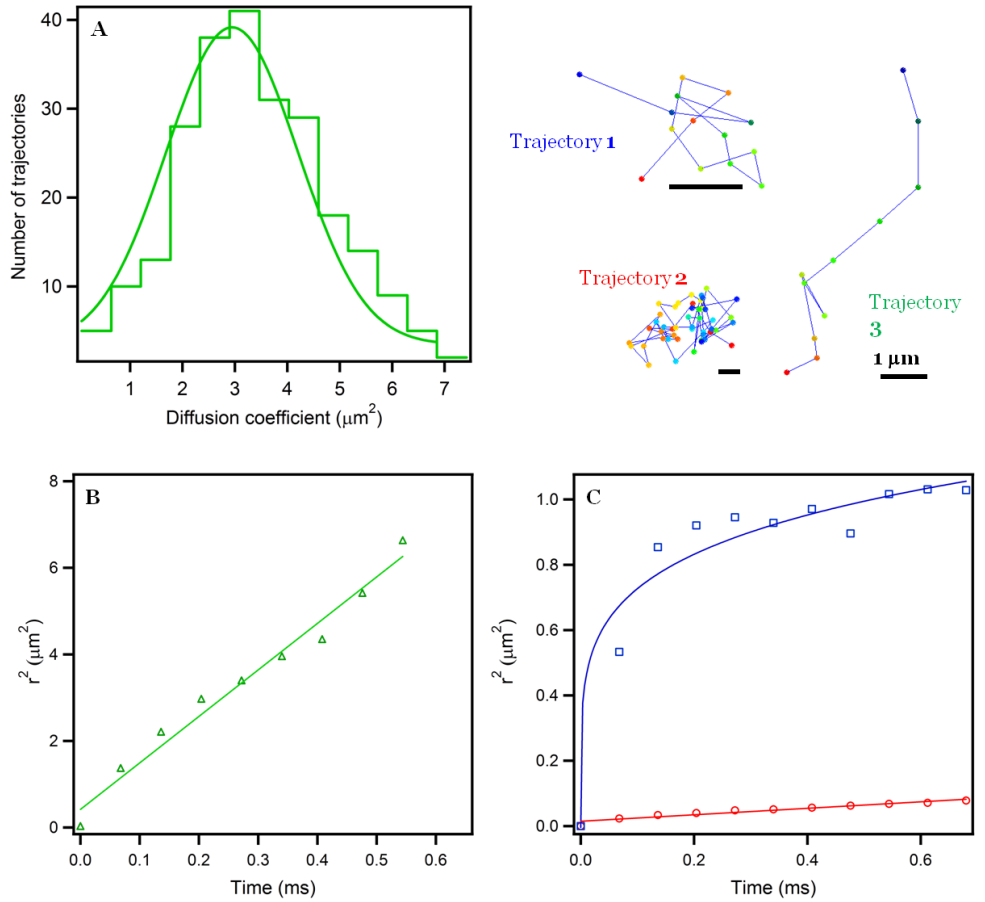

Fig. 6.12 Data from the single particle tracking analysis experiment shown in Fig. 6.11 (left). Three different trajectories are shown in the upper right corner; confined diffusion (trajectory 1, blue curve in panel C), virtually immobilised particle (trajectory 2, red curve in panel C), and normal diffusion (trajectory 3, green curve in panel C).**A:** Histogram of diffusion coefficients from trajectories exhibiting normal/free diffusion. Evaluated according to the method proposed of Saxton (Saxton 1997). The Gaussian fit yields a value for the average diffusion coefficient D = 2.9±0.1 μm²/s. **B:** Same data set as in A. Evaluated according to the cumulative distribution function (Schutz, Schindler et al. 1997). The slope of the fit results in an average diffusion coefficient D = 2.7±0.2 μm²/s. **C:** Mean square displacement versus time for immobilised and confined diffusion. Diffusion coefficients were determined from the cumulative distribution function.

6.2.6 *Effect of surface pressure on adsorption and diffusion*

It has been shown in previous studies that the surface pressure of a monolayer has a strong influence on the activity of PLA_2 (Ivanova, Ivanova et al. 1996; Brezesinski and Mohwald 2003; Zhai, Li et al. 2003). A series of experiments was therefore performed in the surface pressure range from 20 mN/m to 25 mN/m. This pressure range was chosen for two main reasons. First of all, it was directly observed from the fluorescence images that a striking change in the enzyme mobility occurred in this range of surface pressures. Secondly, one should expect a change in PLA_2 activity in this region, based on the fact that the second order phase transition from Liquid-Condensed (LC) to Solid (S) lies in this pressure range (Albrecht, Gruler et al. 1978).

As mentioned, a clear change in the appearance of the fluorescence microscopy images was apparent when compressing the monolayer from 20 mN/m to 22.5 and 25 mN/m. At the lowest pressure, the enzyme was seen to diffuse rapidly and unhindered on the time scale of the camera exposure (40 ms) creating diffuse spots in the recorded fluorescence images (Fig. 6.13, inset). At the higher pressures the spots were more localised, indicating a significant change in the mobility of the enzyme. A representative spot-size recorded at Π = 25 mN/m is given in Fig. 6.13 (inset). This spot size is on the order of the resolution limit, indicating that the enzyme is virtually immobile during the 40 ms camera exposure time. In addition to the spots being narrower at the higher pressures, they also appeared in the same regions of the monolayer during the entire image sequence. The regions where the enzyme frequently shows up are most likely grain boundaries or other structural defects in the monolayer.

The drastic change in diffusion behaviour is likely to be linked to structural changes in the monolayer, which in turn may be linked to the thermodynamic state of the monolayer. This change could well be the LC-S phase transition, which is a second order phase transition primarily attributed to ordering of the lipids on a hexagonal lattice with low compressibility (Möhwald 1995). This is in good agreement with the current model where enzyme activity peaks when the monolayer compressibility is at a maximum where both enzyme penetration and lipid protrusion are favoured. As it is shown here, when the monolayer is compressed into the S-phase, the enzyme can no longer penetrate the monolayer, except near structural defects. This leads to practically zero enzyme activity of DPPC monolayers in the S-phase (Solid) which has previously been reported (Brezesinski and Mohwald 2003).

As mentioned, it is readily seen from the width of the spots in the fluorescence images (Fig. 6.13, inset) that the mobility (i.e. translational diffusion coefficient D) of the enzyme at the monolayer changes as a function of pressure. These diffusion coefficients for PLA_2 at all three different surface pressures were quantified using single particle tracking (SPT). This resulted in two different values for the fast (normal/free) diffusion coefficient; D = 2.2 $\mu m^2/s$ for Π = 20 mN/m and D = 0.1 $\mu m^2/s$ for Π = 22.5 and 25 mN/m. Slower components were also found from immobilised/confined diffusion; for instance, a slow diffusion coefficient of D = 0.1 $\mu m^2/s$ was also found from the particle tracking analysis from the experiment at Π = 20 mN/m.

In addition to the SPT analysis, it was briefly attempted to determine the diffusion coefficient directly from the width of the spots. A brief note on this can be found in the Appendix (C.3).

Finally, the residence time of the enzymes at the monolayer can be found by analysing the time-length of the individual trajectories. The residence times also favour the view that the S-phase is not favourable for enzymatic action and that the enzyme does not bind well at the higher pressures. The residence time t_{res} at Π = 22.5 and 25 mN/m (t_{res} ~ 24 and 34 ms respectively) are a factor two lower than the residence time in the LC-phase at Π = 20mN/m (t_{res} ~ 63 ms). The normalised number of trajectories

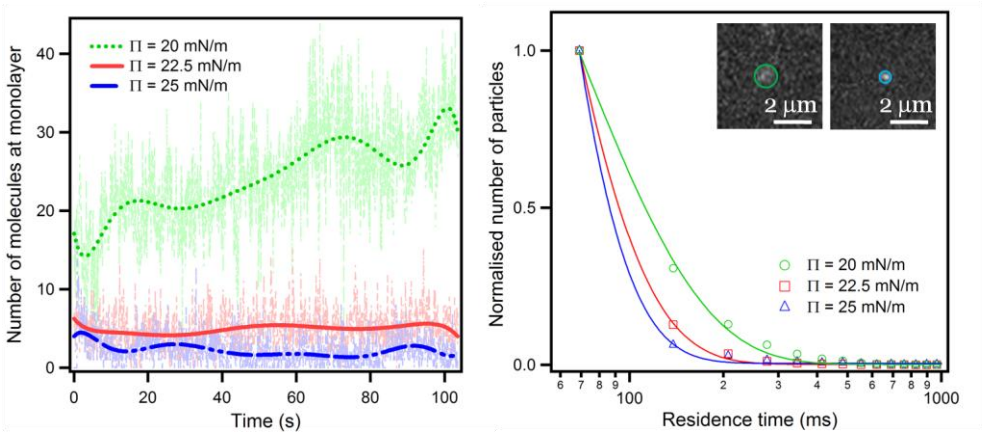

Fig. 6.13 The absolute number of of enzymes at the monolayer in 1500 consecutive image frames (left) and the residence time of the enzymes at the monolayer at three different pressures (right). **Left:** Absolute number of enzymes present in each frame during the 1500 image sequence. The total area analysed for all three pressures were 1000 μm². The data presented here is from a single monolayer experiment where the enzyme was injected under the monolayer at P = 25 mN/m, and then relaxed to 22.5 mN/m and 20 mN/m. the exact same trend in number of enzymes versus pressure was seen when the monolayer was recompressed from 20 mN/m to 25 mN/m. Dots are data points and lines a smoothed fit to the data points. The average over all frames is 24 enz/frame, 5 enz/frame, and 2 enz/frame for the three pressures in order of increasing pressure. **Right:** Normalised number of enzymes at the monolayer versus residence time (i.e. the time-length of the particle trajectories) in a semi-logarithmic plot. Fit to the data points are single exponential decays. The half-time from the fits are: 63 ms, 34 ms, and 24 ms in order of increasing pressure. **Right inset:** Typical enzymes fluorescence signal at P = 20 mN/m (left, green) and at 25 mN/m (right, blue). At Π = 25 the spot size from the fluorescence signal is resolution limited (R ~ 0.5 μm). At Π = 20 mN/m, the enzyme is mobile during time of the camera exposure 40 ms) and creates a delocalised, less intense, spot with a diameter > 1 μm.

versus residence time is shown in Fig. 6.13 (right).

6.3 Conclusion

The activity of porcine pancreas PLA_2 as a catalyst of DPPC hydrolysis was investigated using the monolayer technique combined with a high resolution wide-field fluorescence microscope. The porcine pancreas PLA_2 was seen to degrade domains in a similar fashion as that seen for snake venom PLA_2 in earlier studies (Grainger, Reichert et al. 1989; Grainger, Reichert et al. 1990). The time-evolution of domain degradation induced by PLA_2 activity was analysed and found to be proportional to the perimeter in the early stages of the degradation process. At longer times the rate of domains degradation decreased, most likely due to inhibition from hydrolysis products. The highest turnover rate of lipid molecules in a domain was estimated to be 60 'lipid molecules'/second/'enzyme molecule'.

Single Particle Tracking (SPT) was performed by labelling the enzyme with the highly photo-stable organic fluorophore 'PDI'. The SPT studies showed that PLA_2 accumulates at the edge of DPPC domains and lead to formation of product domains in the LE-region of the monolayer prior to formation of the channels into the domain. This confirms the well-described phenomenon that the activity of PLA_2 is highest at domain boundaries. But for the first time, it is shown that hydrolysis takes place prior to formation of channels into the domains.

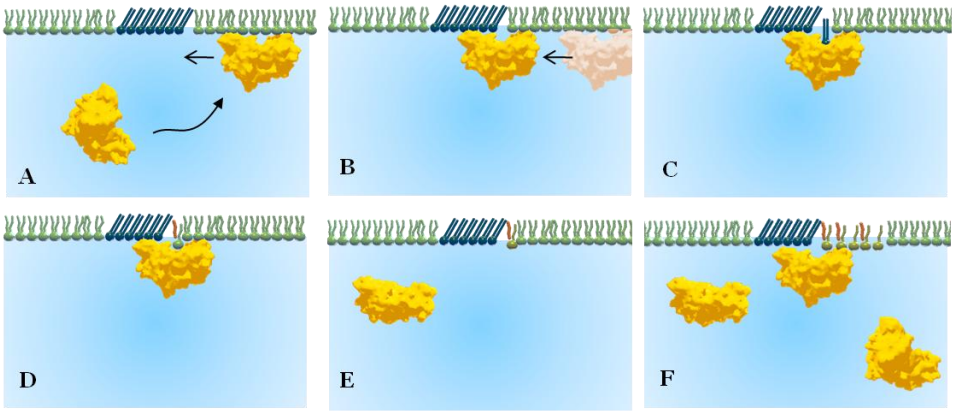

Fig. 6.14 The model of PLA_2 action at water-lipid interfaces. **A-B:** the enzyme molecule adsorbs to the lipid interface and partially penetrates the lipid structure. **C:** If the enzyme diffuses to a packing defect or a LC- domain boundary then protrusion of lipids are much more likely to occur. **D-E:** The protruded lipid (with tilt angle ~8 °) is hydrolysed, creating a lyso-PC molecule and a negatively charged palmitate molecule. **F:** Besides disrupting the structure of the monolayer, which further increases the probability of lipid protrusion, the negative charged product molecules will tend to attract and bind enzyme molecules more strongly. These two effects lead to the auto-catalytic process known as lag burst kinetics.

The tendency for PLA_2 to accumulate at the domain boundaries (in the concentration regime of single enzymes) was higher on DPPC monolayers than on D-DPPC monolayers, where it was virtually zero. This observation fits well into the accepted model for lipid adsorption and activation where it is believed that accumulation is

enhanced by the presence of charged hydrolyses products (Op den Kamp, de Gier et al. 1974; Jain and Berg 1989; Berg, Rogers et al. 1997; Mouritsen, Andersen et al. 2006).

The decreased mobility of PLA_2 on the product domain was attributed to an increased binding strength relative to that of the LE region of the monolayer. However the assumed increased binding did not result in a markedly higher average residence time (130 ms and 120 ms for the product domain and the LE region respectively). Only on the D-DPPC monolayer, which is completely void of product molecules, a significantly different average residence time of the enzyme was found (t_{res} = 70 ms).

On the DPPC monolayers, three distinct modes of diffusion were observed, fast diffusion, confined diffusion, and immobilised diffusion. On an equivalent monolayer of D-DPPC, only fast diffusion was seen. The slow diffusion modes are attributed to diffusion on a partly charged monolayer. The residence time was also found to be higher on the DPPC monolayer than the D-DPPC monolayer, which is also explained by the presence of anionic lipid species in the DPPC monolayer that bind the positively charged *i-face* of the enzyme more strongly than the pure zwitterionic monolayer. In general, the residence time of single enzymes on the monolayers were found to be quite short - on the order of 100 ms. This is in good agreement with the findings that PLA_2 acts in a 'hopping mode' on zwitterionic substrates. However the average residence time on the product domain was found to be shorter than expected since an enzyme diffusing on an anionic lipid structure is expected diffuse in scooting mode(Jain and Berg 1989). The low residence time may be attributed to several competing processes; e.g. the product molecules may dissolve in the subphase and potentially draw the enzyme into solution with it. It should be noted that it is unlikely that the residence time is simply the survival time of the fluorophore, as immobilised fluorophores could be observed for up to 10 seconds under similar conditions.

Table 4 Summary of experimentally determined diffusion coefficients and residence times for porcine pancreas PLA_2 on DPPC and D-DPPC monolayers.

	Diffusion coefficient μm²/s	**Residence time (ms)**	**Note**
DPPC (LE region)	2.7	120	PLA_2 accumulates near the LC-domain boundary
Product domain (lyso-PC / PA)	0.16	130	No tendency for PLA_2 to accumulate
D-DPPC (LE region)	4.6	70	PLA_2 accumulates near the LC-domain/product domain boundary

Finally the effect of pressure was investigated. Above the crystalline phase transition pressure (~20 mN/m) the enzyme only showed confined or immobilised diffusion. At 20 mN/m two modes of diffusion was observed; a fast diffusion, and a slow diffusion. The fast diffusion was slightly faster than diffusion on a monolayer in the phase

transition region. Also in this experiment the enzyme residence time was highest on the monolayer which was susceptible to hydrolysis (Π = 20 mN/m). The number of enzymes on the monolayer was also found to be significantly higher for the monolayer where fast diffusion was observed. This was explained by fewer suitable adsorption sites on the monolayers at high pressures (Π = 22.5 mN/m and 25 mN/m) as well the presence of attractive anionic lipids in the low pressure monolayer (Π =20 mN/m).

These results corroborate the established substrate theories for enzymatic activation at interfaces, as well as providing new knowledge of the behaviour of enzymes on the single molecule level. It has been shown that product domains are formed prior to creation of indentations on the LC-domains, that lateral diffusion of PAL2 is much slower on the product domains that on a DPPC monolayer, which in turn is a factor of two slower than diffusion on a D-DPPC monolayer. In the single molecule concentration regime (pico-molar) there is no tendency for PLA_2 to accumulate at the LC-domain boundaries.

Chapter 7

Summary and outlook

In this study, a wide-field fluorescence microscope (WFM) was constructed and fitted with a Langmuir trough which allowed for the use of a high numerical aperture microscope objective. The setup was used to study three different phenomena:

- Phospholipid phase behaviour
- Lipid diffusion
- Enzyme activity and dynamics

All of these processes, which relate to the lateral organisation of the lipid structures, are important in biological systems and all of these are highly dynamic processes. This study has shown that the well-established Langmuir technique can be used to gain knowledge of processes occurring in and on the lipid monolayer structure using different fluorescence techniques with single molecule sensitivity at millisecond time-resolution.

The first achievement of this study was the construction of the WFM/Langmuir trough setup. In its final version, it was as easy to perform monolayer studies on a 100 μm subphase as on a traditional mm-sized subphase. This is an important improvement which makes it possible to apply up-to-date single molecule detection (SMD) techniques. The versatility of the instrument is proved by the different types of studies performed herein. However, the setup could benefit from further improvements. Especially an additional laser line (or two) as well as a high frequency shutter synchronised with the camera. An available blue laser line was already installed in the WFM during this project, but its 20 mW output was often insufficient for homogenous wide-field illumination of the sample. The laser lines should provide powers on the order of 200mW to obtain reasonable excitation irradiance of the sample (cf. Table 2). The shutter is of course important to minimise bleaching, and in practice allows higher excitation irradiances to be used during image acquisition. One may also install a beam splitter (e.g. polarising, dichroic, or 50/50 (aka half-silver) mirror) splitting the signal between the EMCCD camera and the avalanche photodiodes (APD). This would allow simultaneous image acquisition and fluorescence correlation spectroscopy to be performed, so different areas of inhomogeneous lipid structures could be studied in greater detail.

The first of the three studies performed with the Langmuir trough confirmed the well-described structure of LC-domains in the main phase transition; the LE-LC phase co-existence region. The less-well studied gas-to-liquid expanded phase transition was

also studied and its complex morphology was directly visualised. From the experimental data the width of the G-to-LE transition was estimated by extrapolation from the liquid expanded (LE) phase to the gas (G) phase. The extrapolation showed that the width of the phase transition is several thousand square-angstroms (Å^2). Although the extrapolation is subject to a large uncertainty, it clearly shows that phospholipid monolayers, when initially spread at an air-water interface, generally are in a non-equilibrium meta-stable state.

The second study, a fluorescence correlation spectroscopy (FCS) study of lipid diffusion in a lipid monolayer, showed that the diffusion coefficients (*D*) decreased from 100 μm^2/s to 10 μm^2/s when the surface pressure was increased from 5 mN/m to 40 mN/m which meant changing the mean molecular area (MMA) from 80 Å^2 to 50 Å^2. The finding that the diffusion coefficient is closely related to the thermodynamic variable surface pressure (Π) should be investigated further. First of all because surface pressure is much more well-defined than free-area, especially when the MMA approaches the hard core area of the lipid (~42 Å^2). In this region, small errors in the determination of the MMA, will contribute to large errors in the reciprocal free area (cf. Fig. 5.5). Secondly, a relation between the surface pressure and the diffusion coefficient may help to determine the lateral pressure in bilayer structures (membranes). This has so far not been possible to determine. Yet, lateral pressure is hypothesized to play an important role in controlling the function of transmembrane proteins (O. G. Mourritsen, R. Cantor, personal communications). It was also shown that lipid fluorophores tend to partition along grain boundaries (Fig. 5.6). This effect cannot be seen at high lipid fluorophore concentrations where the image contrast appears homogenous in the LE and S phases. This is of general practical importance. It may explain the variety of reported diffusion coefficients in the literature, because the diffusion coefficient in inhomogeneous systems is highly dependent on the time and length scale of the experimental technique. It also shows that care should be taken when assuming (ideal) mixing of different lipid species under different experimental conditions.

The third and final study investigated the activity and diffusion behaviour of PLA_2 on a monolayer in the LE-LC phase co-existence region (the main transition). It was shown that porcine pancreas PLA_2 (Type IA) degrades the LC-domains in a similar fashion to that seen in previous studies on venom PLA_2 (Type IIB) creating channel-like structures which infiltrate the LC-domain structure. Studies using low concentrations of labelled enzyme show that these channels are not the first reaction to enzyme activity. Prior to the channel-formation, product domains are formed. These are believed to increase the activity of PLA_2 by two mechanisms. First, the negative charge of the product molecules will bind the positively charged *i-face* region of the enzyme to the lipid structure, keeping the enzyme in the most favourable configuration for lipid protrusion. Second, hydrolysis, and accumulation of product molecules in the lipid structure, creates structural defects (imperfect lipid packing) which further facilitate lipid protrusion. The diffusion behaviour of PLA_2 was also investigated by single particle tracking (SPT). The diffusion coefficient was found to depend on the lipid composition. The fastest diffusion was found on a D-DPPC monolayer which was not susceptible to hydrolysis (4.6 μm^2/s), slightly slower diffusion was found on the LE-region of a DPPC monolayer (2.7 μm^2/s) which is believed to be related to hydrolytic action and the presence of product

molecules. By far the slowest diffusion was found on the charged product domain (0.16 $\mu m^2/s$). In all cases, the residence times of the enzyme on the monolayer was found to be short (~100 ms), which corresponds to a 'hopping mode' mechanism. Hopping mode was not expected on the product domain and should be investigated further; potentially on monolayers of varying product composition, or monolayers consisting of negatively charged phospholipids (e.g. a phosphatidyl-glycerol). The effect of calcium or magnesium, which can screen the charges, could also be investigated to see if they are responsible for the lack of long term binding ("scooting") in this study. Finally, in a study where the adsorption of PLA_2 was studied at different surface pressures, it was shown that adsorption is highly dependent on the state of the monolayer. As long as the monolayer was in the LC-phase the enzyme was able to adsorb to and diffuse on the monolayer. However, when the monolayer was compressed into the solid (S) phase then adsorption became extremely restricted, and the few enzymes that did adsorb were largely immobile in distinct regions of the monolayer. For a future study, it would be interesting to perform experiments on a DPPC monolayer in the LE-LC phase co-existence region with only a small percentage of the enzymes labelled. That way, it would be possible to visualise the distribution and behaviour of single enzymes inside a hydrolysis induced channel. This was not done conclusively in the present study. Additional laser lines, as suggested above, would also make it possible to excite the monolayer and enzyme independently. This would make it possible to obtain information on the dynamics of the enzyme and the morphology of the monolayer simultaneously.

Appendix

A. Methods and materials

B. Monolayer preparation

C. Various little calculations

A. Methods and materials

A.1 Suppliers of chemicals

DPPC (1,2-dipalmitoyl-sn-glycero-3-phosphocholine), and DMPC (1,2-dimyristoyl-sn-glycero-3-phosphocholine) were purchased from Avanti Lipids (Alabaster, US). TRITC-DHPE n-(6-tetramethylrhodaminethiocarbamoyl)-1,2-dihexadecanoyl-sn-glycero-3-phosphoethanolamine, triethyl-ammonium salt, DiI (1,1'-dioctadecyl-3,3,3',3'-tetramethylindocarbocyanine perchlorate), R6G (xanthylium, 9-(2-(ethoxycarbonyl)phenyl)-3,6-bis(ethylamino)-2,7-dimethyl, chloride) were purchased from Invitrogen (Molecular Probes). D-α-DPPC (2,3-dihexadecanoyl-sn-glycero-1-phosphocholine) was from Sigma-Aldrich. Sodium chloride (NaCl) Trizma® base, and Trizma HCl® (Luminescence grade) was from Fluka Biochemika. Calcium chloride-dihydrate ($CaCl_2 \cdot 2H_2O$), methanol, ethanol, and n-hexane were purchased from Merck KGaE (spectroscopic grade). All chemicals were used as received. Water: In all steps involving water, the water was purified on a desktop Millipore system (> 18 MΩcm).

Porcine pancreatic phospholipase A_2 was obtained through collaboration with Dr. Allan Svendsen, Novozymes A/S, Denmark.

The NHS ester of p-PDI [CAS number: 817207-4-7] and the NHS-ester binding solid support microspheres obtained through collaboration with prof. Dr. Klaus Müllen, Max Planck Institute, Mainz, Germany.

A.2 Labelling of PLA2 with PDI

Labelling of PLA_2 with PDI was done by mixing appropriate amounts 0.15 mM porcine pancreas PLA_2 with 8 mM PDI-NHS in PBS buffer (200 mM, pH 8) to a final p-PDI to PLA_2 ratio 25:1. The mixture was left to react for 3 hours at 4 °C in the dark. Separation of the labelled PLA_2 (PDI-PLA_2) from the un-reacted dye was accomplished by addition of 40 mg of solid support microspheres (see below) and incubation for 2 minutes. Labelled enzyme was subsequently isolated from the solid support microspheres by filtration through a 0.2 μm Supor® nylon membrane. To insure virtually all un-reacted dye was separated from the PLA_2-PDI solution, several spin filtrations (3 kDa cut off) were performed. Labelling resulted in an average of 2-3 fluorophores per PLA_2; determined by UV-VIS spectroscopy and by stepwise bleaching of PLA_2-PDI conjugates immobilized on a glass surface.

A.3 Experimental protocol (Chapter 4): Morphology of DPPC monolayers

DPPC solutions were prepared in n-hexane/ethanol (95/5 vol%) at a concentration of 0.6 mg/mL. The relative amount of TRITC-DHPE was 0.1 mol%. All experiments were performed at room temperature 20-22 °C, and all experiments were repeated at least three times.

The formation of gas bubbles was done by the usual spreading and formation of a DPPC monolayer. The monolayer was compressed into the liquid-expanded (LE) phase at a surface pressure of Π = 2-4 mN/m, before it was again relaxed into the 'gas'–'liquid-expanded' (G-LE) phase co-existence region. The relaxation was done at several different rates. The fastest rate was 5 $Å^2$/lipid/min, the slowest was 0.5 $Å^2$/lipid/min.

Images of DPPC monolayers presented herein are all from experiments using TRITC-DHPE. Images were recorded on a Andor Ixon+ DU-897 EMCCD camera (512*512 pixels, pixel dimension 16 x 16 μm). Magnification was 60x (Olympus 60×, UPLAPO, working distance 0.25mm, N.A. 1.2) giving maximal image dimensions of 137 μm x 137 μm. Excitation irradiance ($I_0/2$) was set to ~ 1 kW/cm².

A.4 Experimental protocol (Chapter 5): Lipid diffusion in monolayers

A.4.1 FCS measurements on DMPC monolayers

DMPC solutions were prepared in either n-hexane/ethanol (95/5 vol%) or n-hexane/methanol (99.9/0.1 vol%). The lipid to lipid fluorophore ratio was between 1:50,000 and 1:200,000 (~10^{-3}-10^{-5} mol%).

The lowest lipid-to-lipid fluorophore ratio yielded ~1-2 fluorophores in the focus which gave maximal amplitudes in the time-auto correlation functions (time-ACFs), and thus in principle the optimal S/N ratio due to the strong signal fluctuation (Kask, Gunther et al. 1997). The measured diffusion times were independent on the lipid ratio used.

All FCS measurements on DMPC monolayers presented herein were performed with TRITC-DHPE as lipid fluorophore at 20 ± 0.5°C or 22 ± 0.5°C.

All experiments were repeated at least three times using slightly different compression rates (~1-2 Å²/lipid/min) and waiting times between measurements without any systematic influence on the measured values. Most of the experiments were performed by first compressing to high pressure (> 40 mN/m) and then performing FCS measurements as pressure was stepwise released. This method was preferred for practical reasons; it allowed a continuous compression isotherm to be recorded and it also provided a check that leak proof monolayer conditions were obtained before FCS measurements were initiated.

Prior to recording fluorescence traces (i.e. intensity as a function of time), the monolayers were left to equilibrate at the target pressure for 5-15 minutes with the barriers set to maintain constant pressure. The barriers were then stopped and FCS measurements initiated with the focus deliberately placed below the air-water interface and thereby with the monolayer out-of-focus. During the FCS measurements the position of the air-water interface spontaneously moved down along the z-axis, bringing the air-water interface first into focus, and then out-of-focus again (with the final focus position above the air-water interface). This method has previously been described and named “time-dependent z-scan” (Benda, Benes et al. 2003; Humpolickova, Gielen et al. 2006).

The duration of each FCS trace was set to 10 seconds with a two second pause in-between each trace. The 10 second duration was the shortest possible time needed to obtain time-ACF’s that could be fitted with good accuracy, and short trace times were preferred in order to minimise possible effects from the monolayer movement along the z-axis (i.e. optical axis). A complete time dependent z-scan typically lasted 30 minutes, and resulted in 150 individual FCS traces. The first and the last traces were often too far from focus and could not be fitted to the time-ACF. On average 60 FCS traces, recorded in the vicinity of the optimal optical focus, of each z-scan were fitted and used to determine the diffusion coefficient at a given pressure.

The radius of the focal volume r_{min} was found by external calibration against Rhodamine 6G with known diffusion coefficient, D_{R6G} = $3 \cdot 10^{-6}$ cm²/s at 22 °C (Magde, Elson et al. 1974). The radius of the observation volume under the applied conditions was found to be r_{min} = 225±10 nm.

Diffusion coefficients *D* were in practice recorded at various surface pressures Π. Subsequently Π was converted to the corresponding MMA by comparison with previously recorded continuously compressed pressure-area isotherms. At least three isotherms of each lipid solution were recorded. This approach was necessary as FCS measurements over a complete range of surface pressures lasted several hours, which was accompanied by lipid loss over time, due to absorption of lipid to barriers, trough edges, and the PTFE ring used to minimise surface flow (Hardy, Richardson et al. 2006).

A.4.2 WFM measurements on DPPC/DiI(C18)

Different lipid fluorophores were tested to find a lipid fluorophore which could partition in the DPPC LC-phase. Such studies have previously been done in our group using differential scanning calorimetry (DSC) on lipid vesicles (Hac, Seeger et al. 2005). Of all the tested lipid fluorophores, both DSC and the present monolayer experiments showed that DiI(C18) had the highest miscibility in the gel/LC phase; although still favouring the fluid/LE-phase. Lipid fluorophores tested using DSC were: DiI(C16)*, DiI(C18)*, TRITC-DHPE*, BODIPY-C16, and DiD(C18). Lipid fluorophores marked with an asterisk where also tested in monolayers, where also Lissamine rhodamine B was tested.

To facilitate lipid fluorophore partitioning (e.g. trapping) in the LC phase, several different spreading solvents and spreading methods were tested. For instance, it was attempted to spread the monolayer lipid from a chloroform solution at a small trough area such that a surface pressure of ~ 40 mN/m was reached without compression. However, upon releasing pressure, the lipid fluorophore was always seen to partition virtually exclusively in the fluid phase of the co-existence region (described further below). Except for this and a few other experiments with the same purpose, the use of chloroform as a spreading solvent was avoided for multiple reasons: (i) It tends to spread quite vigorously on the water surface, making isotherms less reproducible than those where hexane is used, (ii) it has a higher solubility in water than hexane (8 g/L and 0.01 g/L respectively) and differential scanning calorimetry (DSC) has shown that it has a tendency to remain bound to the lipid structure causing shifted heat capacity (melting) profiles if the lipid is not “dried” under high vacuum (Th. Heimburg, personal communication), (iii) and finally, it is a potent carcinogen.

Images of DPPC monolayers presented herein are all from experiments with DiI(C18). As for DMPC measurements, the lipid:lipid fluorophore ratios where in-between 1:50,000 and 1:200,000. Images were recorded on a Andor Ixon+ DU-897 EMCCD camera cooled to -85 °C. Frame rate at full field of view (using all 512*512 pixels) and exposure time 40 ms was 15 Hz. Excitation irradiance ($I_0/2$) was set to ~ 1 kW/cm².

A.5 Experimental protocol (Chapter 6): Activity and diffusion of PLA2

A.5.1 Protocol for visualisation of domain degradation

Buffer for all experiments were Tris 10 mM, pH 8.9, NaCl 150 mM, $CaCl_2$ 5 mM, containing 5 nM porcine pancreas PLA_2. This is the same buffer that was used in the original work by Grainger *et al.*, but the enzyme concentration was approximately 30 times lower enzyme than theirs; 5 nM vs 125 nM.[5] (Grainger, Reichert et al. 1989; Grainger, Reichert et al. 1990)

The lipid (DPPC 0.5 – 0.7 mg/mL) and fluorophore (TRITC-DHPE 0.1 mol%) was deposited from a hexane/methanol 99.9/0.1 to a mean molecular area MMA of ~ 110 Å². The monolayer was

[5] This concentration is based on the following: Grainger et al. injected 0.5 mL of 0.014 mg/ml (1 μM) snake venom PLA_2 into a PTFE ring with dimensions (height * radius = 6 mm * 10 mm; volume of solution inside PTFE ring = 4 mL). Which gives a final concentration of ~125 nM

compressed immediately at a high rate (5 Å²/lipid/min) to MMA ~ 65 (Π ≈ 8 mN/m). All experiments were performed at room temperature (22±1 °C).

The images showing degradation of LC-domains were recorded on an Apogee KX85 CCD camera (pixel array 1300 x 1080, pixel width/height 6.7 μm, chip temperature -18 °C) at an image frequency of 0.3 Hz. The first data series, showing several domains in the field of view, were recorded with an Olympus air objective (40x, NA 0.6, W.D. 2.5 mm, optical resolution = 0.54 μm, pixel resolution = 168 nm/pixel). The images of the single domain was recorded using an Olympus water immersion objective (60x, NA 1.2, W.D. 0.22 mm, optical resolution = 0.27 μm, pixel resolution 112 nm/pixel).

A.5.2 Protocol for single particle tracking

In the "single molecule" experiments, the DPPC monolayer (with no lipid fluorophore embedded) was compressed to the target MMA or pressure before the enzyme was injected. Enzyme injection was done via a Hamilton syringe and the enzyme was deposited in the subphase immediately outside the slit in the PTFE ring. As enzyme diffused into the subphase inside the PTFE ring (and thereby field of view) a surface concentration gradient was created which allowed observation of areas with very high enzyme concentration (Fig. 0.1, left), intermediate enzyme concentration, and low enzyme concentration (Fig. 0.1, right) in a single experiment by simply translating the trough over the microscope objective. This method had several practical advantages; for instance it was possible, within the same sample, to confirm that the enzyme was active (Fig. 0.1, left) and to perform single particle tracking (SPT) experiment (Fig. 0.1, right). This of course meant that the bulk concentration was not known exactly, however the surface density could easily by determined and thereby a rough estimate of the bulk concentration of enzymes in the subphase volume below the observation area could be made based on the following typical values; observation area 3000 μm², subphase height ~ 100 μm, an average of 100 molecules observed at the interface, 1% of bulk enzymes are located at the interface. This estimate typically yielded bulk concentrations of 5 pM. This is in accord with the fact that in

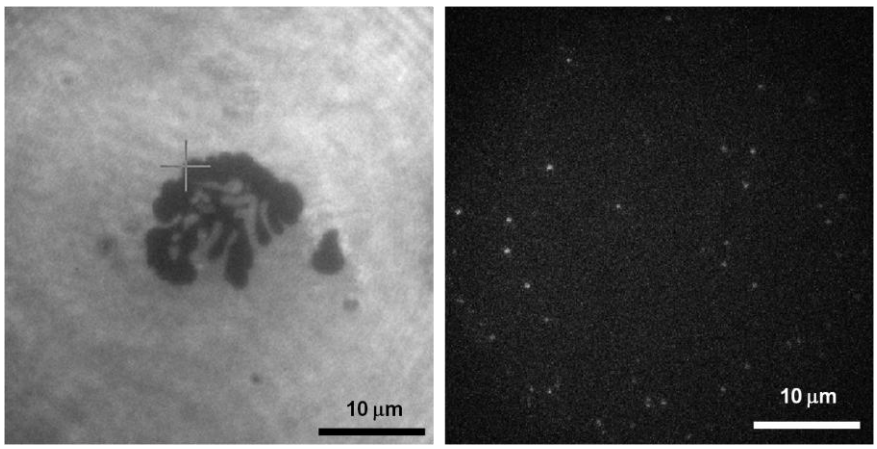

Fig. 0.1 The two extreme situations created by the concentration gradient method **Left**: In regions with high enzyme concentration the usual degradation of LC-domains could be observed **Right**: At the other extreme individual molecules could be observed and SPT could be performed.

experiments where the enzyme was uniformly distributed in the subphase at a bulk concentration of 5 nM the interface appeared saturated with enzyme in the LE-region of the monolayer.

The images visualising the diffusion of single enzymes were recorded on an Andor EMCCD camera cooled to -85 °C (Exposure time 40 ms, EM Gain ~ 250). The final magnification was 150x and done via an Olympus water immersion objective (60x, NA 1.2, W.D. 0.22 mm, optical resolution = 0.27 μm) combined with a 2.5x magnification camera lens. The resulting pixel resolution was 107 nm/pixel.

A.6 Data analysis (Chapter 6): Time evolution of domain degradation

An area of 550 x 550 pixels containing the domain under investigation was cropped from the original full frame images (1300 x 1080 pixels). The cropped image was run through a built-in (Marr type) edge detection routine in Igor Pro software package from WaveMetrics. Approximately half of the binary edge images had to be corrected slightly in order to accurately describe the edge of the domain: Most often, narrow channels were not detected, or detected solely as a single line (i.e. with no area inside).

Determination of the area and perimeter of the LC-domains was done by a combination of the public domain programme ImageJ (available at http://rsb.info.nih.gov/ij/) and Igor Pro.

For the channel analysis, a "zero line" (dotted lines at the mouth of the channels in Fig. 0.2) were added to define the internal area and onset/end of the channel perimeter.

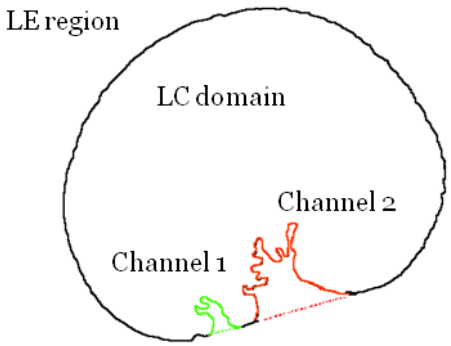

Fig. 0.2 "Edge detected" image with the perimeter of channel 1 and channel 2 highlighted in red and green respectively. The channel areas are defined by means of a "zero line" (dotted line in red and green).

Time zero (t = 0) is defined as the point in time where compression was stopped at a MMA of 65 Å² which is the centre of the phase transition. The time in-between compression stop (t=0), and the time of the first indentation (t=34 min) could not be analysed due to a slow drift of the monolayer. We could therefore only keep the same domain in the field-of-view for ~45 minutes; i.e. the domain in Fig 5.5A had drifted out of the field-of-view by the time channel-growth started.

A total of 65 images showing the time-evolution of the channel-like structures penetrating into the LC-domain were analysed.

A.7 Data analysis (Chapter 6): Single particle tracking

The tracking of single enzyme trajectories was performed by collaborators at the Division of Molecular and Nano Materials, Katholieke Universiteit Leuven, Belgium using a home-built Matlab® routine developed for a similar experimental series using PLA1 (Rocha, Hutchison et al. 2008). The enzymes were located with a precision of ~100 nm for slowly diffusing enzymes and ~200 nm for quickly diffusing enzymes.

The enzyme trajectories were analysed using two different methods: Weighted mean square displacement and cumulative distribution function. Both are described thoroughly in the literature (Saxton 1997; Schutz, Schindler et al. 1997). The essence for both methods is that the diffusion constant is best characterised at short diffusion times. In Saxton's method, the individual trajectories ($\langle r^2 \rangle$ vs. t) are analysed, but with the displacement over short time intervals weighted heavily (cf. Eq. (G.1) and Fig. 0.3)

$$\left\langle r^2 \ n \right\rangle = \frac{1}{N_{T-n+1}} \sum_{i=0}^{N_{T-n+1}-1} \left[\vec{r}\ i+n \ - \vec{r}\ i \right]^2 \tag{G.1}$$

where $\langle r^2(n) \rangle$ is the mean square distance for the time lag n, N_T is the total number of time steps (= data points is the trajectory).

In the method by Schütz *et al.*, the MSD at different time lags for multiple trajectories are analysed collectively. The result is given as a single probability function $P(r^2,\tau)$ which describes the probability of finding a particle within a circle of a given radius r after a time lag τ

$$P(r^2,\tau) = 1 - \exp\left(\frac{r^2(\tau)}{\left\langle r^2(\tau) \right\rangle} \right) \tag{G.2}$$

where $\tau = \Delta t$; the time between two consecutive images. This method is reffered to as Cumulative Distribution Function or simply CDF in the following.

The two methods of analysis have each their strengths and weaknesses. The method proposed by Saxton is the most intuitive and clearly show if the diffusion behaviour of a single particle changes during a trajectory; e.g. if a freely diffusion particle becomes immobilised. On the other hand, the CDF method yields better statistics, especially when many short trajectories are known (Saxton 1997).

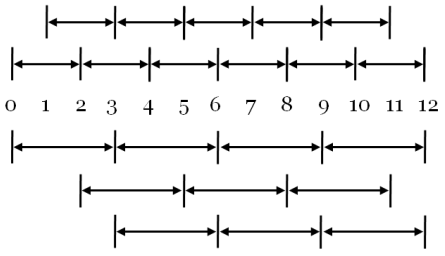

Fig. 0.3 The basis for the (Saxton) weighting method: Consider a trajectory of 11 steps. Now the MSDs for time lags t = 2 are determined for all pairs separated by two time steps resulting in 11 individual values for MSD(t = 2) and thus 11 diffusion coefficients. For time lag t = 3, 10 individual diffusion coefficients are obtained, and so forth. Finally, for time lag = 11 (where the diffusion coefficient is the least well-characterised) only one value for D is obtained.

B. Monolayer preparation

B.1 Procedure for cleaning the Teflon monolayer trough

1) Before each experiment the trough was cleaned by wiping it over with dust free wipes soaked ethanol, followed by squirting with large amounts of lukewarm ethanol, and finally milli-Q water.
    i. Every 1-2 weeks, the trough was completely immersed in Deconex-90 over night to remove trace impurities.
    ii. Following enzyme experiments, the trough was left under hot running tap water for 15-20 minutes.
2) The trough was then mounted on the microscope setup, where it was filled to the brim with milli-q water.
3) During repeated compression and relaxation cycles the aqueous surface was cleaned by continuous aspiration. To compensate for the amount of subphase which was sucked off, milli-Q water or buffer was regularly added behind the barriers.
4) The surface was considered clean when a complete compression of the clean surface did not give rice to a pressure increase of more 0.1 mN/m.

B.2 Procedure for creating lipid monolayers

1) The cleaned trough (including metal ring with coverglass) was filled with milli-Q water until the subphase height over the coverglass was approximately a few millimetres (much higher than during measurements).
2) The lipid was deposited from the stock solution by carefully placing small drops (< 0.5 μL) of solution on the water surface using a Hamilton syringe in an appropriate amount so the mean molecular area was > 110 Å^2 when the barriers were in their initial fully expanded position. Typically a volume af ~10 μL when the stock solution was ~0.6 mg/mL.
3) The solvent was allowed to evaporate for 5-15 minutes (in some enzyme experiments compression was started immediately. See below).
4) Before starting monolayer compression, the microscope objective was positioned with the focus ~80-100 μm above the top side of the coverglass in the trough. Subsequently subphase was removed (typical volume ~5 mL) until the subphase height was also ~80-100 μm and the air-water interface was within the optical focus.
5) Before starting the compression, the acrylic box was sprayed with milli-Q water to ensure a high humidity, minimising evaporation of subphase during the experiment
6) Compression was usually performed continuously until the desired surface pressure, mean molecular area, or monolayer collapse. Typically compression was done at rates of 0.5 Å^2/lipid/min. The highest used compression rate used for results presented herein was 5 Å^2/lipid/min.

If otherwise is not specifically stated, then the monolayer experiments were performed at room temperature (20-22 °C) to minimise convection due to temperature gradients and vibrations from the cooling plate.

B.3 Procedure for gluing coverglasses

Before gluing the coverglasses (thickness #00, ø = 25 mm) onto the metal rings, the coverglasses were cleaned in acetone, Deconex 11 Universal, rinsed with milli-Q water (> 18 MΩcm), and stored in methanol until use. Gluing to the metal ring was done using UV curing adhesive (Loctite® 358). To maximise binding strength the top surface of the ring was scratched using sand paper and immediately before adding the glue the ring was heated to 35 °C to make the glue spread more evenly. The coverglass was then gently pressed onto the ring making sure that the glue completely covered the interface between the glass and the metal. To avoid tension in the coverglass, the ring was allowed to cool to room temperature before curing by exposure to UV. The top side was irradiated for 30 min at 365 nm. The back side was additionally irradiated at 254 for 30 min. The short wavelength was necessary for glue exposed to air to cure. Excess adhesive, typically on the side of the ring, was removed using small amounts of acetone. Although full curing should occur within minutes, it was clearly observed that allowing cover glasses and rings to rest for several days after gluing produced far more durable components. For this reason, a number of metal rings were made, so a stock was always available. Immediately before use, the metal ring-coverglass components were again cleaned thoroughly using water bath sonication in acetone, Deconex® 11, ethanol, and finally milli-Q water.

C. Various little calculations

C.1 Lipid turnover number for PLA_2

Here we will try to get an estimate for the turnover rate of lipid molecules during PLA_2 catalysed hydrolysis at the LC-domain boundary. This estimate is based on (FIGURE OF DOMAIN) and (PLOT OF DA/DT). It was found that during the initial stages of hydrolysis there is a correlation between the perimeter *P* and the rate of 'channel area increase' dA/dt into the LC-domain. This correlation had the form and value

$$\frac{dA}{dt} \propto \alpha \cdot P = 0.4\ {}^{\mu m}\!/_{\min} \cdot P \tag{C.1}$$

We now equate the 'channel area increase' directly to hydrolysis of the lipid molecules in the LC-domain. Since the average area of a single lipid molecule is known, we can calculate the approximate number of molecules in one μm² of LC-domain structure

$${}^{Lipids}\!/_{um^2} = \frac{10^8\ {}^{\text{Å}^2}\!/_{\mu\text{m}^2}}{50\text{Å}^2 / lipid} = 2 \cdot 10^6 \tag{I.2}$$

We also know the dimensions of the enzyme molecules, which we for simplicity say is spherical with a diameter of 5 nm. Assuming that the enzymes sit shoulder-by-shoulder along the LC-domain boundary we find that 1 μm of perimeter accommodates no more than 200 enzyme molecules at any given time. Retuning to Eq. (C.1) we can now estimate the turnover rate of lipid molecules per enzyme

$$\frac{d(\text{lipid})}{dt} \propto \frac{0.4\ {}^{\mu\text{m}}\!/_{\text{min}} \cdot 2 \cdot 10^6\ {}^{\text{lipid}}\!/_{\text{um}^2}}{200\ {}^{\text{N}_{\text{Enz}}}\!/_{\mu\text{m}} \cdot 60\ {}^{\text{s}}\!/_{\text{min}}} = 70\ {}^{\text{lipid}}\!/_{\text{N}_{\text{Enz}} \cdot \text{s}} \tag{I.3}$$

Which is the number stated in the main body of the text.

As mentioned in the text, both the number of enzymes and the perimeter are subject to uncertainty. We have little evidence that the all of the perimeter is covered in active enzymes constantly (which also requires that the total perimeter is activated for hydrolysis). This can lead to an underestimation of the turnover rate of the enzyme. Conversely, the perimeter could potentially be underestimated since the resolution of the microscope (270 nm) is far above the size of the lipid molecules (10 Å²) and thus potentially the true (fractal) structure of the LC-domain boundary (Mandelbrot 1967).

C.2 Estimation of fluorescence collection quantum yield

The fluorophore used in this study was a perylene derivative 'PDI' made water soluble by adding sulfonyl substituents (-HSO_3) in the "bay" positions (Jianqiang Qu 2004). The extinction coefficient is $\varepsilon \sim 21000$ $M^{-1}cm^{-1}$ at 532 nm (Jianqiang Qu 2004; Margineanu, Hofkens et al. 2004) and the fluorescence quantum yield is $\Phi_f \sim$ 0.6- 1 (Tang, Peneva et al. 2007).

In single molecule fluorescence studies it is useful to estimate the net fluorescence signal (brightness) from single PDI molecules. For this it is necessary to calculate a rough number of the expected emission of photons from the PDI molecule and the collection quantum yield of the microscope setup. For this purpose it is convenient to convert the molar extinction coefficient ε to an absorbance cross-section σ. This can be done using the two different forms of the Lambert-Beer law; e.g. (Alberty and Silbey 1996; Lakowicz 2004)

$$A = \log\frac{I_0}{I} = \varepsilon c l \tag{I.4}$$

and

$$\frac{I}{I_0} = e^{-\sigma \cdot N \cdot l} \tag{I.5}$$

where A is absorbance, I_0 the irradiance of incident light (W/cm²), I the irradiance of transmitted light (W/cm²), c the concentration (M), l the light path length trough the sample (cm), x the light path length trough the sample (m), σ the absorption cross-section (cm²), N the particle density (molecules/cm³). From this we find that

$$\sigma_{PDI} = \frac{2.3 \cdot \varepsilon \cdot c \cdot l}{N \cdot x} = \frac{2.3 \cdot \varepsilon}{N_A} = \frac{2.3 \cdot 21{,}000 \mathrm{M^{-1}cm^{-1}}}{6.0 \cdot 10^{23} \mathrm{mol^{-1}} \cdot 10^{-3} \mathrm{L/cm^3}} = 8.1 \cdot 10^{-17} \mathrm{cm^2} \tag{I.6}$$

Although expressed in units of area, σ is still a measure of the probability of light absorption, and not the fluorophores space-filling area. From the cross-section we can now determine the number of photons absorbed by a PDI molecule per second

$$k(\mathrm{abs}) = \frac{I_0 \cdot \sigma}{E_{photon}} \tag{I.7}$$

where E_{photon} is the energy of photons at 532 nm found from Planck's law

$$E_{photon} = \frac{h \cdot c}{\lambda} = 3.7 \cdot 10^{-19} \mathrm{J} \tag{I.8}$$

where h is Planck's constant ($6.6 \cdot 10^{-19}$ J·s), and c the speed of light in vacuum ($3.0 \cdot 10^8$ m/s). Inserting I_0 = 0.6 kW/cm² as the excitation irradiance of the laser, Eq. (I.7) yields

$$k(\mathrm{abs}) = 1.3 \cdot 10^5 \, s^{-1} \tag{I.9}$$

The fluorescence lifetime of PDI in water has been reported to be $\tau_f \sim$ 5 ns (Margineanu, Hofkens et al. 2004), which is three order of magnitude faster than each absorption event (= 1/A'). It is therefore reasonable to use the approximation that fluorescence emission is instantaneous. In addition, the rate of intersystem crossing (k_{ISC}) is reported to be close to zero leading to a virtually

unpopulated triplet state. Thereby the rate of fluorescence emission k(em) is approximately given by

$$k(\mathrm{em}) = \Phi_f \cdot k(\mathrm{Abs}) = 8 \cdot 10^4\ s^{-1} \tag{I.10}$$

Unfortunately not all of these photons are collected. By far the biggest loss is due to the isotropic emission of fluorescence (i.e. photons are emitted in all directions). The collection efficiency of a microscope objective can be found by integrating the emission from a point source over the total volume and is approximately

$$\eta_{obj} = \frac{1}{4\pi} \int_0^{2\pi} d\phi \int_0^{\theta} \sin\theta \, d\theta \approx 28\% \tag{I.11}$$

where θ is the collection half-angle (64.5°). A smaller loss of signal is caused by the filter sets needed to block the excitation light from reaching the camera (namely the dichroic mirror and the emission filter). Although PDI has a relatively large Stokes' shift (which in practice means that only a small amount of the fluorescence signal has the wavelength of the blocked laser light), a part of the emitted signal will always be discriminated by the filters. For high quality filters sets, as used here, a 10% loss of signal is estimated. Finally, ~ 10% of the remaining signal is lost at the camera resulting in total collection efficiency of

$$\eta_{total} \approx \eta_{obj} \cdot \eta_{filters} \cdot \eta_{EMCCD} \approx 23\% \tag{I.12}$$

The final signal, i.e. the total number of photons collected for the exposure time t_{exposure}, can be estimated from

$$N_{photons} = k \cdot (\mathrm{em}) \cdot t_{\mathrm{exposure}} \cdot \eta_{total} \tag{I.13}$$

which results in an order of 1000 photons for a typical exposure time of 40 ms exposure. Using an objective with N.A. 1.2 and exciting at 532 nm, the radius of the airy disc (i.e. 84% percent of the emitted light from a point source) is 270 nm. This means that a particle which is immobile on the time scale of the exposure will spread over ~ 16 pixels on the CCD chip. This will result in only ~ 50 photons on each CCD chip pixel for an immobile particle, and readily explains the need a very sensitive EMCCD camera and a well-calibrated optical path. A note for the experimentalist: Since the images are contrast images, and the investigated species are usually mobile particles, then a longer exposure time does not necessarily result in better image quality. Often, the signal at longer exposure times will simply tend to spread over more camera pixels leading to reduced contrast. Sometimes less is more!

C.3 Spot size versus diffusion coefficient

Is there a simpler way to determine the diffusion coefficient than to track the motion of every single particle in every single frame? This question was inspired by the experiment described in Section 6.2.6, where the adsorption and diffusion PLA_2 was visualised at different pressures. Very briefly:

- at Π = 20 mN/m, the average surface density of enzymes was 24 enzymes/1000 μm^2 and two diffusion coefficients were found D = 2.2 $\mu m^2/s$ and D = 0.1 $\mu m^2/s$
- at Π = 25 mN/m, the average surface density of enzymes was 2 enzymes/1000 μm^2 and one diffusion coefficient was found D = 0.1 $\mu m^2/s$

From the obtained image series (1500 images analysed for each pressure) it was apparent from that the spot size produced by the diffusing particles at Π = 20 mN/m, was much wider than the spot size produced by the particles diffusing on the monolayer at Π = 25 mN/m. This leads us to recap what was described in Section 2.3.2;

> *The fluorescence signal from a point source creates an airy disc in the image plane of the microscope (Fig. 2.9). The central airy disc contain 84% of the signal intensity, and its width is given by the resolution of the optics (cf. Eq. (2.31)).*

In practice, however, the point sources (e.g. the fluorophores) move during the exposure time of the camera. Thus they produce a spot significantly larger than the size of diffraction limited airy disc. It is trivial to note that the faster the particle moves the larger the resulting spot in our image spot. However it is interesting to speculate whether we can determine the diffusion coefficient of the particle from the size of the resulting spot? In the following we will turn this question around an estimate the spot size produced by a particle with a given diffusion coefficient after a (fixed) time lag of 40 ms, which was the actual exposure time used in the experiment.

Two typical spot sizes were shown in Fig. 6.13 (right), these are also shown in Fig. 0.4; where

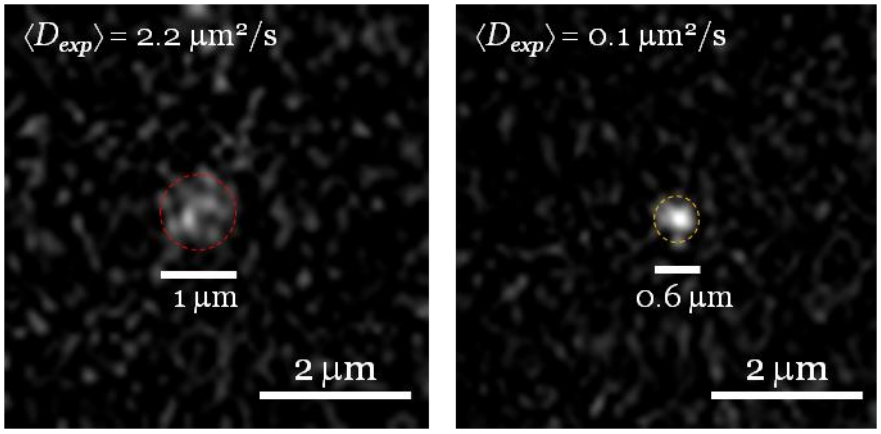

Fig. 0.4 Two random spots from the experiment described in Section 6.2.6. The spots shown are the same as in Fig. 6.13 (right), only here the contrast has been increased ~40%. Both spots were recorded using an exposure time τ_{exp} = 40 ms. **Left**: Spot recorded at a surface pressure Π= 20mN/m. The diameter of the spot in the image is ~1 μm^2. The average diffusion coefficient measured for the fast diffusion component in the experiment was 2.2 $\mu m^2/s$. **Right:** Spot recorded at a surface pressure Π= 25 mN/m. The diameter of the spot in the image is ~0.6 μm^2. The average diffusion coefficient measured for all the particles in the experiment was 0.1 $\mu m^2/s$.

they have been digitally magnified and contrast enhanced. It is apparent that the spot size in the left panel is wider (and less bright) than the spot size in the right panel. In the images the experimentally determined average diffusion coefficients D are given. These were determined from several hundred particles displacements, whereas we shall only use one image for the spot-size determination of the diffusion coefficient done here.

The probability density distributions (PDF) for the two particles with the diffusion coefficients D found in the experiment (0.1 μm²/s and 2.2 μm²/s) are shown in Fig 0.5. The red curves gives the probability P(r^2, 40 ms) of finding a particle with the given diffusion coefficient within a circle of square radius r^2 after a time lag of 40 ms. The blue curve gives the probability P(r, 40 ms) for the radius r. The average square displacement of the exponential decay is found at P = 1/e (63%), which is (of course) equivalent to the 'mean square displacement' (MSD = 4·D·t). However, for the estimate of the spot size we will use the narrower distribution P(r^2, 40 ms) = 50%, which is the square displacement of 50% of the particles during the 40 ms exposure. This quantity is given by

$$\mathrm{P}_{50\%}\ r^2, 40\ \mathrm{ms}\ = \mathrm{MSD} \times \ln 2 \tag{I.14}$$

We also see that

$$\mathrm{P}_{50\%}\ r, 40\ \mathrm{ms}\ = \sqrt{\mathrm{MSD} \times \ln 2} \tag{I.15}$$

Knowing this we return to the airy disc. If the particle is completely immobile, then the observed spot will have R = 540 nm/ 2 = 270 nm. However, if the particle during the 40 ms exposure has performed a random walk within a circle of radius r approximated by Eq. (I.15) then the size of the spot will become the simple sum of the airy radius and the random walk radius

$$r_{observed\,spot} = r_{Airy\,spot} + r_{random\,walk} \tag{I.16}$$

which is

$$r_{spot} = \frac{1.22 \cdot 532\mathrm{nm}}{2 \cdot \mathrm{NA}} + \sqrt{\mathrm{MSD} \times \ln 2} \tag{I.17}$$

Which, for t = 40 ms, reduces to

$$r_{spot} = 270 + 0.333 \cdot \sqrt{D} \tag{I.18}$$

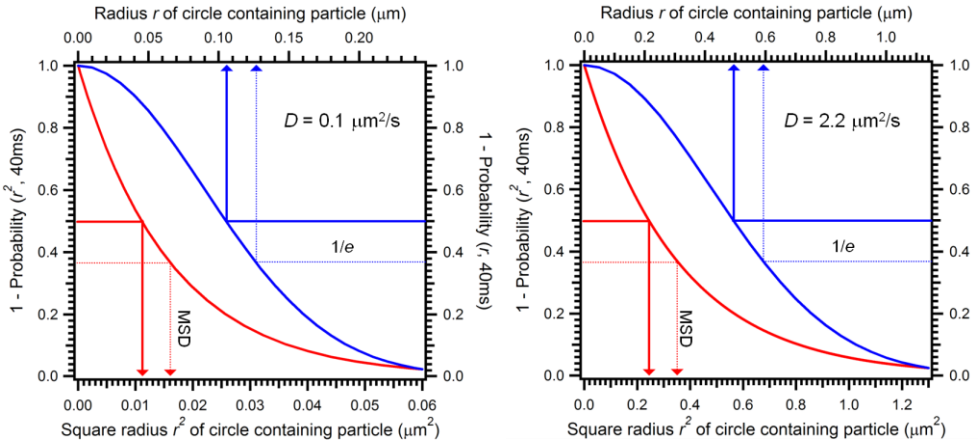

Fig 0.5 Probability distribution function (PDF) for square displacements (red curve) and displacements (blue curve). **Left:** PDF for a particle with diffusion coefficient D = 0.1 μm²/s. MSD(40 ms) = 0.016 μm². **Right:** PDF for a particle with diffusion coefficient D = 2.2 μm²/s. MSD(40 ms) = 0.352 μm².

We have assumed the particles explore all areas of the circle during the random walk. This is a fair approximation for short trajectories but not for long trajectories because long trajectories will not fill the area within the circle uniformly. Eq. (I.18) is plotted in Fig 0.6. The radius of the area predicted for the two particles from the experiment (Fig. 0.4) are highlighted (dotted lines) and have values for r_{spot} (D=0.1 μm²/s) = 0.38 μm, and r_{spot} (D=2.2 μm²/s) = 0.76 μm which are not too far off the measured values (~0.3 μm² and 0.5 μm² respectively).

A test of this method will require an analysis of a complete data set where the diffusion coefficient is measured by several methods; e.g. fluorescence correlation spectroscopy FCS, single particle tracking SPT, and this novel spot size method. As noted, since the trajectory of a particle performing a random walk does not fill the area uniformly, a correction factor would probably be needed for relative high diffusion coefficients. Also in practice, a higher optical magnification would be desirable. At present the width of a camera pixel correspond to 107 nm on the sample (pixel resolution). However, as always, there is a direct trade-off between magnification and signal, and at higher optical magnification, the less photons will arrive at each pixel giving an inferior signal-to-noise ratio.

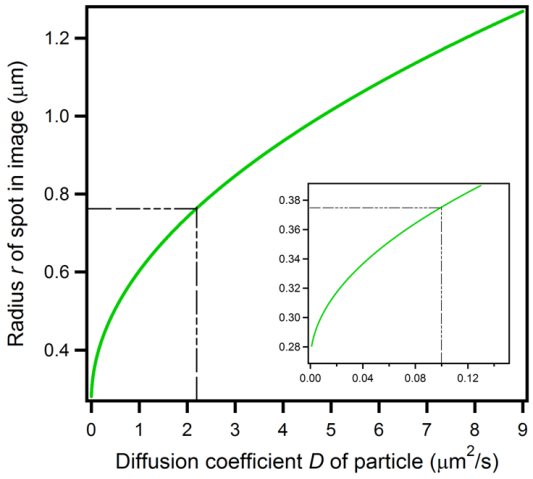

Fig 0.6 Graphical representation of the relation in Eq. (I.18). Inset: Detailed view of the region relevant for a particle with D = 0.1 μm²/s.

References

Abbe, E. (1873). "Beiträge zur Theorie des Mikroskops und der mikroskopischen Wahrnehmung." Arch. mikrosk. Anat. Entwichlungsmech. **9**: 413-468.

Alberty, A. R. and J. R. Silbey (1996). Physical Chemistry, John Wiley & Sons, Inc.

Albrecht, O., H. Gruler, et al. (1978). "Polymorphism of Phospholipid Monolayers." Journal De Physique **39**(3): 301-313.

Almeida, P. F. F. and W. L. C. Vaz (1995). Lateral Diffusion in Membranes, Elsevier, Amsterdam.

Almeida, P. F. F., W. L. C. Vaz, et al. (1992). "Lateral Diffusion in the Liquid-Phases of Dimyristoylphosphatidylcholine Cholesterol Lipid Bilayers - a Free-Volume Analysis." Biochemistry **31**(29): 6739-6747.

Axelrod, D., D. E. Koppel, et al. (1976). "Mobility measurement by analysis of fluorescence photobleaching recovery kinetics." Biophys. J. **16**(9): 1055-1069.

Balashev, K., M. Gudmand, et al. (2003). "Humicola lanuginosa lipase hydrolysis of mono-oleoyl-rac-glycerol at the lipid-water interface observed by atomic force microscopy." Biochimica Et Biophysica Acta-Biomembranes **1615**(1-2): 93-102.

Batchinski, A. J. (1913). "Untersuchungen über die innere Reibung der Flussigkeiten." Zeitschrift für Physikalische Chemie **84**: 643.

Benda, A., M. Benes, et al. (2003). "How To Determine Diffusion Coefficients in Planar Phospholipid Systems by Confocal Fluorescence Correlation Spectroscopy." Langmuir **19**(10): 4120-4126.

Berg, O. G. (1985). "Orientation Constraints in Diffusion-Limited Macromolecular Association - the Role of Surface-Diffusion as a Rate-Enhancing Mechanism." Biophysical Journal **47**(1): 1-14.

Berg, O. G., M. H. Gelb, et al. (2001). "Interfacial enzymology: The secreted phospholipase A(2)-paradigm." Chemical Reviews **101**(9): 2613-2653.

Berg, O. G., J. Rogers, et al. (1997). "Thermodynamic and Kinetic Basis of Interfacial Activation: Resolution of Binding and Allosteric Effects on Pancreatic Phospholipase A2 at Zwitterionic Interfaces." Biochemistry **36**(47): 14512-14530.

Blom, H. (2003). Correlation spectroscopy of single emitters - fundamental studies and applications related to quatum optics and life sciences. Department of

Microelectronics and Information Technology. Laboratory of Optics, Photonics and Quatum Electronics. Stockholm, Royal Institute of Technology (KTH). **Ph.D. Thesis**.

Bockmann, R. A., A. Hac, et al. (2003). "Effect of sodium chloride on a lipid bilayer." Biophysical Journal **85**(3): 1647-1655.

Bonsen, P. P. M., Vandeene.Ll, et al. (1972). "Studies on Phospholipase a and Its Zymogen from Porcine Pancreas .4. Influence of Chemical Modification of Lecithin Structure on Substrate Properties." Biochimica Et Biophysica Acta **270**(3): 364-372.

Brezesinski, G., A. Dietrich, et al. (1995). "Influence of Ether Linkages on the Structure of Double-Chain Phospholipid Monolayers." Chemistry and Physics of Lipids **76**(2): 145-157.

Brezesinski, G. and H. Mohwald (2003). "Langmuir monolayers to study interactions at model membrane surfaces." Advances in Colloid and Interface Science **100**: 563-584.

Brockman, H. (1999). "Lipid monolayers: why use half a membrane to characterize protein-membrane interactions?" Current Opinion in Structural Biology **9**(4): 438-443.

Brockman, H. L., C. M. Jones, et al. (1980). "Application of a microcomputer-controlled film balance system to collection and analysis of data from mixed monolayers." Journal of Colloid and Interface Science **78**(2): 502-512.

Burack, W. R. and R. L. Biltonen (1994). "Lipid Bilayer Heterogeneities and Modulation of Phospholipase a(2) Activity." Chemistry and Physics of Lipids **73**(1-2): 209-222.

Chalikian, T. V. (2001). "Structural Thermodynamics of Hydration." J. Phys. Chem. B **105**(50): 12566-12578.

Christ, T., F. Kulzer, et al. (2001). "Watching the photo-oxidation of a single aromatic hydrocarbon molecule." Angewandte Chemie-International Edition **40**(22): 4192-4195.

Chung, H. S. (1966). "On the Macedo---Litovitz Hybrid Equation for Liquid Viscosity." The Journal of Chemical Physics **44**(4): 1362-1364.

Cohen, M. H. and D. Turnbull (1959). "Molecular Transport in Liquids and Glasses." The Journal of Chemical Physics **31**(5): 1164-1169.

Cupillard, L., R. Mulherkar, et al. (1999). "Both Group IB and Group IIA Secreted Phospholipases A2 Are Natural Ligands of the Mouse 180-kDa M-type Receptor." J. Biol. Chem. **274**(11): 7043-7051.

Dahmen-Levison, U., G. Brezesinski, et al. (1998). "Specific adsorption of PLA(2) at monolayers." Thin Solid Films **329**: 616-620.

Danielli, J. F. and H. Davson (1935). "A contribution to the theory of permeability of thin films." Journal of Cellular and Comparative Physiology **5**(4): 495-508.

Deschenes, L. A. and D. A. V. Bout (2002). "Single molecule photobleaching: increasing photon yield and survival time through suppression of two-step photolysis." Chemical Physics Letters **365**(5-6): 387-395.

Devaux, P. and H. M. McConnell (1972). "Lateral Diffusion in Spin-Labeled Phosphatidylcholine Multilayers." Journal of the American Chemical Society **94**(13): 4475-&.

Dickson, R. M., D. J. Norris, et al. (1996). "Three-dimensional imaging of single molecules solvated in pores of poly(acrylamide) gels." Science **274**(5289): 966-969.

Doolittle, A. K. (1951). "Studies in Newtonian Flow .2. the Dependence of the Viscosity of Liquids on Free-Space." Journal of Applied Physics **22**(12): 1471-1475.

Doolittle, A. K. (1952). "Studies in Newtonian Flow .3. the Dependence of the Viscosity of Liquids on Molecular Weight and Free Space (in Homologous Series)." Journal of Applied Physics **23**(2): 236-239.

Douglas Magde, E. L. E. W. W. W. (1974). "Fluorescence correlation spectroscopy. II. An experimental realization." Biopolymers **13**(1): 29-61.

Ebel, H., P. Grabitz, et al. (2001). "Enthalpy and volume changes in lipid membranes. I. The proportionality of heat and volume changes in the lipid melting transition and its implication for the elastic constants." Journal of Physical Chemistry B **105**(30): 7353-7360.

Edidin, M. (2003). "The state of lipid rafts: From model membranes to cells." Annual Review of Biophysics and Biomolecular Structure **32**: 257-283.

Egner, A., M. Schrader, et al. (1998). "Refractive index mismatch induced intensity and phase variations in fluorescence confocal, multiphoton and 4Pi-microscopy." Optics Communications **153**(4-6): 211-217.

Ehrenberg, M. and R. Rigler (1974). "Rotational brownian motion and fluorescence intensify fluctuations." Chemical Physics **4**(3): 390-401.

Einstein, A. (1905). "The motion of elements suspended in static liquids as claimed in the molecular kinetic theory of heat." Annalen Der Physik **17**(8): 549-560.

Elson, E. L. and D. Magde (1974). "Fluorescence Correlation Spectroscopy .1. Conceptual Basis and Theory." Biopolymers **13**(1): 1-27.

Engelman, D. M. (2005). "Membranes are more mosaic than fluid." Nature **438**(7068): 578-580.

Falck, E., M. Patra, et al. (2005). "Response to comment by Almeida et al.: Free area theories for lipid bilayers-predictive or not?" Biophysical Journal **89**(1): 745-752.

Feng, S. S. (1999). "Interpretation of Mechanochemical Properties of Lipid Bilayer Vesicles from the Equation of State or Pressure - Area Measurement of the Monolayer at the Air - Water or Oil - Water Interface." Langmuir **15**(4): 998-1010.

Fick, A. (1855). "Ueber Diffusion." Annalen der Physik und Chemie **170**(1): 59-86.

Funatsu, T., Y. Harada, et al. (1995). "Imaging of single fluorescent molecules and individual ATP turnovers by single myosin molecules in aqueous solution." Nature **374**(6522): 555-559.

Gaines, G. L. (1966). Insoluble monolayers at liquid-gas interfaces. New York, John Wiley & Sons Inc.

Galla, H. J., W. Hartmann, et al. (1979). "Two-Dimensional Passive Random-Walk in Lipid Bilayers and Fluid Pathways in Biomembranes." Journal of Membrane Biology **48**(3): 215-236.

Galla, H. J. and E. Sackmann (1974). "Lateral Diffusion in Hydrophobic Region of Membranes - Use of Pyrene Excimers as Optical Probes." Biochimica Et Biophysica Acta **339**(1): 103-115.

Gambin, Y., R. Lopez-Esparza, et al. (2006). "Lateral mobility of proteins in liquid membranes revisited." Proceedings of the National Academy of Sciences **103**(7): 2098-2102.

Georgallas, A. and D. A. Pink (1982). "Phase transitions in monolayers of saturated lipids : Exact results and Monte Carlo simulations." Journal of Colloid and Interface Science **89**(1): 107-116.

Ghosh, R. N. and W. W. Webb (1994). "Automated Detection and Tracking of Individual and Clustered Cell-Surface Low-Density-Lipoprotein Receptor Molecules." Biophysical Journal **66**(5): 1301-1318.

Goerke, J. (1998). "Pulmonary surfactant: functions and molecular composition." Biochimica et Biophysica Acta (BBA) - Molecular Basis of Disease **1408**(2-3): 79-89.

Gorter, E. M. D. and F. Grendel (1925). "On bimolecular layers of lipoids on the chromocytes of the blood." The Journal of Experimental

Medicine **41**: 439-443.

Grainger, D. W., A. Reichert, et al. (1989). "An Enzyme Caught in Action - Direct Imaging of Hydrolytic Function and Domain Formation of Phospholipase-a-2 in Phosphatidylcholine Monolayers." Febs Letters **252**(1-2): 73-82.

Grainger, D. W., A. Reichert, et al. (1990). "Hydrolytic Action of Phospholipase-A2 in Monolayers in the Phase-Transition Region - Direct Observation of Enzyme Domain Formation Using Fluorescence Microscopy." Biochimica Et Biophysica Acta **1023**(3): 365-379.

Grandbois, M., H. Clausen-Schaumann, et al. (1998). "Atomic force microscope imaging of phospholipid bilayer degradation by phospholipase A(2)." Biophysical Journal **74**(5): 2398-2404.

Gruen, D. W. R. and J. Wolfe (1982). "Lateral Tensions and Pressures in Membranes and Lipid Monolayers." Biochimica Et Biophysica Acta **688**(2): 572-580.

Hac, A. (2003). Diffusion process in membranes containing coexisting domains investigated by fluorescence correlation spectroscopy. Göttingen / Copenhagen, Max Planck Institute (Göttingen) / Niels Bohr Institute (University of Copenhagen). **Ph.D.**

Hac, A. E., H. M. Seeger, et al. (2005). "Diffusion in two-component lipid membranes - A fluorescence correlation spectroscopy and Monte Carlo simulation study." Biophysical Journal **88**(1): 317-333.

Hardy, N. J., T. H. Richardson, et al. (2006). "Minimising monolayer collapse on Langmuir troughs." Colloids and Surfaces a-Physicochemical and Engineering Aspects **284**: 202-206.

Hecht, E. (2002). Optics, Addison Wesley.

Heimburg, T. (1998). "Mechanical aspects of membrane thermodynamics. Estimation of the mechanical properties of lipid membranes close to the chain melting transition from calorimetry." Biochimica Et Biophysica Acta-Biomembranes **1415**(1): 147-162.

Heimburg, T. (2007). Thermal Biophysics of Membranes, Wiley-VCH.

Heimburg, T. and A. D. Jackson (2005). "On soliton propagation in biomembranes and nerves." Proceedings of the National Academy of Sciences of the United States of America **102**(28): 9790-9795.

Hess, S. T. and W. W. Webb (2002). "Focal volume optics and experimental artifacts in confocal fluorescence correlation spectroscopy." Biophysical Journal **83**(4): 2300-2317.

Hewson, W. (1773). "On the figure and composition of the red particles of the blood, commonly called the red globules." Philosophical Transactions **63**: 306-24.

Honger, T., K. Jorgensen, et al. (1996). "Systematic Relationship between Phospholipase A2 Activity and Dynamic Lipid Bilayer Microheterogeneity." Biochemistry **35**(28): 9003-9006.

Hoogenboom, J. P., J. Hernando, et al. (2007). "Power-law blinking in the fluorescence of single organic molecules." ChemPhysChem **8**(6): 823-833.

Hoogenboom, J. P., E. M. H. P. van Dijk, et al. (2005). "Power-Law-Distributed Dark States are the Main Pathway for Photobleaching of Single Organic Molecules." Physical Review Letters **95**(9): 097401-4.

Hoyrup, P., T. H. Callisen, et al. (2004). "Lipid protrusions, membrane softness, and enzymatic activity." Physical Chemistry Chemical Physics **6**(7): 1608-1615.

Hughes, B. D., B. A. Pailthorpe, et al. (1981). "The Translational and Rotational Drag on a Cylinder Moving in a Membrane." Journal of Fluid Mechanics **110**(SEP): 349-372.

Hughes, B. D., B. A. Pailthorpe, et al. (1982). "Extraction of Membrane Microviscosity from Translational and Rotational Diffusion Coefficients." Biophys. J. **37**(3): 673-676.

Humpolickova, J., E. Gielen, et al. (2006). "Probing Diffusion Laws within Cellular Membranes by Z-Scan Fluorescence Correlation Spectroscopy." Biophys. J. **91**(3): L23-25.

Israelachvili, J. N. (1991). Intermolecular and Surface Forces, Second Edition: With Applications to Colloidal and Biological Systems, Academic Press.

Ivanova, M. G., T. Ivanova, et al. (1996). "Hydrolysis of monomolecular films of long chain phosphatidylcholine by phospholipase A2 in the presence of [beta]-cyclodextrin." Colloids and Surfaces B: Biointerfaces **6**(1): 9-17.

Ivanova, M. G., T. Ivanova, et al. (1996). "Hydrolysis of monomolecular films of long chain phosphatidylcholine by phospholipase A(2) in the presence of beta-cyclodextrin." Colloids and Surfaces B-Biointerfaces **6**(1): 9-17.

Jacobson, K., E. D. Sheets, et al. (1995). "Revisiting the Fluid Mosaic Model of Membranes." Science **268**(5216): 1441-1442.

Jahnig, F. (1984). "Lipid Exchange between Membranes." Biophysical Journal **46**(6): 687-694.

Jain, M. K. and O. G. Berg (1989). "The Kinetics of Interfacial Catalysis by Phospholipase-A2 and Regulation of Interfacial Activation - Hopping Versus Scooting." Biochimica Et Biophysica Acta **1002**(2): 127-156.

Jensen, U. B. and A. C. Simonsen (2005). "Shape relaxations in a fluid supported membrane during hydrolysis by phospholipase A2." Biochimica et Biophysica Acta (BBA) - Biomembranes **1715**(1): 1-5.

Jianqiang Qu, C. K. M. P. K. M. (2004). "Ionic Perylenetetracarboxdiimides: Highly Fluorescent and Water-Soluble Dyes for Biolabeling." Angewandte Chemie **116**(12): 1554-1557.

Kaganer, V. M., H. Mohwald, et al. (1999). "Structure and phase transitions in Langmuir monolayers." Reviews of Modern Physics **71**(3): 779-819.

Kane, S. A., M. Compton, et al. (2000). "Interactions determining the growth of chiral domains in phospholipid monolayers: Experimental results and comparison with theory." Langmuir **16**(22): 8447-8455.

Kask, P., R. Gunther, et al. (1997). "Statistical accuracy in fluorescence fluctuation experiments." European Biophysics Journal with Biophysics Letters **25**(3): 163-169.

Kastrup, L., H. Blom, et al. (2005). "Fluorescence fluctuation spectroscopy in subdiffraction focal volumes." Physical Review Letters **94**(17).

Ke, P. C. and C. A. Naumann (2001). "Single molecule fluorescence imaging of phospholipid monolayers at the air-water interface." Langmuir **17**(12): 3727-3733.

Kim, S. H. and H. Yu (1992). "Lateral Diffusion of Amphiphiles and Macromolecules at the Air-Water-Interface." Journal of Physical Chemistry **96**(10): 4034-4040.

Klopfer, K. J. and T. K. Vanderlick (1996). "Isotherms of dipalmitoylphosphatidylcholine (DPPC) monolayers: Features revealed and features obscured." Journal of Colloid and Interface Science **182**(1): 220-229.

Korlach, J., P. Schwille, et al. (1999). "Characterization of lipid bilayer phases by confocal microscopy and fluorescence correlation spectroscopy." Proceedings of the National Academy of Sciences **96**(15): 8461-8466.

Kruger, P. and M. Losche (2000). "Molecular chirality and domain shapes in lipid monolayers on aqueous surfaces." Physical Review E **62**(5): 7031-7043.

Kudo, I. and M. Murakami (2002). "Phospholipase A2 enzymes." Prostaglandins & Other Lipid Mediators **68-69**: 3-58.

Kusumi, A., I. Koyama-Honda, et al. (2004). "Molecular Dynamics and Interactions for Creation of Stimulation-Induced Stabilized Rafts from Small Unstable Steady-State Rafts." Traffic **5**(4): 213-230.

Lakowicz, J. R. (2004). Principles of Fluorescence Spectroscopy, Springer Science-Buisiness Media Inc.

Lang, E., J. Baier, et al. (2006). "Epifluorescence, confocal and total internal reflection microscopy for single-molecule experiments: a quantitative comparison." Journal of Microscopy-Oxford **222**: 118-123.

Langmuir, I. (1917). "The constitution and fundamental properties of solids and liquids. II. Liquids." Journal of the American Chemical Society **39**(9): 1848-1906.

Lee, A. G. (1977). "Lipid Phase-Transitions and Phase-Diagrams .1. Lipid Phase-Transitions." Biochimica Et Biophysica Acta **472**(2): 237-281.

Li, J. B., Z. J. Chen, et al. (2000). "Dynamic observations of the hydrolysis of a DPPC monolayer at the air/water interface catalyzed by phospholipase A(2)." Angewandte Chemie-International Edition **39**(17): 3059-3062.

Li, J. B., R. Miller, et al. (1998). "Spreading concentration effect on the morphology of phospholipid monolayers." Thin Solid Films **329**: 84-86.

Lichtman, J. W. and J.-A. Conchello (2005). "Fluorescence microscopy." Nat Meth **2**(12): 910-919.

Liu, C. H., A. Paprica, et al. (1997). "Effects of size of macrocyclic polyamides on their rate of diffusion in model membranes." Biophysical Journal **73**(5): 2580-2587.

Lösche, H. and H. Mohwald (1984). "Fluorescence microscopy on monomolecular films at an air/water interface." Colloids and Surfaces **10**: 217-224.

Lösche, M. and H. Mohwald (1984). "Fluorescence microscope to observe dynamical processes in monomolecular layers at the air/water interface." Review of Scientific Instruments **55**(12): 1968-1972.

Lösche, M. and H. Möhwald (1984). "Impurity controlled phase transitions of phospholipid monolayers." European Biophysics Journal **11**(1): 35-42.

Lösche, M., E. Sackmann, et al. (1983). "A Fluorescence Microscopic Study Concerning the Phase-Diagram of Phospholipids." Berichte Der Bunsen-Gesellschaft-Physical Chemistry Chemical Physics **87**(10): 848-852.

Macdonald, A. G. (1988). "Application of the Theory of Homeoviscous Adaptation to Excitable-Membranes - Pre-Synaptic Processes." Biochemical Journal **256**(2): 313-327.

Macedo, P. B. and T. A. Litovitz (1965). "On Relative Roles of Free Volume and Activation Energy in Viscosity of Liquids." Journal of Chemical Physics **42**(1): 245-256.

Magde, D., E. L. Elson, et al. (1974). "Fluorescence correlation spectroscopy. II. An experimental realization." Biopolymers **13**(1): 29-61.

Maloney, K. M. and D. W. Grainger (1993). "Phase-Separated Anionic Domains in Ternary Mixed Lipid Monolayers at the Air-Water-Interface." Chemistry and Physics of Lipids **65**(1): 31-42.

Mandelbrot, B. (1967). "How Long Is the Coast of Britain? Statistical Self-Similarity and Fractional Dimension." Science **156**(3775): 636-638.

Margineanu, A., J. Hofkens, et al. (2004). "Photophysics of a water-soluble rylene dye: Comparison with other fluorescent molecules for biological applications." Journal of Physical Chemistry B **108**(32): 12242-12251.

Marsh, D. (1996). "Lateral pressure in membranes." Biochimica et Biophysica Acta (BBA) - Reviews on Biomembranes **1286**(3): 183-223.

Marsh, D. (2006). "Comment on interpretation of mechanochemical properties of lipid bilayer vesicles from the equation of state or pressure-area measurement of the monolayer at the air-water or oil-water interface." Langmuir **22**(6): 2916-2919.

Masuda, A., K. Ushida, et al. (2005). "New Fluorescence Correlation Spectroscopy Enabling Direct Observation of Spatiotemporal Dependence of Diffusion Constants as an Evidence of Anomalous Transport in Extracellular Matrices." Biophys. J. **88**(5): 3584-3591.

Masuda, A., K. Ushida, et al. (2005). "New fluorescence correlation spectroscopy enabling direct observation of spatiotemporal dependence of diffusion constants as an evidence of anomalous transport in extracellular matrices." Biophysical Journal **88**(5): 3584-3591.

McConlogue, C. W. and T. K. Vanderlick (1997). "A close look at domain formation in DPPC monolayers." Langmuir **13**(26): 7158-7164.

McConnell, H. M., L. K. Tamm, et al. (1984). "Periodic Structures in Lipid Monolayer Phase Transitions." Proceedings of the National Academy of Sciences **81**(10): 3249-3253.

Moerner, W. E. and M. Orrit (1999). "Illuminating single molecules in condensed matter." Science **283**(5408): 1670-+.

Mouritsen, O. G., T. L. Andersen, et al. (2006). "Activation of interfacial enzymes at membrane surfaces." Journal of Physics-Condensed Matter **18**(28): S1293-S1304.

Mouritsen, O. G. and M. Bloom (1984). "Mattress Model of Lipid-Protein Interactions in Membranes." Biophysical Journal **46**(2): 141-153.

Möhwald, H., Ed. (1995). Phospholipid Monolayers. Handbook of Biological Physics, Elsevier, Amsterdam.

Nagle, J. F. (1976). "Theory of Lipid Monolayer and Bilayer Phase-Transitions - Effect of Headgroup Interactions." Journal of Membrane Biology **27**(3): 233-250.

Nagle, J. F. (1993). "Area Lipid of Bilayers from Nmr." Biophysical Journal **64**(5): 1476-1481.

Nagle, J. F. and S. Tristram-Nagle (2000). "Structure of lipid bilayers." Biochimica et Biophysica Acta (BBA) - Reviews on Biomembranes **1469**(3): 159-195.

Nielsen, L. K., T. Bjornholm, et al. (2000). "Critical phenomena: Fluctuations caught in the act." Nature **404**(6776): 352-352.

Nielsen, L. K., T. Bjornholm, et al. (2007). "Thermodynamic and Real-Space Structural Evidence of a 2D Critical Point in Phospholipid Monolayers." Langmuir **23**(23): 11684-11692.

Nielsen, L. K., J. Risbo, et al. (1999). "Lag-burst kinetics in phospholipase A2 hydrolysis of DPPC bilayers visualized by atomic force microscopy." Biochimica et Biophysica Acta (BBA) - Biomembranes **1420**(1-2): 266-271.

Ober, R. J., S. Ram, et al. (2004). "Localization Accuracy in Single-Molecule Microscopy." Biophys. J. **86**(2): 1185-1200.

Op den Kamp, J., J. de Gier, et al. (1974). "Hydrolysis of Phosphatidylcholine Liposomes by Pancreatic Phospholipase A2 at Transition-Temperature." Biochimica Et Biophysica Acta **345**(2): 253-256.

Overton, E. (1899). "On the general osmotic properties of the cell, their probable origin, and their significance for physiology." Vierteljahrschrift der Naturforschende Gesselschaft (Zurich) **44**: 88-135.

Paige, M. F., E. J. Bjerneld, et al. (2001). "A comparison of through-the-objective total internal reflection microscopy and epifluorescence microscopy for single-molecule fluorescence Imaging." Single Molecules **2**(3): 191-201.

Pallas, N. R. and B. A. Pethica (1985). "Liquid-Expanded to Liquid-Condensed Transitions in Lipid Monolayers at the Air Water Interface." Langmuir **1**(4): 509-513.

Peters, R. and K. Beck (1983). "Translational Diffusion in Phospholipid Monolayers Measured by Fluorescence Microphotolysis." Proceedings of the National Academy of Sciences **80**(23): 7183-7187.

Petty, M. C. (1996). Langmuir-Blodgett Films: An Introduction, Cambridge University Press

Piston, D. W. (1998). "Choosing Objective Lenses: The Importance of Numerical Aperture and Magnification in Digital Optical Microscopy." Biol Bull **195**(1): 1-4.

Qian, A. H., M. P. Sheetz, et al. (1991). "Single-Particle Tracking - Analysis of Diffusion and Flow in 2-Dimensional Systems." Biophysical Journal **60**(4): 910-921.

Rayleigh (1879). "Investigations in optics with special reference to the spectroscope. 1. Resolving, or separating power of optical instruments." Philosophical Magazine **8**: 261-274.

Razinaqv, K., J. P. Behr, et al. (1974). "Methods for Probing Lateral Diffusion of Membrane Components - Triplet-Triplet Annihilation and Triplet-Triplet Energy-Transfer." Chemical Physics Letters **26**(3): 440-444.

Ricci, F. P., M. A. Ricci, et al. (1977). "Free Volume Theory and on Macedo-Litovitz Hybrid Equation for Diffusion in Liquids." Journal of Physical Chemistry **81**(2): 171-177.

Rigler, R., Ü. Mets, et al. (1993). "Fluorescence correlation spectroscopy with high count rate and low background: analysis of translational diffusion." European Biophysics Journal **22**(3): 169-175.

Rocha, S., J. A. Hutchison, et al. (2008). "Linking phospholipase mobility to activity by single molecule wide-field microscopy." Submitted.

Romero, G., K. Thompson, et al. (1987). "The Activation of Porcine Pancreatic Phospholipase-A2 by Dipalmitoylphosphatidylcholine Large Unilamellar Vesicles - Analysis of the State of Aggregation of the Activated Enzyme." Journal of Biological Chemistry **262**(28): 13476-13482.

Sackmann, E. and H. Trauble (1972). "Studies of Crystalline-Liquid Crystalline Phase-Transition of Lipid Model Membranes .1. Use of Spin Labels and Optical Probes as Indicators of Phase-Transition." Journal of the American Chemical Society **94**(13): 4482-&.

Saffman, P. G. and M. Delbruck (1975). "Brownian Motion in Biological Membranes." Proceedings of the National Academy of Sciences **72**(8): 3111-3113.

Saxton, M. J. (1987). "Lateral Diffusion in an Archipelago - the Distance Dependence of the Diffusion Constant." Biophysical Journal **51**(2): A542-A542.

Saxton, M. J. (1994). "Anomalous Diffusion Due to Obstacles - a Monte-Carlo Study." Biophysical Journal **66**(2): 394-401.

Saxton, M. J. (1997). "Single-particle tracking: The distribution of diffusion coefficients." Biophysical Journal **72**(4): 1744-1753.

Saxton, M. J. (1999). "Lateral diffusion of lipids and proteins." Membrane Permeability **48**: 229-282.

Saxton, M. J. (2005). "Fluorescence Correlation Spectroscopy." Biophys. J. **89**(6): 3678-3679.

Saxton, M. J. (2007). "A Biological Interpretation of Transient Anomalous Subdiffusion. I. Qualitative Model." Biophys. J. **92**(4): 1178-1191.

Saxton, M. J. and K. Jacobson (1997). "Single-particle tracking: Applications to membrane dynamics." Annual Review of Biophysics and Biomolecular Structure **26**: 373-399.

Schmidt, T., G. J. Schutz, et al. (1996). "Imaging of single molecule diffusion." Proceedings of the National Academy of Sciences **93**(7): 2926-2929.

Schmidt, T., G. J. Schutz, et al. (1996). "Imaging of single molecule diffusion." Proceedings of the National Academy of Sciences of the United States of America **93**(7): 2926-2929.

Schutz, G. J., H. Schindler, et al. (1997). "Single-molecule microscopy on model membranes reveals anomalous diffusion." Biophys. J. **73**(2): 1073-1080.

Schutz, G. J., H. Schindler, et al. (1997). "Single-molecule microscopy on model membranes reveals anomalous diffusion." Biophysical Journal **73**(2): 1073-1080.

Schwille, P. and A. Garcia-Sáez (2007). "Single molecule techniques for the study of membrane proteins." Applied Microbiology Biotechnol **76**(10): 257-266(

Seelig, J. and A. Seelig (1980). "Lipid Conformation in Model Membranes and Biological-Membranes." Quarterly Reviews of Biophysics **13**(1): 19-61.

Sharonov, A. and R. M. Hochstrasser (2006). "Wide-field subdiffraction imaging by accumulated binding of diffusing probes." Proceedings of the National Academy of Sciences of the United States of America **103**(50): 18911-18916.

Simonsen, A. C. (2008). "Activation of Phospholipase A2 by Ternary Model Membranes." Biophys. J. **94**(10): 3966-3975.

Simonsen, A. C., U. B. Jensen, et al. (2006). "Hydrolysis of fluid supported membrane islands by phospholipase A(2): Time-lapse imaging and kinetic analysis." Journal of Colloid and Interface Science **301**(1): 107-115.

Singer, S. J. and G. L. Nicolson (1972). "The Fluid Mosaic Model of the Structure of Cell Membranes." Science **175**(4023): 720-731.

Six, D. A. and E. A. Dennis (2000). "The expanding superfamily of phospholipase A(2) enzymes: classification and characterization." Biochimica Et Biophysica Acta-Molecular and Cell Biology of Lipids **1488**(1-2): 1-19.

Sprague, B. L. and J. G. McNally (2005). "FRAP analysis of binding: proper and fitting." Trends in Cell Biology **15**(2): 84-91.

Spring, S. I. a. K. R. (1997). Video Microscopy: The Fundamentals. New York, Plenum Press.

Suppan, P. (1994). Chemistry and light. Cambridge, The Royal Society of Chemistry.

Tanaka, K., P. A. Manning, et al. (1999). "Lipid lateral diffusion in dilauroylphosphatidylcholine/cholesterol mixed monolayers at the air/water interface." Langmuir **15**(2): 600-606.

Tang, J. and R. A. Marcus (2005). "Diffusion-Controlled Electron Transfer Processes and Power-Law Statistics of Fluorescence Intermittency of Nanoparticles." Physical Review Letters **95**(10): 107401-4.

Tang, T., K. Peneva, et al. (2007). "Photophysics of Water Soluble Perylene Diimides in Surfactant Solutions." J. Phys. Chem. A **111**(42): 10609-10614.

Van Deenen, L. L. M. and G. H. De Haas (1963). "The substrate specificity of phospholipase A." Biochimica et Biophysica Acta (BBA) - Specialized Section on Lipids and Related Subjects **70**: 538-553.

Vaz, W. L. C., R. M. Clegg, et al. (1985). "Translational Diffusion of Lipids in Liquid-Crystalline Phase Phosphatidylcholine Multibilayers - a Comparison of Experiment with Theory." Biochemistry **24**(3): 781-786.

Verger, R. and G. H. De Haas (1976). "Interfacial Enzyme Kinetics of Lipolysis." Annual Review of Biophysics and Bioengineering **5**(1): 77-117.

von Tscharner, V. and H. M. McConnell (1981). "An alternative view of phospholipid phase behavior at the air-water interface. Microscope and film balance studies." Biophys. J. **36**(2): 409-419.

Wawrezinieck, L., H. Rigneault, et al. (2005). "Fluorescence Correlation Spectroscopy Diffusion Laws to Probe the Submicron Cell Membrane Organization." Biophys. J. **89**(6): 4029-4042.

Webb, W. W. (1974). "Fluorescence Correlation Spectroscopy." Bulletin of the American Physical Society **19**(3): 197-197.

Widengren, J., U. Mets, et al. (1995). "Fluorescence Correlation Spectroscopy of Triplet-States in Solution - a Theoretical and Experimental-Study." Journal of Physical Chemistry **99**(36): 13368-13379.

Widengren, J. and Ü. Mets (2003). Conceptual Basis of Fluorescence Correlation Spectroscopy and Related Techniques as Tools in Bioscience. Single Molecule Detection in Solution. C. Zander, J. Enderlein and R. Keller, Wiley-VCH 69-120.

Wu, E., K. Jacobson, et al. (1977). "Lateral diffusion in phospholipid multibilayers measured by fluorescence recovery after photobleaching." Biochemistry **16**(17): 3936-3941.

Xiang, T. x. (1999). "Translational Diffusion in Lipid Bilayers: Dynamic Free-Volume Theory and Molecular Dynamics Simulation." J. Phys. Chem. B **103**(2): 385-394.

Yeow, E. K. L., S. M. Melnikov, et al. (2006). "Characterizing the Fluorescence Intermittency and Photobleaching Kinetics of Dye Molecules Immobilized on a Glass Surface." J. Phys. Chem. A **110**(5): 1726-1734.

Yu, J., D. H. Hu, et al. (2000). "Unmasking electronic energy transfer of conjugated polymers by suppression of O-2 quenching." Science **289**(5483): 1327-1330.

Yura, H. T. and T. S. Rose (1995). "Gaussian beam transfer through hard-aperture optics." Applied Optics **34**(30): 6826 - 6828.

Zhai, X. H., J. B. Li, et al. (2003). "Direct observations of the cleavage-reaction of an L-DPPC monolayer catalyzed by phospholipase A(2) and inhibited by an indole inhibitor at the air/water interface." Chembiochem **4**(4): 299-305.

Zhou, F. and K. Schulten (1996). "Molecular dynamics study of phospholipase A(2) on a membrane surface." Proteins-Structure Function and Genetics **25**(1): 12-27.

Zondervan, R., F. Kulzer, et al. (2004). "Photobleaching of Rhodamine 6G in Poly(vinyl alcohol) at the Ensemble and Single-Molecule Levels." J. Phys. Chem. A **108**(10): 1657-1665.

Zondervan, R., F. Kulzer, et al. (2003). "Photoblinking of rhodamine 6G in poly(vinyl alcohol): Radical dark state formed through the triplet." Journal of Physical Chemistry A **107**(35): 6770-6776.